博士学位論文

# 水中環境における光学画像の画質改善に関する研究

平成２７年度

李　玉潔

九州工業大学大学院　工学府 電気電子工学専攻

Ph.D. Thesis

# Study on Optical Image Quality Improvement for Underwater Environment

by
Yujie Li

B.S., Yangzhou University (2009)
M.E., Yangzhou University (2012)
M.E., Kyushu Institute of Technology (2012)
Submitted in partial fulfillment of the requirements for
the degree of Ph.D. of Engineering
at the

KYUSHU INSTITUTE OF TECHNOLOGY

September, 2015

# TABLE OF CONTENTS

# List of Tables

# List of Figures

# List of Acronyms

| | |
|---|---|
| **GOOS** | Global Ocean Observing System |
| **GCOS** | Global Climate Observing System |
| **GEOSS** | Global Earth Observing System of Systems |
| **DBLP** | Data Buoy Cooperation Panel |
| **WMO** | World Meteorological Organization |
| **UUV** | Unmanned Underwater Vehicles |
| **AUV** | Autonomous Underwater Vehicles |
| **SSS** | Sector Scanning Sonars |
| **ROV** | Remotely Operated Vehicles |
| **TOBI** | Towed Ocean Bottom Instrument |
| **MBS** | Multi Beam Sonar |
| **FCM** | Fuzzy C Means |
| **CNR** | Contrast-to-Noise Ratio |
| **HVS** | Human Visual System |
| **SSIM** | Structural Similarity |
| **PSNR** | Peak Signal to Noise Ratio |
| **CCT** | Corrected Color Temperature |
| **MSE** | Mean Squared Error |
| **SPD** | Spectral Power Distribution |
| **ACWFCM** | Automatic Clustering Weighted Fuzzy C Means |
| **ACE** | Automatic Color Equalization |
| **BF** | Bilateral Filter |
| **LBF** | Local Binary Fitting |
| **AOS** | Additive Operator Splitting |
| **SDF** | Signed Distance Function |
| **GAC** | Geodesic Active Contours |

| | |
|---|---|
| **GAR** | Geodesic Active Regions |
| **PC** | Piecewise Constant |
| **PS** | Piecewise Smooth |
| **ACM** | Active Contour Model |
| **DMS** | Deep-sea Mining Systems |
| **CIE** | Commission Internationale de L'Eclairage |
| **FACM** | Fast Active Contour Model |

# Abstract

Since the 1960s, autonomous underwater vehicles (AUVs) and unmanned underwater vehicles (UUVs) have been used for deep-sea exploration. Sonar sensors also have been extensively used to detect and recognize objects in oceans. Although sonar sensors are suitable for long-range distance imaging, due to the principles of acoustic imaging, sonar images are low signal to noise ratio, low resolution and no colors. In order to acquire more detail information of underwater object, a short-range imaging system is required. In this situation, a photo vision sensor is used reasonably. However, the low contrast and color distortion of underwater images are still the major issues for practical applications. Therefore, this thesis will concentrate on the underwater optical images quality improvement.

Although the underwater optical imaging technology has made a great progress, the recognition of underwater objects is still a challenging subject nowadays. Different from the normal images, underwater images suffer from poor visibility due to the medium scattering and light distortion. First of all, capturing good quality images in underwater circumstance is difficult, mostly due to attenuation caused by light that is reflected from a surface and is deflected and scattered by particles. Secondly, absorption substantially reduces the light energy. The random attenuation of the light mainly causes the haze appearance along with the part of the light scattered back from the water. In particular, an underwater object which 10 meters away from camera lens is almost indistinguishable because of light absorption. Furthermore, when the artificial light is employed, it can cause a distinctive footprint on the seafloor.

In order to obtain high quality underwater images that can be adapted to the traditional image identification algorithms, this work aimed to construct an underwater image processing framework. Due to the special characteristic of underwater images,

segment the image to several parts before directly perform a subject identification is thought an efficient way. And for obtaining a good underwater image segment result, the work to improve the quality of the image is necessary. Such work contains image enhancement, color correction and noise reduction, etc. The experiments demonstrate that the proposed methods produced visually pleasing results, and the numerical image quality assessment also proved the effectiveness of this proposal. The organization of this thesis is as follows.

Chapter 1 briefly reviews the characteristics and types of acoustic imaging and optical imaging technologies in ocean. The traditional underwater imaging models and the issues of recent underwater imaging systems are also introduced.

Chapter 2 describes a novel underwater image enhancement method. The transmission is estimated by the proposed dual-channel prior. Then a robust locally adaptive filter algorithm for enhancing underwater images is used. In addition, the artificial light removal method is also proposed. Compared with the traditional methods, the proposed method obtains better images.

Chapter 3 presents a color correction method to recover the distorted image colors. In the experiments, the proposed method recovers the distorted colors in real-time. The color corrected images have a reasonable noise level in their dark regions, and the global contrast is also well improved.

Chapter 4 describes two methods for image segmentation. The first one is the automatic clustering Weighted Fuzzy C Means (WFCM) based segmentation method. It automatically obtains a reasonable clustering result for the underwater images with simple texture. The second method is fast Active Contour Model (ACM) based image segmentation method, which dramatically improves the calculation speed. Compare with the traditional methods, the processing speed is improved by over 10 times.

Chapter 5 presents the conclusions of this work, and points out some future research directions.

# Chapter 1

# Introduction

## 1.1 Ocean Observation

Ocean is human valuable asset. With the continued growth of the population, land resources are large consumption. Each country has increased marine development. Ocean observations [1] have being developed and deployed by scientists and researchers for monitoring the status of ocean. Some observatories are cabled, such as, the Ocean Networks Canada Observatory [2] which contains VENUS and NEPTUNE Canada cabled networks. It used for real-time interactive experiments, for example, measuring ocean health, resources, natural hazards, marine conservation and ecosystems. Some observatories are made up of surface buoys, such as NOAA Ocean Climate Observation System [3]. The observations near the equator are of particular important to climate. Besides of monitoring the air-water exchange of heat and water, the moored buoys provide platforms for instrumentation to measure the air-water exchange of carbon dioxide in the tropics. Some observatories are remote sensed, such as Japanese Ocean Flux Data Sets with Use of Remote Sensing Observation [4]. It is used for monitoring the changes of heat, water and momentum with atmosphere at ocean surface.

Interestingly, there are some excellent systems for ocean observing, such as Global Ocean Observing System proposed by Henry. Stommel WHOI [5]. More than 30 countries are joined in this program. However, until now this system also has some drawbacks. First, the system is not fully built-out because of funding issues. Second, most of subsystems are not at full operational capacity. Many of them are funded through research programs rather than operational. Third, deep ocean (under 2000 meters) is very under-sampled-issue of technology and cost.

In this thesis, we firstly review the ocean observation systems in technology level. Then, analysis the feasibility of recent systems and propose some novel technologies for improving recent optical imaging systems.

### 1.1.1 Remote Sensing

Costal and ocean resources are fully affected by ocean, land-atmospheric physics, biology and geology. Extreme events and environmental disasters require the satellite remote sensing to track currents, map ocean productivity, assess winds and waves. The development and usage of satellites that complement ship-based observations, moored and other autonomous sensors and models. It will provide high quality data more frequently, allowing for improving site-specific forecasts of weather, water conditions, and resource distribution [6].

Fortunately, there are existed some ocean remote sensing systems in the world. The Global Ocean Observing System (GOOS), the Global Climate Observing System (GCOS), and the Global Earth Observing System of Systems (GEOSS) are coordinated with U.S. plans for satellite remote sensing.

### 1.1.2 In Situ Sensing

In 1985, the Data Buoy Cooperation Panel (DBLP) was estimated, as a joint body of the World Meteorological Organization (WMO) and Intergovernmental Oceanographic Commission (IOC) of UNESCO. The DBLP aims to share international coordination and assist those providing and using observations from data buoys, within the meteorological and oceanographic communities [7].

Until now, DBLP has 1250 global surface drifting buoy array with 5 degrees resolution. It also has 120 moorings for combining the global tropical moored buoy network.

### 1.1.3 Underwater Sensing

Ocean bottom sensor nodes plan an important role for underwater sensing. They are used for monitoring the oceanographic data collection, pollution monitoring, offshore

exploration, disaster prevention, assisted navigation and tactical surveillance. Unmanned underwater vehicles (UUVs) and Autonomous underwater vehicles (AUVs) are equipped with underwater sensors. And most of them are used to find application in exploration of natural underwater resources and gathering of scientific data in collaborative monitoring missions.

Recently, wireless underwater acoustic networking is the enabling technology for these applications. Although underwater communication has been studied since the Second World War, there are also some disadvantages. Firstly, real time monitoring is impossible. Secondly, control of the underwater systems is difficult. Thirdly, it is limited to record the amount of data during the monitoring mission [8]. Many researchers are currently focusing on developing next generalization network for terrestrial wireless ad hoc and sensor networks.

## 1.2 Imaging Systems

### 1.2.1 Sonar Systems

Sound can be used to produce a map of reflected intensities, which is called sonogram. These sonar images are often similar to optical images, and the level of details higher than the traditional ways. People should take significant experience before interpret the information correctly [9].

Sonograms are made by the devices which emit beam pulses toward the bottom of the ocean. The sonar beams are narrow in one direction and wide in the other direction, emitted down from the transducer to the objects. The intensities of the acoustic reflection from the seafloor are called “fan-shaped”, which likes an image. As the beam is moved, the reflections will depict a series of image lines perpendicular to the direction of motion [9]. When stitched together “along track”, the beam-lines will produced a single image of the seabed or objects.

It is necessary that the movement can be gained by rotation of the transducer array, just like in sector scanning sonars (SSS) for remotely operated vehicle (ROV), where they are used as navigational aids, such as conventional ship-radars. However, the

equipment is towed on a cable behind the ship, and because of the lines imaged is perpendicular to the length axis of ship.

In the 1970s, the long range GLORIA side-scan sonar was developed. It was used to monitor the large oceanic areas, operated at low frequencies (6 kHz) and was used to produce images of continental shelves world-wide [10]. Recently, the 30 kHz Towed Ocean Bottom Instrument (TOBI) multi-sensor is used instead of it. To reach a higher resolution of the sonar image, it is possible to either increase the frequency or to increase the number of elements of the transducer array [11]. On the other hand, signal processing techniques are used for improving its performance.

About 40 years ago, there have been many researchers who attempt to design an acoustic-optical camera. The first successful set was the EWATS system, which was created in the 1970s and had 200 lines of resolution and maximum of 10 meters range. In the 2000s, DIDSON [12], Echoscope [13], BlueView [14] or the other acoustic camera are designed for serving the underwater.

While the above mentioned acoustic imaging systems perform well, they also have the challenges in the measurement of the seafloor or objects. In order to monitor and survey small-scale bed objects in the ocean, coastal, river, the issue of increase the accuracy and resolution of imaging sonars is also remaining. Another issue is to reduce the cost of multi-beam sonar (MBS), so as to facilitate a wider application of the technique.

### 1.2.2 Optical Systems

Optical imaging sensors can be provided much information at high speed. They are commonly used in many terrestrial and air robotic application. However, because of the interaction between electromagnetic waves and water, optical imaging systems and vision systems need to be specifically designed to be able to use in underwater environment [15].

Underwater images have specific characteristics that should be consider during the gathering process and processing process. Light attenuation, scattering, non-uniform

lighting, shadows, color distortion, suspended particles or abundance of marine life on top or surrounding the target are frequently found in typical underwater scenes.

## 1.3 Issues in Imaging Systems

One effect of the inherent optical properties (IOP) of ocean is that it becomes darker and darker with the water depth increases. As the water depth increases, the light from the sun is absorbed and scattered. For example, in the clean ocean water, the euphotic depth is less than 200 meters [16]. In addition, the spectral composition of sunlight also changes with the water depth. Absorption is larger for long wavelengths (red color) than for short (green color); therefore, most of underwater images taken by natural light (sunlight) will appear blue or green on images or videos. Consequently, for the application of deep-sea or turbidly water, additional illumination is required.

### 1.3.1 Scattering

The volume scattering function describes the angular distribution of light scattered by a suspension of particles toward the direction at a wavelength. In the past years, many researchers in optical oceanography built instruments to measure the volume scattering function of sea waters [17]. Figure 1-1 shows three of Petzold's VSF curves displayed on a log-log plot to emphasize the forward scattering angles. Then instruments are a spectral response centered at $\lambda = 514nm$ with a bandwidth of 75 *nm* [18].

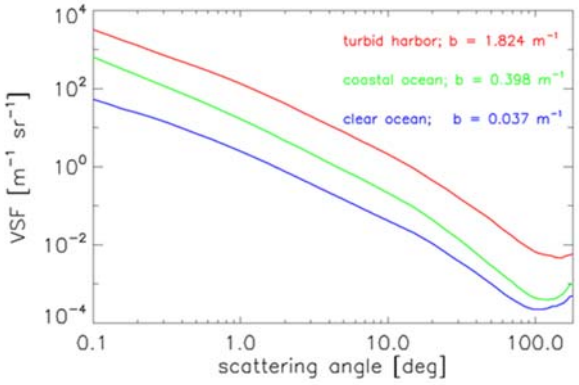


**Figure 1-1**: Log-log plots of Petzold's measured volume scattering function from three different waters

### 1.3.2 Absorption

When light penetrates the water, photons are either absorbed or scattered. While scattering redirects the angle of the photon path, absorption removes the photons from the light path. The absorption is highly spectrally dependent. In practice, it is hardly to measure the absorption rate [19].

Absorption by water is shown in Figure 1-2. The blue wavelength is more highly absorbed than red wavelength.

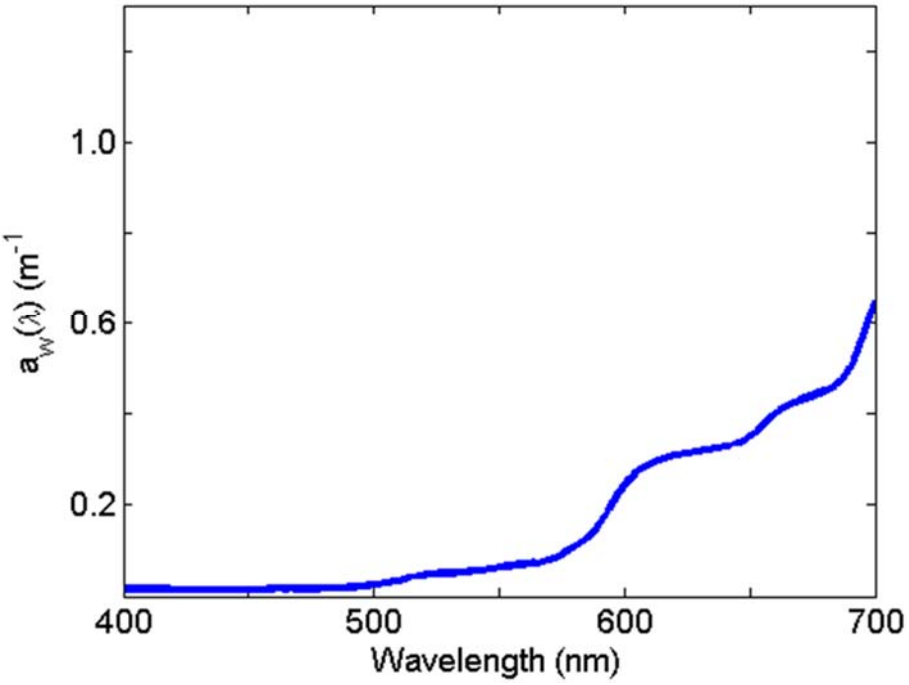


**Figure 1-2**: Absorption spectrum for pure water

The absorption rate of phytoplankton is shown in Figure 1-3.

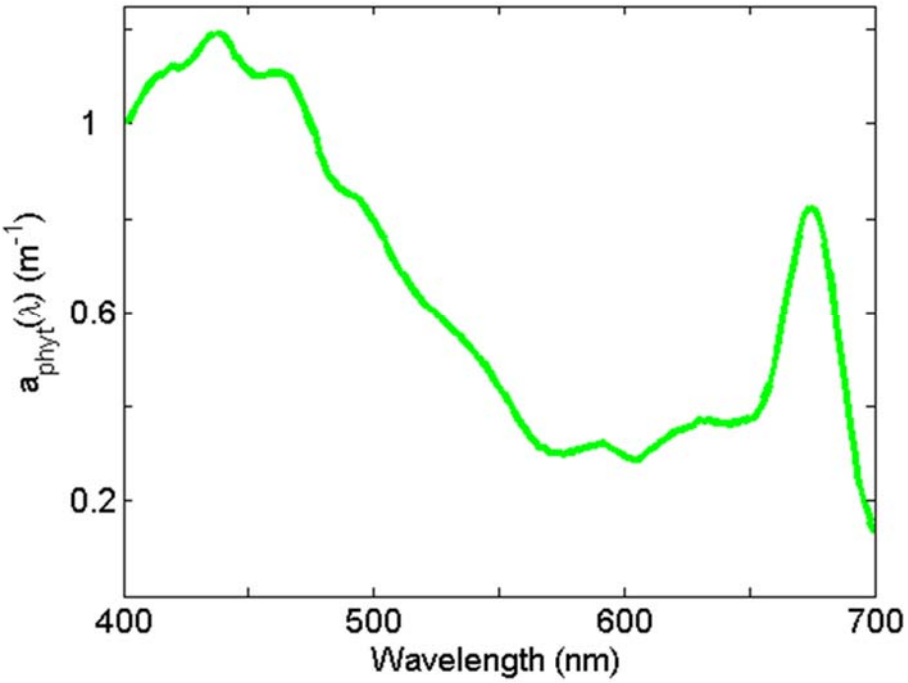


**Figure 1-3**: Generic phytoplankton absorption spectrum for mixed algal composition

### 1.3.3 Color Distortion

Compare with common photographs, underwater optical images suffer from poor visibility owing to the medium. Large suspended particles cause scattering in turbid water. Color distortion occurs because different wavelengths are attenuated to different degrees in water. Meanwhile, absorption of light in water substantially reduces its intensity. Furthermore, the random attenuation of light causes a hazy appearance as the light backscattered by water along the line of sight considerably degrades image contrast. So, underwater images contrast enhancement becomes more and more important [20].

Other issues such as artificial lighting, camera reflection, blurring is also affecting the quality of underwater images.

## 1.4 Contributions

Although sonar sensors are suitable for long-range distance imaging, due to the

principles of acoustic imaging, sonar images are low signal to noise ratio, low resolution and no colors. In order to acquire more detail information of underwater object, a short-range imaging system is required. In this situation, a photo vision sensor is used reasonably. However, the low contrast and color distortion of underwater images are still the major issues for practical applications. Therefore, this thesis will concentrate on the underwater optical images quality improvement.

The main contributions of this thesis can be summarized as follows.

1. A novel underwater imaging model that compensates for the attenuation along the propagation path is described. In addition, a robust locally adaptive filtering algorithm for enhancing underwater images is used. Compared with the traditional methods, the proposed method can obtain better results.

2. One color correction method for underwater image reconstruction was proposed. It is based on camera spectral response, color temperature and spectral power distribution. This method can recover the real scene actually.

3. Two methods for underwater image segmentation were proposed. The first one is automatic clustering weighted Fuzzy C Means based image segmentation method. It can segment the simple objects in water. The second one is fast active contour model based image segmentation method. Compare with the traditional level set methods, the processing speed of proposed method was improved by over 10 times.

## 1.5 Chapter Descriptions

In order to obtain high quality underwater images that can be adapted to the traditional image identification algorithms, this work aimed to construct an underwater image processing framework. Due to the special characteristic of underwater images, segment the image to several parts before directly perform a subject identification is thought an efficient way. And for obtaining a good underwater image segment result, the work to improve the quality of the image is necessary. Such work contains image

enhancement, color correction and noise reduction, etc. The experiments demonstrate that the proposed methods produced visually pleasing results, and the numerical image quality assessment also proved the effectiveness of this proposal. The organization of this thesis is as follows:

**Chapter 1** briefly reviews the characteristics and types of acoustic imaging and optical imaging technologies in the ocean. The traditional underwater imaging models and the drawbacks are introduced.

**Chapter 2** describes a novel underwater image enhancement method. The transmission is estimated by the proposed dual-channel prior. Then a robust locally adaptive filter algorithm for enhancing underwater images is used. In addition, the artificial light removal method is also proposed. Compared with the traditional methods, the proposed method obtains better images.

**Chapter 3** presents a color correction method to recover the distorted image colors. In the experiments, the proposed method recovers the distorted colors in real-time. The color corrected images have a reasonable noise level in their dark regions, and the global contrast is also well improved.

**Chapter 4** describes two methods for image segmentation. The first one is the automatic clustering Weighted Fuzzy C Means (WFCM) based segmentation method. It automatically obtains a reasonable clustering result for the underwater images with simple texture. The second method is fast Active Contour Model (ACM) based image segmentation method, which dramatically improves the calculation speed. Compare with the traditional methods, the processing speed is improved by over 10 times.

**Chapter 5** presents the conclusions of this work, summarizes the contributions and identifies some future research directions.

# Chapter 2

# Image Enhancement

## 2.1 Background

Recently, because of the energy exhausted in the world, ocean observing systems have been developed. Along with the development of underwater technologies, autonomous underwater vehicles (AUVs) and unmanned underwater vehicles (UUVs) have been used for deep-sea exploration. Sonars sensors also have been widely used for detecting and recognizing objects for underwater environments. However, for short-range identification, vision sensors must be used instead of sonars, because the images of sonars are low signal to noise ratio, low resolution [21].

Compared with normal images, underwater optical images suffer from poor visibility due to the medium, because the medium causes scattering, color distortion, and absorption. For example, large suspended particles cause scattering in turbid water. Color distortion occurs because different wavelengths are attenuated to different degrees in water. At the same time, light is absorbed in water and its intensity is reduced. The random attenuation of light causes a hazy appearance. In particular, underwater objects which 10 meters away from the camera lens are almost indistinguishable. In order to obtain clear images, image enhancement becomes very important [22].

A lot of researchers have developed many methods for underwater images enhancement. Schechner et al. [23] proposed a polarization filter to compensate for visibility degradation. Ancuti et al. [24] exploited an image fusion method in turbid water. Fattal et al. [25] proposed a graphic-theory-based independent-component analysis model to estimate the synthetic transmission and shading for recovering images. He et al. [26, 27] proposed the dark channel prior through over 5000 nature images, then used soft matting to refine the depth map, and finally obtained clear images. Nicholas et

al. [28] proposed a graph-cut method to refine the depth map. Chiang et al. [29] obtained the reconstructed image by using the improved dark channel prior model.

The aforementioned methods can enhance the images, but they have many shortcomings which reduce their practical applications. Firstly, the imaging equipment is difficult to use in practice. Secondly, multiple input images are required. At last, lack of intelligence. In [30] proposed a guided trigonometric filter to refine the depth map, but it does not consider the wavelength.

In this chapter, we focus on a single image and propose a novel underwater optical imaging model and a corresponding underwater image enhancement method. The performance of the proposed method is certified both experimentally and analytically.

## 2.2 Physical based Underwater Image Enhancement

### 2.2.1 Underwater Imaging Model

Atmospheric light and artificial light traveling through water are sources of illumination for underwater environment. Let us suppose that the energy attenuation model can be formulated as follows:

$$E_\lambda^W(x) = E_\lambda^A(x) \cdot Nrer(\lambda)^{D(x)} + E_\lambda^I(x) \cdot Nrer(\lambda)^{T(x)}, \quad \lambda \in \{r, g, b\}, \tag{2.1}$$

where $E_\lambda^W(x)$ is the amount of illumination at point $x$ of scene, $E_\lambda^A(x)$ is the amount of illumination of atmospheric light at point $x$, $E_\lambda^I(x)$ is the illumination of artificial light at point $x$, and *Nrer* is the normalized residual energy ratio [31]. In general underwater environment, *Nrer* has the following values:

$$N_{rer}(\lambda) = \begin{cases} 0.8 \sim 0.85 & if\ \lambda = 650 \sim 750 \mu m(red) \\ 0.93 \sim 0.97 & if\ \lambda = 490 \sim 550 \mu m(green) \\ 0.95 \sim 0.99 & if\ \lambda = 400 \sim 490 \mu m(blue) \end{cases}. \tag{2.2}$$

At point $x$, the artificial light is reflected with transmission $T(x)$ from the camera. $D(x)$ is the depth from water surface to scene. Color distortion and scattering occurs during this process. Supposing that the rate of absorption and scattering is $\rho_\lambda(x)$, the

illumination of ambient light $E_\lambda^\omega(x)$ is

$$E_\lambda^\omega(x)=\left(E_\lambda^A(x)\cdot Nrer(\lambda)^{D(x)}+E_\lambda^I(x)\cdot Nrer(\lambda)^{T(x)}\right)\cdot\rho_\lambda(x),\quad \lambda\in\{r,g,b\}. \tag{2.3}$$

According to the modified de-hazing model [32], the scene image $I_\lambda(x)$ can be formulated as follows:

$$I_\lambda(x)=\left[\left(E_\lambda^A(x)\cdot Nrer(\lambda)^{D(x)}+E_\lambda^I(x)\cdot Nrer(\lambda)^{T(x)}\right)\cdot\rho_\lambda(x)\right]\cdot t_\lambda(x) +\left(1-t_\lambda(x)\right)\cdot B_\lambda,\ \lambda\in\{r,g,b\}, \tag{2.4}$$

where the homogenous background $B_\lambda$ represents the part of the light reflected by the object, The residual energy ratio $t_\lambda(x)$ can be represented in terms of the energy of a light beam of wavelength $\lambda$ during it propagates through transmission $T(x)$ within the water, it is represented by $E_\lambda^{residual}(x)$ and $E_\lambda^{initial}(x)$, as follows:

$$t_\lambda(x)=\frac{E_\lambda^{residual}(x)}{E_\lambda^{initial}(x)}=10^{-\beta(\lambda)T(x)}=Nrer(\lambda)^{T(x)}, \tag{2.5}$$

where the normalized residual energy ratio $N_{rer}(\lambda)$ corresponds to the ratio of residual energy to initial energy for every unit of distance propagated, and $\beta(\lambda)$ is the extinction coefficient of mediums.

Consequently, substituting Eq. (2.5) in Eq. (2.4), then obtain:

$$I_\lambda(x)=\left[\begin{pmatrix}E_\lambda^A(x)\cdot Nrer(\lambda)^{D(x)}+\\ E_\lambda^I(x)\cdot Nrer(\lambda)^{T(x)}\end{pmatrix}\cdot\rho_\lambda(x)\right]\cdot Nrer(\lambda)^{T(x)} +\left(1-Nrer(\lambda)^{T(x)}\right)\cdot B_\lambda,\ \lambda\in\{r,g,b\}. \tag{2.6}$$

The above equation contains the light scattered and the wavelength attenuation. Once water surface-scene depth $D(x)$ and transmission $T(x)$ are known, a clean image can be obtained. Figure 2-1 shows a schematic of the proposed underwater optical imaging model. In order to enhance the image, we consider the processing flowchart shown in Figure 2-2.

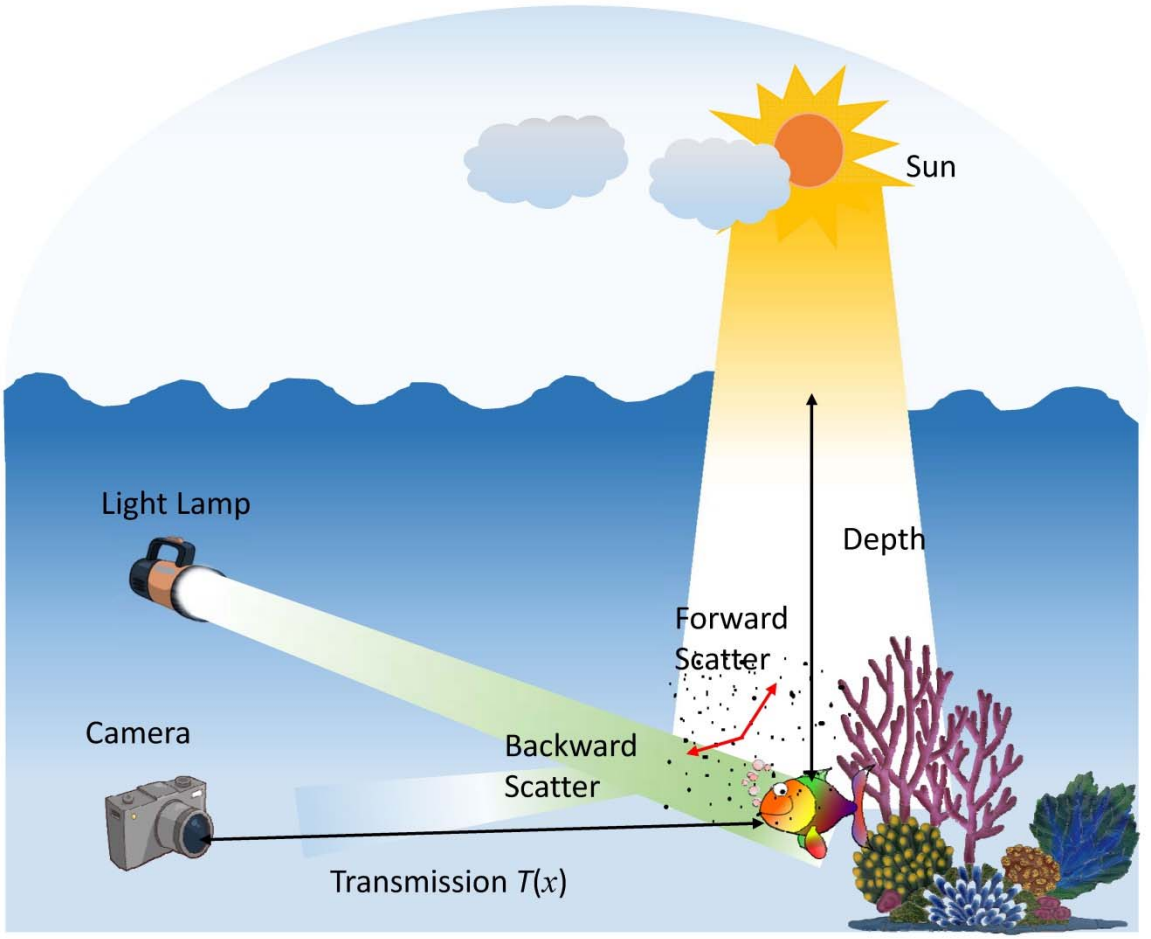


**Figure 2-1**: Schematic of the underwater imaging model.

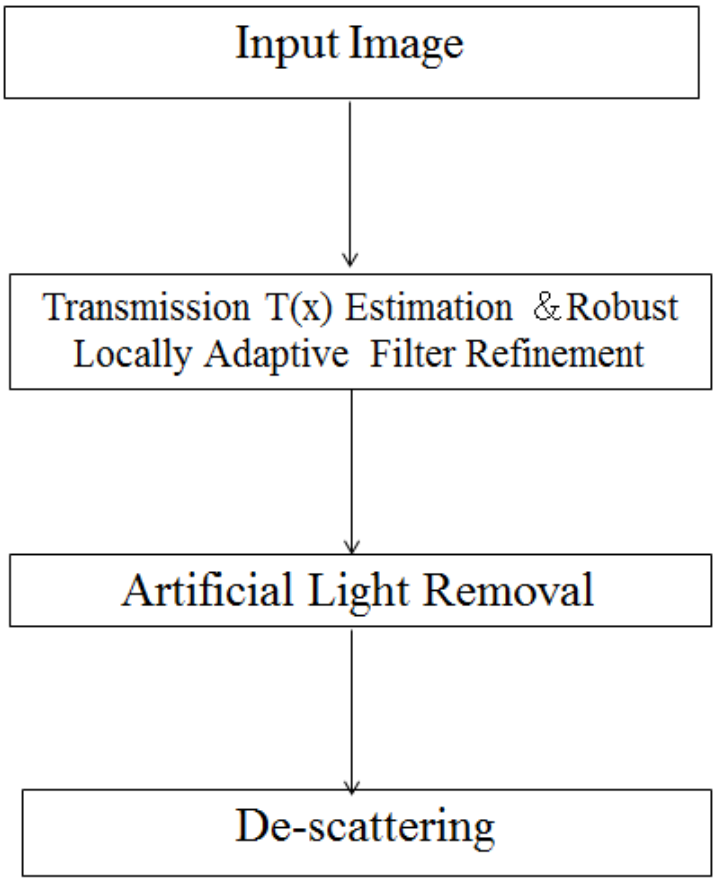


**Figure 2-2:** Pipeline of underwater image enhancement.

### 2.2.2 De-scattering

**(I) Transmission *T*(*x*) Estimation**

The authors of [33] found that the red color channel of RGB channels is the dark channel, because the red color channel is with the lowest pixel value. During our experiments, we found that in turbid water, the lowest pixel value of the RGB channels is not always the red color channel; the blue color channel sometimes is with the lowest pixel value. The light of red wavelength is easily absorbed when it propagates in water, but sometimes the blue channel is absorbed more quickly than the red channel (See Figure 2-3). So, in this paper, the dual-channel (red and blue) values are taken as a rough transmission.

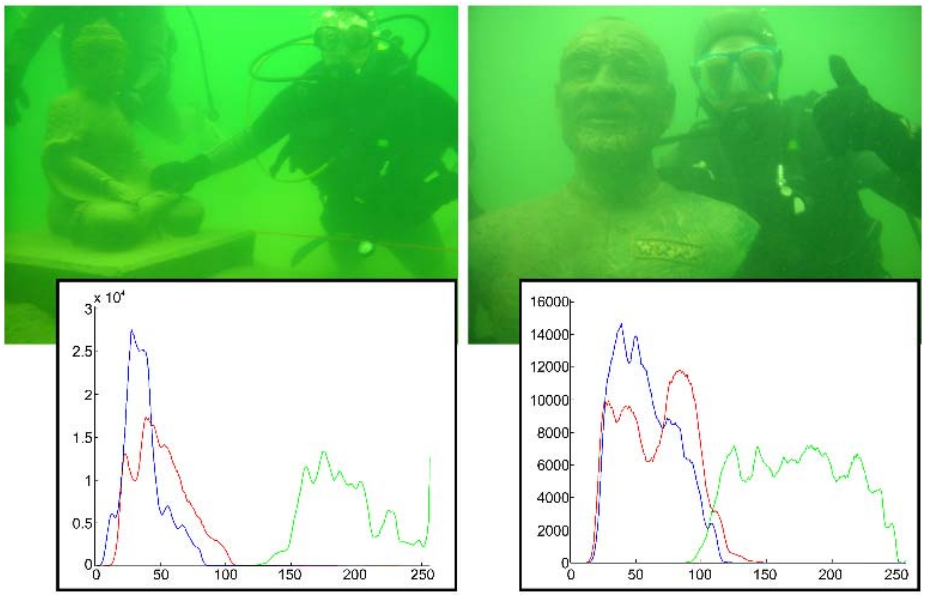


**Figure 2-3:** RGB histograms of underwater images.

As indicated in Eq. (2.6), we suppose the non-scatter image $J_\lambda(x)$ reflected from point $x$ is

$$J_\lambda(x)=\left(E_\lambda^A(x)\cdot Nrer(\lambda)^{D(x)}+E_\lambda^I(x)\cdot Nrer(\lambda)^{T(x)}\right)\cdot\rho_\lambda(x),\quad \lambda\in\{r,g,b\}. \tag{2.7}$$

We define the underwater dark channel $J_{dark}(x)$ for the underwater non-scatter image $J_\lambda(x)$ as

$$J_{dark}(x)=\min_{\lambda}\min_{y\in\Omega(x)}J_\lambda(y),\ \lambda\in\{r,b\}. \tag{2.8}$$

If point $x$ is at a part of the foreground object, the value of the minimum dual channel is very small [34]. And $y$ is a point of a local patch $\Omega(x)$. Applying the min operation to a local patch $\Omega(x)$ on the scattered image $I_\lambda(x)$, we have

$$\min_{y\in\Omega(x)}\left(I_\lambda(y)\right)=\min_{y\in\Omega(x)}\left\{\begin{matrix}J_\lambda(y)\cdot Nrer(\lambda)^{T(y)}+\\ \left(1-Nrer(\lambda)^{T(y)}\right)\cdot B_\lambda\end{matrix}\right\},\quad \lambda\in\{r,b\}. \tag{2.9}$$

Because $B_\lambda$ is the homogeneous background light and the residual energy ratio $Nrer(\lambda)^{T(y)}$ on the small local patch $\Omega(x)$ surrounding point $x$ is essentially a constant $Nrer(\lambda)^{T(x)}$, the min operation on the second term on the right-hand side of Eq. (2.9)

can be removed to obtain

$$\min_{y\in\Omega(x)}\left(I_\lambda(y)\right)=\min_{y\in\Omega(x)}J_\lambda(y)\cdot Nrer(\lambda)^{T(x)}+\left(1-Nrer(\lambda)^{T(x)}\right)\cdot B_\lambda,\ \lambda\in\{r,b\}. \tag{2.10}$$

We rearrange the above equation and perform on more min operation among all channels as follows:

$$\begin{aligned}&\min_\lambda\left\{\frac{\min_{y\in\Omega(x)}\left(I_\lambda(y)\right)}{B_\lambda}\right\}=\\&\min_\lambda\left\{\frac{\min_{y\in\Omega(x)}J_\lambda(y)}{B_\lambda}\cdot Nrer(\lambda)^{T(x)}\right\}+\\&\min_\lambda\left(1-Nrer(\lambda)^{T(x)}\right),\ \lambda\in\{r,b\}.\end{aligned} \tag{2.11}$$

The first term on the right-hand side of Eq. (2.11) is dark channels which equal to 0. Consequently, as follows.

$$\max_\lambda(Nrer(\lambda)^{T(x)})=1-\min_\lambda\left\{\frac{\min_{y\in\Omega(x)}(I_\lambda(y))}{B_\lambda}\right\},\lambda\in\{r,b\}. \tag{2.12}$$

Finally, the transmission $T(x)$ can be represented as following.

$$T(x)=\ln\left(1-\min_\lambda\left\{\frac{\min_{y\in\Omega(x)}\left(I_\lambda(y)\right)}{B_\lambda}\right\}\right)/\ln\max\left\{Nrer(\lambda)\right\},\lambda\in\{r,b\}. \tag{2.13}$$

**(II) Transmission *T*(*x*) Refinement using Locally Adaptive Filter**

In previous section, we roughly estimated the transmission $T(x)$. But, the transmission $T(x)$ contains mosaic effects. So, we use a robust locally adaptive filter to reduce the mosaic effects then obtain more smoothly transmission $\hat{T}(x)$. In this section, we introduce a constant time algorithm for robust locally adaptive filter.

The basic fast Laplacian filter has been considered as an effective way for removing "outliers". The basic local Laplacian filter can promise the image details or tone. The local Laplacian filter extends to overcome the traditional Laplacian filter which can appropriate for constructing edge-preserving. Furthermore, local Laplacian filter can be simply implemented with basic manipulations. Here we first introduce the principle of

basic local Laplacian filter. Let the input image $I$ with N×N size and its intensity is defined as a scalar function $I(x,y)\epsilon[0,1]$ after normalization. $G_l$ is processed by Gaussian image pyramid [35], and $L_l$ is obtained by Laplacian image pyramid. The relationship between these two pyramids:

$$\begin{cases} L_l = G_l - (G_{l+1})_{\uparrow} & l = 1 \cdots n-1 \\ L_n = G_n & l = n \end{cases} \tag{2.14}$$

where $()_{\uparrow}$ corresponds to the upsampling operation. Local Laplacian filter also defines a remapping function $r$ on the normalized image intensity:

$$r(i,g) = \begin{cases} g + sign(i-g)\left(|i-g|/\sigma_r\right)^{\alpha} & if\ |i-g| \le \sigma_r \\ g + sign(i-g)\left(\beta\left(|i-g| - \sigma_r\right) + \sigma_r\right) & if\ |i-g| > \sigma_r \end{cases} \tag{2.15}$$

where $r(i,g)$ is a scalar function and the aim of this function is, given a center $g$, to remap $i$ at the position of ($x_l$, $y_l$, $l$) in $\{G_l\}$ into $r(i,g)$, where $i$ and $g$ are both scalar image intensities. $\alpha$ and $\beta$ are two key parameters that control the local laplacian filtering [36] effects. The former parameter $\alpha$ generates effects of smoothing or enhancing, while the later parameter $\beta$ generates effects of tone mapping.

To obtain the transmission $\hat{T}(x)$, firstly, we consider a two-level pyramid in the transmission and corresponding input image $I(x)$. Assuming that, the pixel $p$ has a single neighbor $q$ in input image and ignores the spatial weight $\overline{G}_{\sigma_p}$. The refined depth disparity with the filter becomes:

$$\hat{T}_p = T_p + f(I_{\lambda,q} - T_p)(I_{\lambda,q} - T_p) \tag{2.16}$$

We highlight the role of pixel differences by subtracting $I_q$ on both sides. Assuming that function $f$ is symmetric, which is always the case in practice. Then we obtain:

$$\hat{T}_p - I_{\lambda,q} = (T_p - I_{\lambda,q}) - f(T_p - I_{\lambda,q})(T_p - I_{\lambda,q}) \tag{2.17}$$

Defining $h(x) = [1\text{-}f(x)]x$, we get:

$$\tilde{r}(T) = g + h(T - I_{\lambda}) \tag{2.18}$$

where $\tilde{r}$ is the remapping function. $h$ defines the desired refined depth disparity gradients. We compute the pyramid for the intermediate image $\{L[\tilde{d}]\}$ and copy the corresponding coefficient to the transmission $\hat{T}(x)$. Then, we get the final result [37].

The refined transmission image is shown in Figure 2-4.

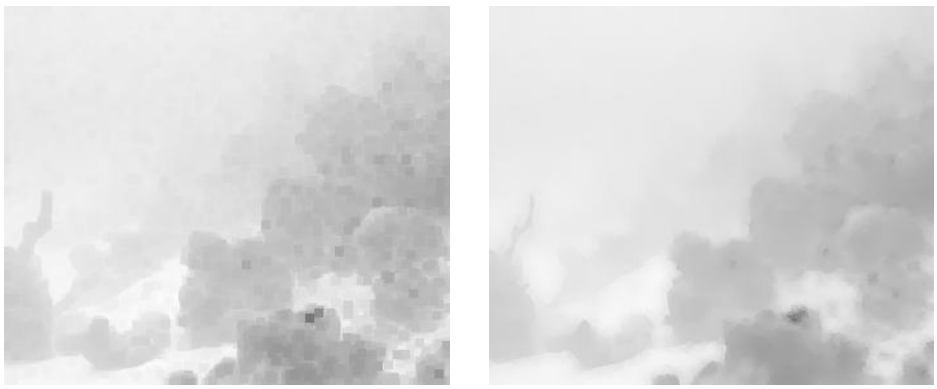

(a) (b)

**Figure 2-4:** Transmission refinement image using the robust locally adaptive filter. (a) Input rough transmission image. (b) Refined transmission image.

**(III) Artificial Light Removal**

In underwater environment, the main source of light is the sunlight. The underwater background is brighter than the foreground, because the underwater background corresponds to light transmitted without being absorbed or reflected by objects. The mean luminance indicates that a supplementary light source is existence [38]. The foreground and background of an image can be segmented as follows:

$$area-type(x)=\begin{cases} foreground\ if\ \hat{T}(x)>\sigma \\ background\ if\ \hat{T}(x)\le\sigma \end{cases} \tag{2.19}$$

where $\sigma$ is the threshold distance and usually $\sigma = 0.5$.

**(IIII) De-scattering**

In the above subsection, we obtained the refined Transmission $\hat{T}(x)$. In order to remove scatter effects, first, we should obtain the rate of absorption and scattering $\rho_\lambda(x)$. For this, we use the least squares solution:

$$\begin{aligned} &\rho_\lambda(x)=\left(J_\lambda(x)^T\cdot J_\lambda(x)\right)^{-1}\cdot J_\lambda(x)^T \\ &\cdot\left(E_\lambda^A(x)\cdot Nrer(\lambda)^{D(x)}+E_\lambda^I(x)\cdot Nrer(\lambda)^{\hat{T}(x)}\right), \\ &\lambda\in\{r,g,b\}. \end{aligned} \tag{2.20}$$

After removing the effects of artificial light, the Eq. (2.6) is written as:

$$I_\lambda(x)=E_\lambda^A(x)\cdot Nrer(\lambda)^{D(x)}\cdot\rho_\lambda(x)\cdot Nrer(\lambda)^{\hat{T}(x)} +\left(1-Nrer(\lambda)^{\hat{T}(x)}\right)\cdot B_\lambda,\ \lambda\in\{r,g,b\}. \tag{2.21}$$

Finally, the de-scattered image is written as:

$$\begin{aligned}\tilde{J}_\lambda(x)&=\frac{I_\lambda(x)-\left(1-Nrer(\lambda)^{\hat{T}(x)}\right)\cdot B_\lambda}{Nrer(\lambda)^{\hat{T}(x)}}\\&=E_\lambda^A(x)\cdot Nrer(\lambda)^{D(x)}\cdot\rho_\lambda(x)\cdot Nrer(\lambda)^{\hat{T}(x)},\\&\lambda\in\{r,g,b\}.\end{aligned} \tag{2.22}$$

## 2.3 Experiments and Discussions

There are generally two methods to evaluate image quality. One is the subjective evaluation of the observer. By human eyes to observe image quality, then determine the difference between the images. However, it is greatly affected by subjective image. The other is by calculating the Peak Signal-to-Noise Ratio (*PSNR*) or Mean Square Error (*MSE*) to evaluate the quality of image. *PSNR* and *MSE* are objective evaluation criteria. *PSNR* is the ratio between the maximum possible power of a signal and the power of corrupting noise. It is often defined through the *MSE*. Let give a noise-free image $f(x,y)$, and $f_0(x,y)$ is the noisy approximation, *MSE* is defined as follows:

$$MSE=\frac{1}{mn}\sum_{x=0}^{m-1}\sum_{y=0}^{n-1}\left[f(x,y)-f_0(x,y)\right]^2. \tag{2.23}$$

The *PSNR* is defined as follows:

$$PSNR=10\log_{10}\left(\frac{L^2}{MSE}\right), \tag{2.24}$$

Where $L$ is the maximum possible pixel value of an image. Generally, the larger value of *PSNR*/*MSE*, the better quality of the image is.

Recently, a multi-scale *SSIM* method was proposed for image quality assessment. The define of *SSIM* is as follows, and $C_1$, $C_2$ are small constants.

$$SSIM(\mathrm{x},\mathrm{y})=\frac{(2\mu_A\mu_B+C_1)(2\sigma_{AB}+C_2)}{(\mu_A^2+\mu_B^2+C_1)(\mu_A^2+\mu_B^2+C_2)}. \tag{2.25}$$

Where signal $A$ and $B$ are input signal, $\mu_A$ is the mean of $A$, $\sigma_A$ is the variance of $A$ and $\sigma_{AB}$ is the covariance of $A$ and $B$. The parameters of relative importance $\alpha$, $\beta$, $\gamma$ are equal to 1. The larger value of *SSIM* is, the better quality of image is.

In our experiments, the proposed method is evaluated both analytically and experimentally by real-world images and utilizing ground-truth water tank images. We also compare the proposed method with currently used state-of-the-art methods.

*A. Comparison of Conventional Methods*

In the first experiment, we used a *Windows XP* PC running on an *Intel Core 2 Duo* CPU (2.0 GHz) with 2 GB RAM. The size of each image is 600 × 424 pixels. We compare the proposed method with other methods for removing scatter from real-world underwater image.

Figure 2-5 shows the results of different de-scattering methods. In Figure 2-5(b), Bazeille's method causes serious distortion. The drawback of Fattal's method is that the background and foreground need to be manually determined, which is difficult in practical applications (Figure 2-5(c)). Nicholas's graph-cut-based method (Figure 2-5(d)) requires a lot of processing time and computational effort, and the processed image is blurred. In comparison with He et al.'s method in Figure 2-5(e), some regions are too dark (e.g. the right corner of the coral reefs) and haze is not removed (e.g. the center of the image). In Xiao's model (Figure 2-5(f)), we find some unresolved scatter around the coral reefs; furthermore, selecting parameters for fusion in that method is difficult. In Ancuti's model, there are some hazy appearances (Figure 2-5(g)). Chiang's de-scattered image has color shifting (Figure 2-5(h)). In comparison with the conventional methods, we can find that the proposed method achieve visual pleasing result (Figure 2-5(i)).

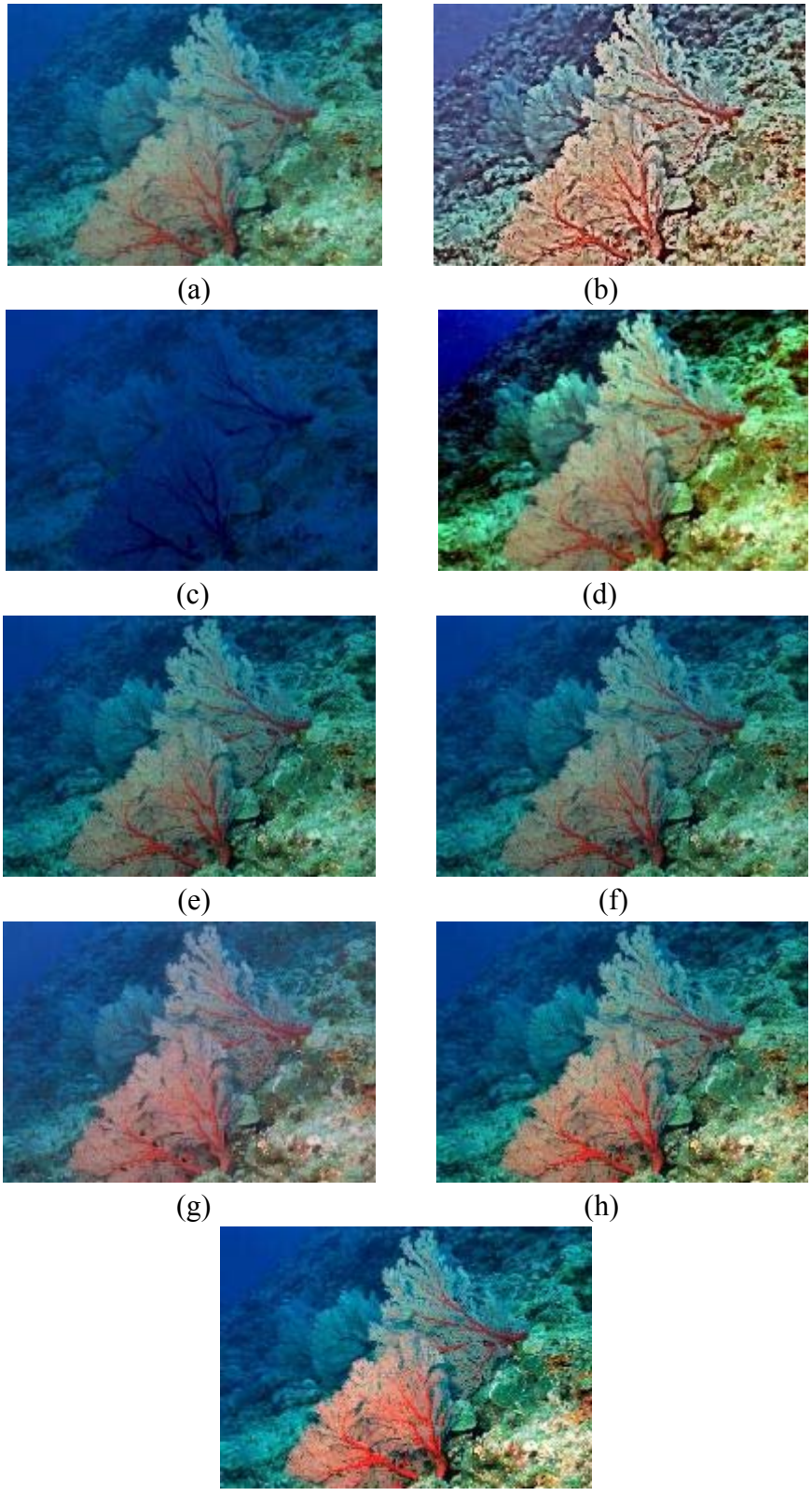

**Figure 2-5:** Results of different enhancement methods. (a) Input Image. (b) Bazeille's method; (c) Fattal's method; (d) Nicholas's method; (e) He's method; (f) Xiao's

method ; (g) Ancuti's method; (h) Chiang's method; and (i) the proposed method.

In addition to the visual analysis mentioned above, we also conducted a quantitative analysis, primarily from the perspective statistics measurement of the images. This analysis includes High-Dynamic Range Visual Difference Predictor2 Image Quality Assessment (HDR-VDP2-IQA), Peak Signal to Noise Ratio (*PSNR*), and structural similarity index (*SSIM*). In this paper, the inverse $Q_{MOS}$ value is between 100 (best) and 0 (worst) for measuring without a ground-truth images assessment. Table 2-1 lists the PSNR values, the inverse $Q_{MOS}$ values, and the *SSIM* values measured for different methods. These results indicate that the proposed method not only work well for de-scattering but also work with lower computation time.

**TABLE 2-1:** Comparative Analysis of Different De-scattering Methods (see Figure 2-5)

| Methods | *PSNR* | $Q_{MOS}$ | *SSIM* | CPU Time [s] |
|---|---|---|---|---|
| Bazeille | 13.0844 | 19.8556 | 0.2061 | 1.98 |
| Fattal | 11.7316 | 19.2204 | 0.4581 | 11.48 |
| Nicholas | 18.9630 | 43.0762 | 0.7763 | 167.86 |
| He | 23.2120 | **77.8366** | 0.9642 | 116.22 |
| Xiao | 24.5089 | 66.0857 | 0.9493 | 104.98 |
| Ancuti | 27.0414 | 39.8664 | 0.9074 | 62.76 |
| Chiang | 27.3216 | 71.7899 | 0.9597 | 38.73 |
| Proposed | **27.7829** | 77.6780 | **0.9698** | **28.68** |

*B. Water Tank Simulation*

We also tested the proposed method using simulations in a water tank. In this simulation, we used an *OLYMPUS Tough TG-2* underwater camera, a water surface-scene depth of 0.3 meters. Figure 2-6 illustrates the results with different methods that a color chart is placed in a water tank. In this experiment, Bazeille's, Fattal's, Chiang's, and Ancuti's results have color distortion. In results of He et al., Nicholas et al., and Xiao et al., there are some scatter remained. As shown in Figure 2-6,

compare with other methods, the proposed method effectively removes haze appearance. Therefore, we conclude that the proposed method can enhance the underwater image well.

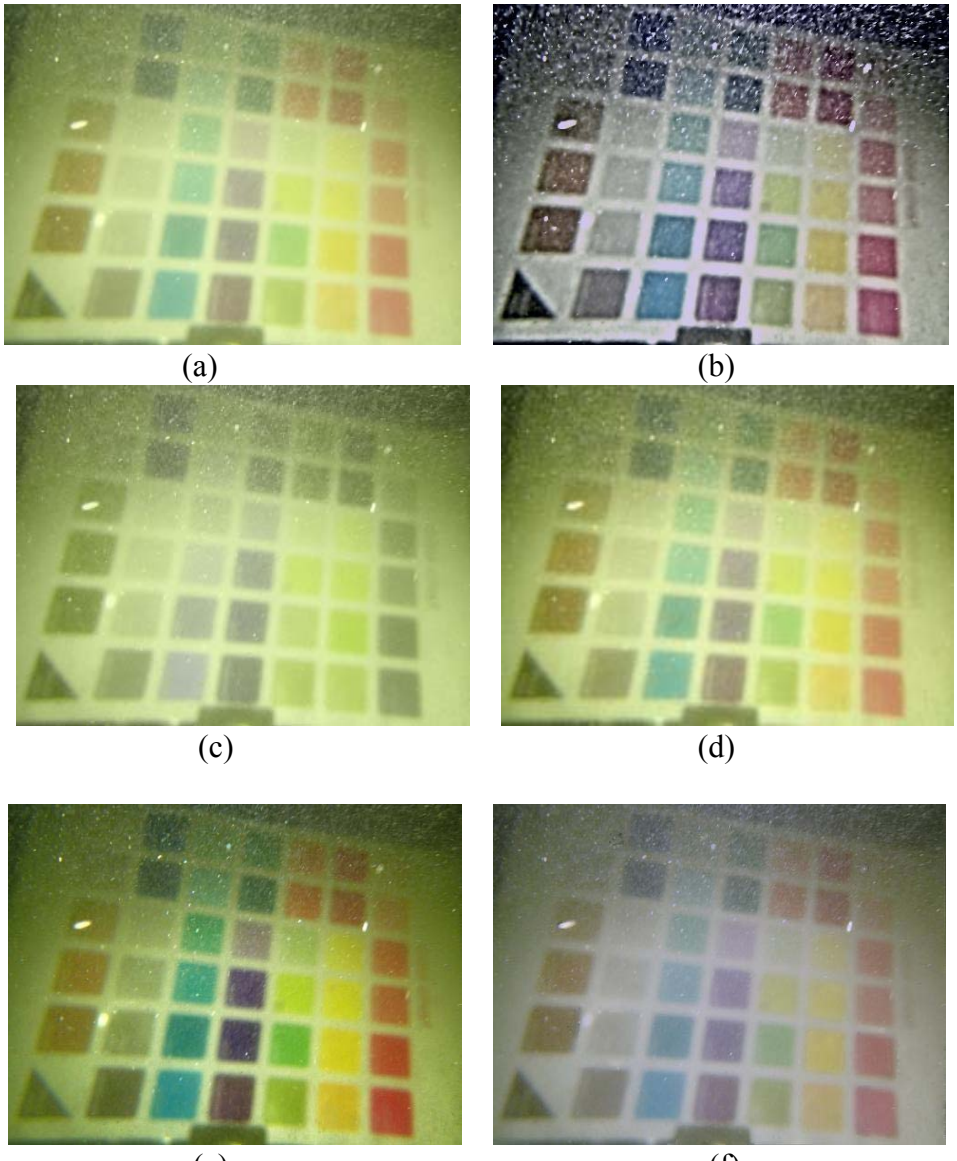

(a) (b) (c) (d) (e) (f)

**Figure 2-6:** Simulation results of a color chart in turbid water using different methods. (a) Turbidity image; (b) Bazeille's method; (c) Fattal's method; (d) Nicholas's method; (e) He's method; (f) Xiao's method; (g) Ancuti's method; (h) Chiang's method; (i) Proposed method; (j) Color chart. (*Cont.*)

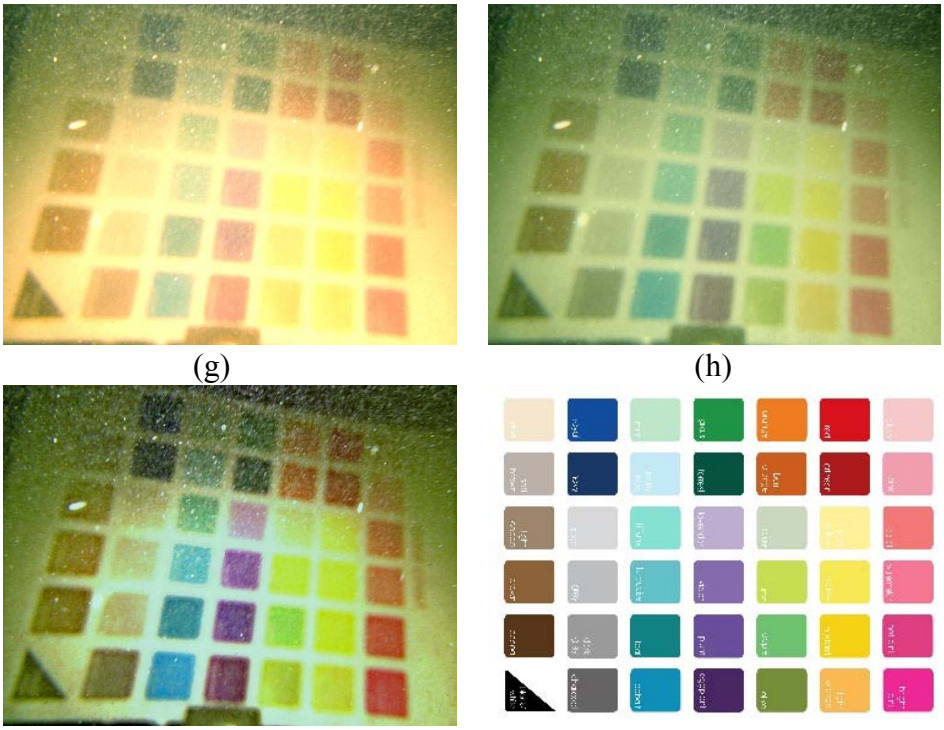

(g) (h)

(i) (j)

**Figure 2-6:** Simulation results of a color chart in turbid water using different methods. (a) Turbidity image; (b) Bazeille's method; (c) Fattal's method; (d) Nicholas's method; (e) He's method; (f) Xiao's method; (g) Ancuti's method; (h) Chiang's method; (i) Proposed method; (j) Color chart.

Figure 2-7 to Figure 2-12 illustrates the results with different methods in different turbidity water. In this experiment, we made a linear scale of 6 turbidity steps ranging from clean to heavily haze by adding deep-sea soil to the seawater (from 1 mg/L to 200 mg/L). Some scatters remained in He et al.'s results and Gibson et al.'s results, while Tarel et al.'s results and Fattal et al.'s results show color distortion. As shown in the last row, the proposed method can remove the haze appearance effectively.

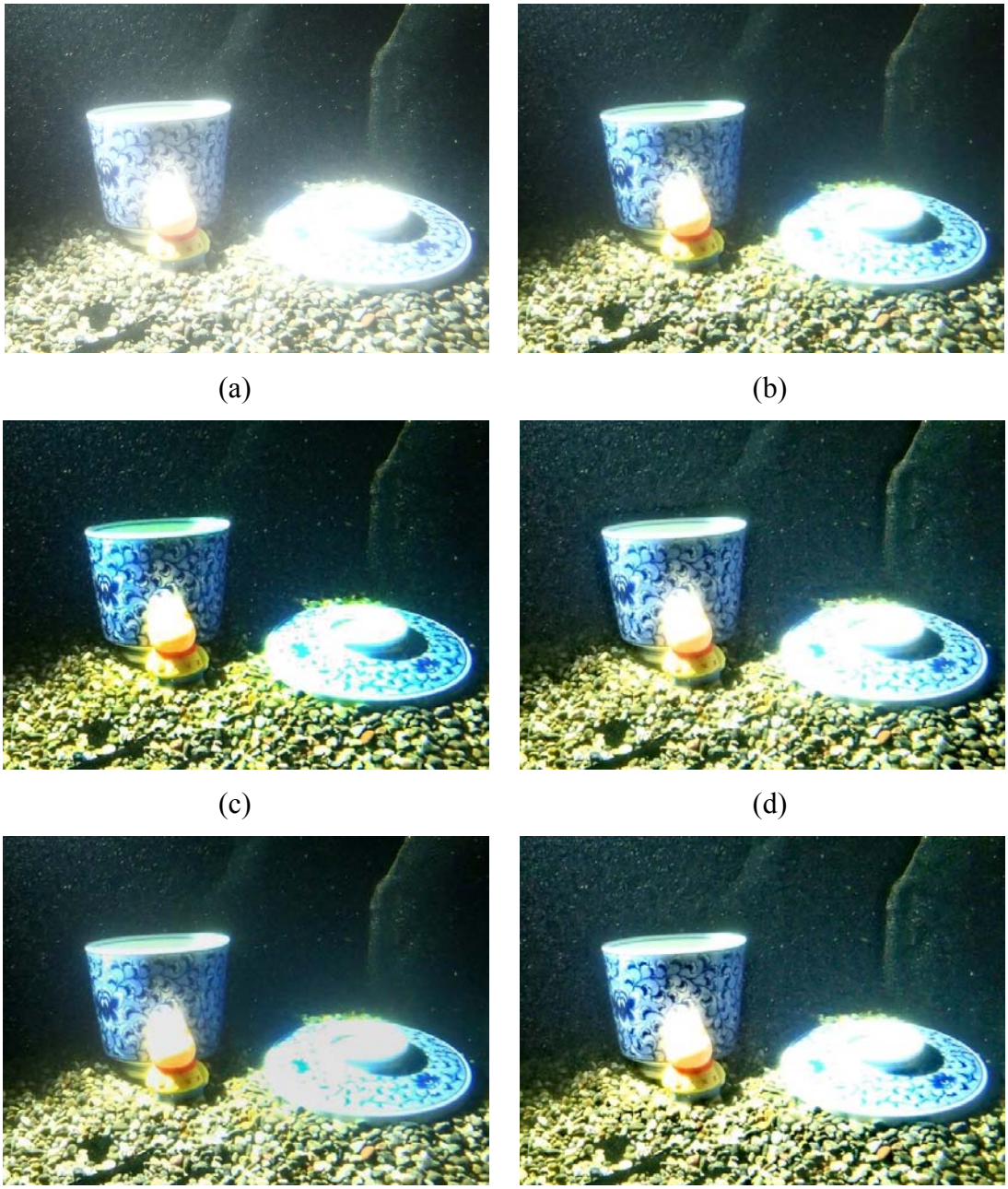

(a) (b)

(c) (d)

(e) (f)

**Figure 2-7**: Toy and cup (1 mg/L). (a) Input image; (b) He et al.'s method; (c) Tarel et al.'s method; (d) Gibson et al.'s method; (e) Fattal et al.'s method; and (f) The proposed method.

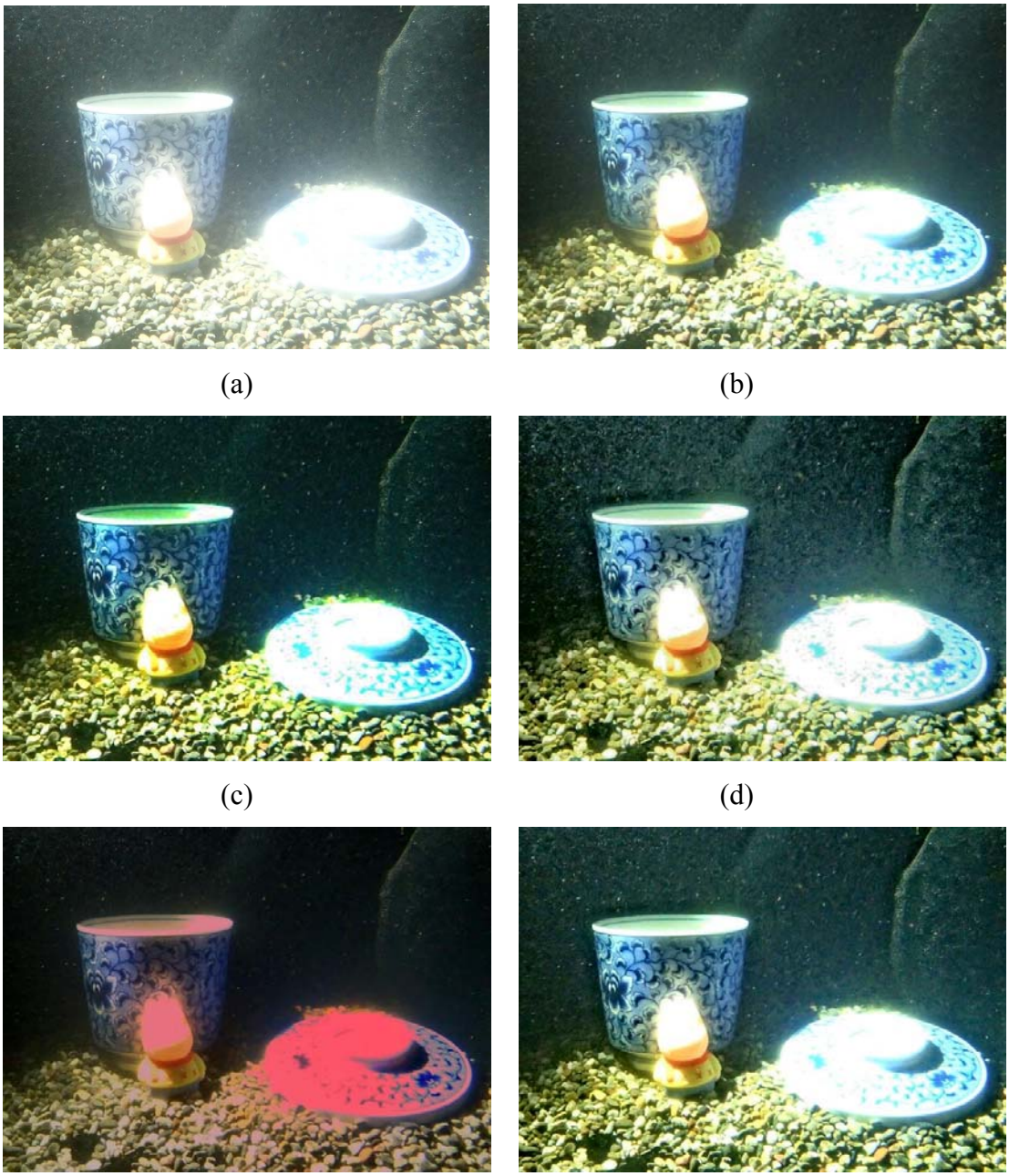

(a) (b)

(c) (d)

(e) (f)

**Figure 2-8**: Toy and cup (2 mg/L). (a) Input image; (b) He et al.'s method; (c) Tarel et al.'s method; (d) Gibson et al.'s method; (e) Fattal et al.'s method; and (f) The proposed method.

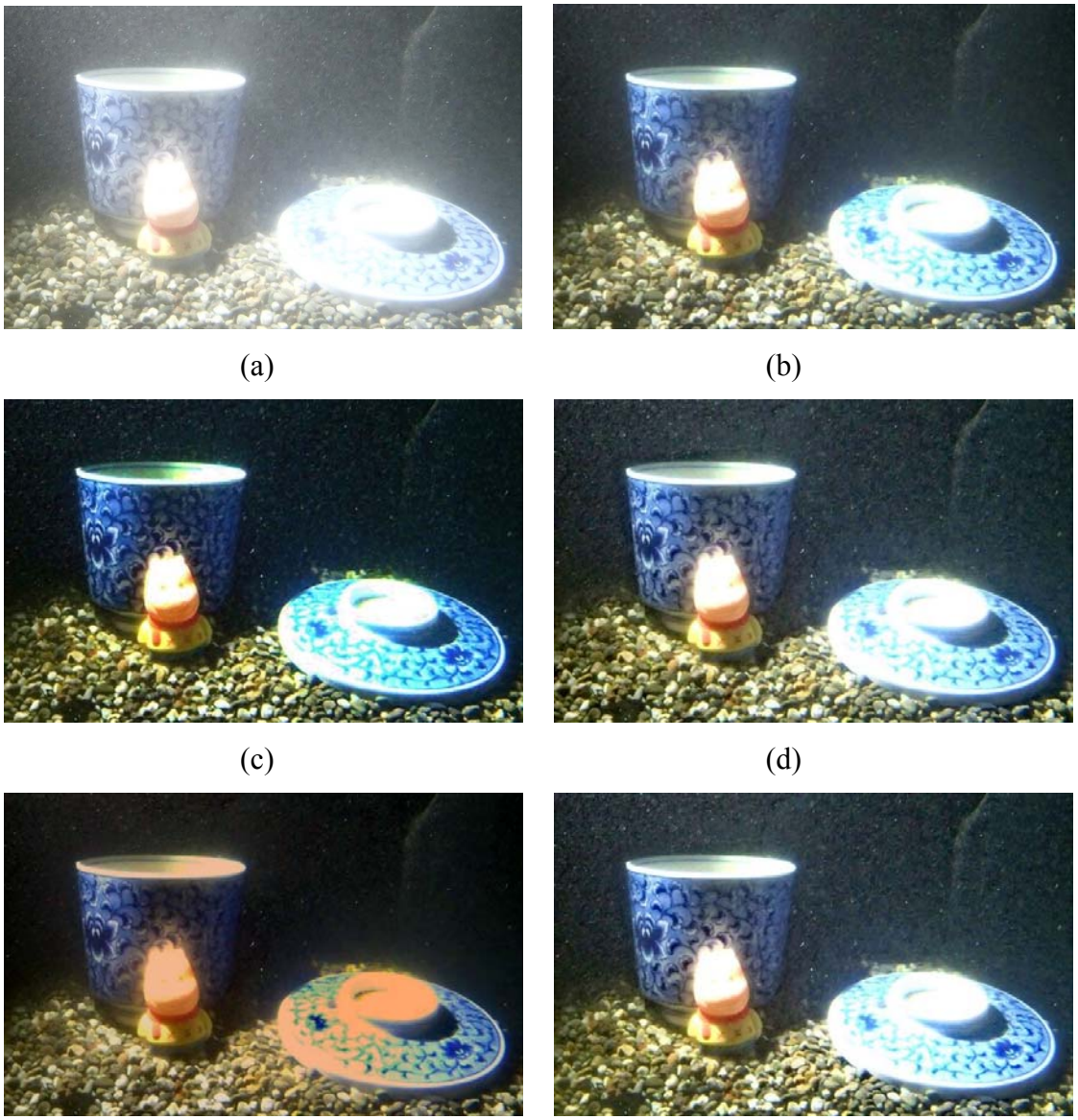

(a) (b)

(c) (d)

(e) (f)

**Figure 2-9**: Toy and cup (10 mg/L). (a) Input image; (b) He et al.'s method; (c) Tarel et al.'s method; (d) Gibson et al.'s method; (e) Fattal et al.'s method; and (f) The proposed method.

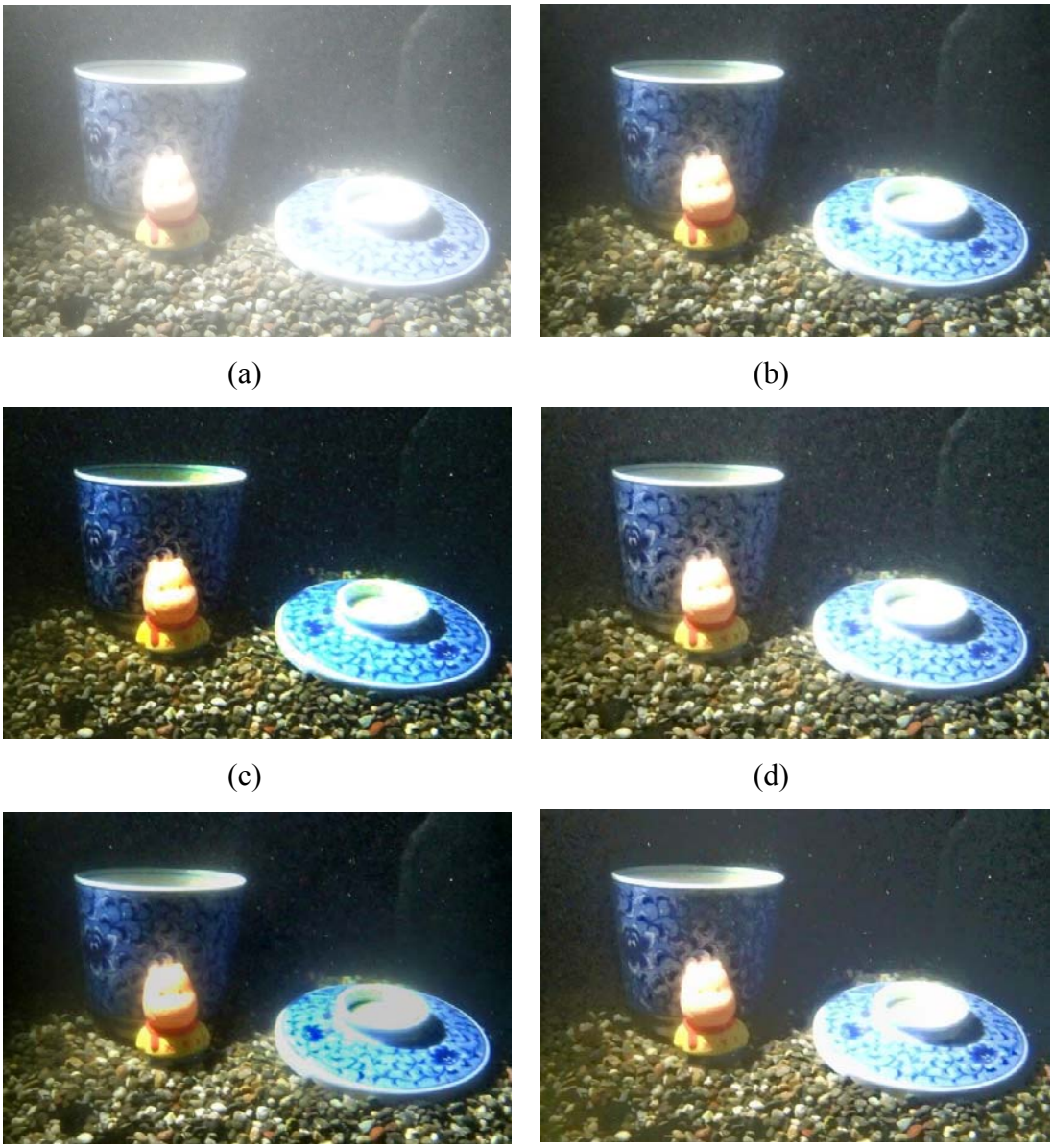

(a) (b)

(c) (d)

(e) (f)

**Figure 2-10**: Toy and cup (20 mg/L). (a) Input image; (b) He et al.'s method; (c) Tarel et al.'s method; (d) Gibson et al.'s method; (e) Fattal et al.'s method; and (f) The proposed method.

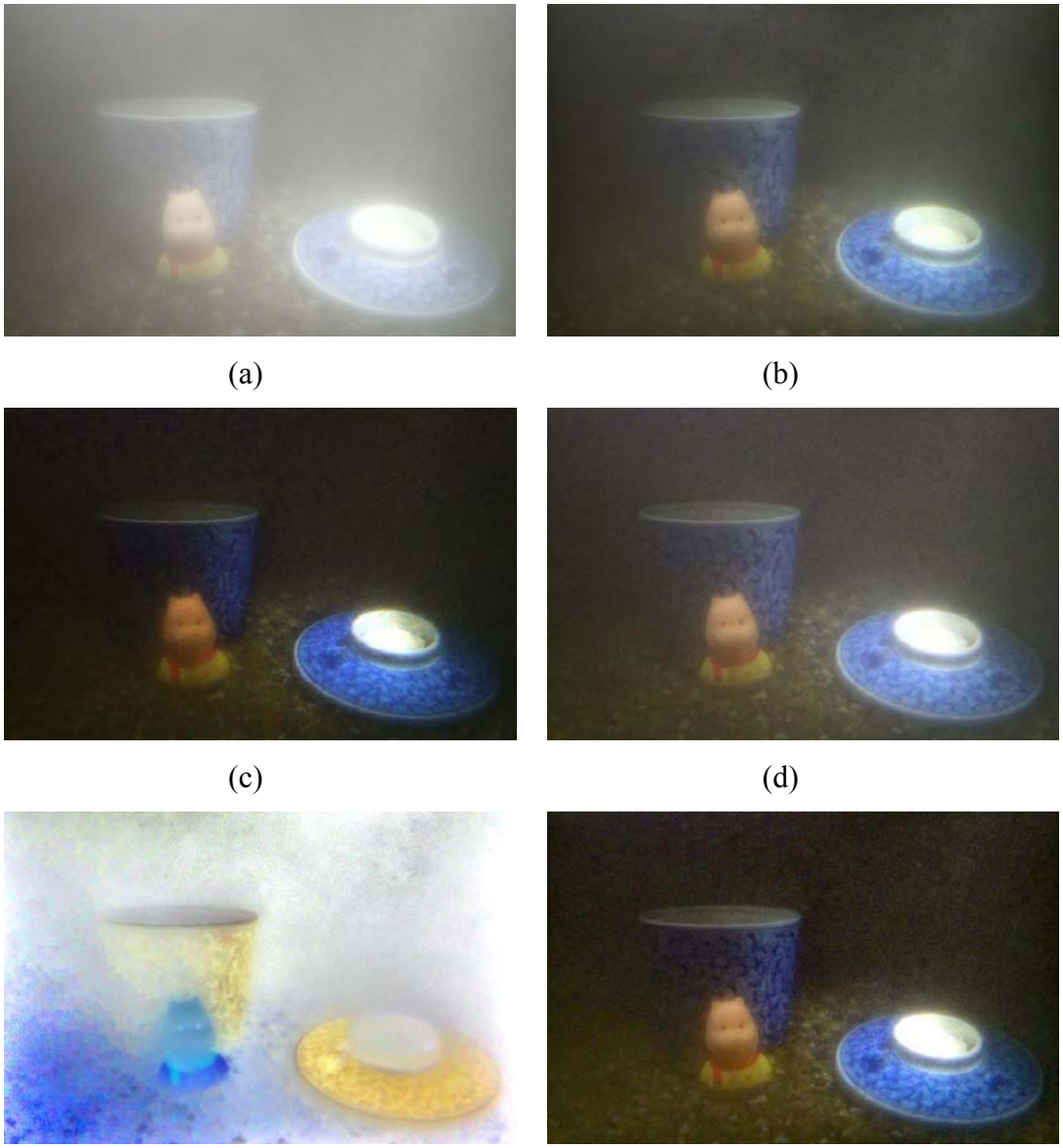

(a) (b)

(c) (d)

(e) (f)

**Figure 2-11**: Toy and cup (100 mg/L). (a) Input image; (b) He et al.'s method; (c) Tarelet al.'s method; (d) Gibson et al.'s method; (e) Fattal et al.'s method; and (f) The proposed method.

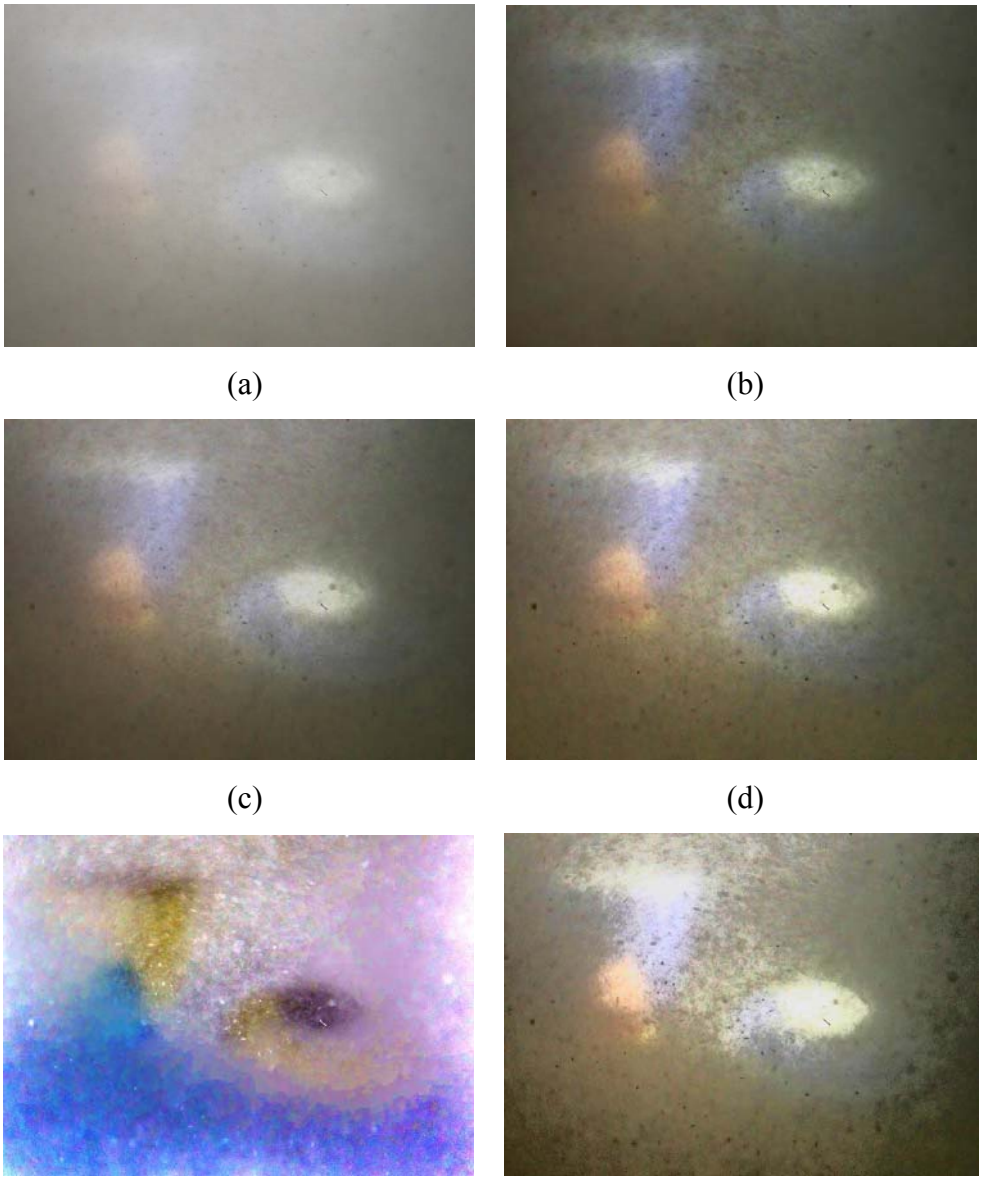

(a) (b) (c) (d) (e) (f)

**Figure 2-12**: Toy and cup (200 mg/L). (a) Input image; (b) He et al.'s method; (c) Tarel et al.'s method; (d) Gibson et al.'s method; (e) Fattal et al.'s method; and (f) The proposed method.

In this chapter, we take the Contrast-to-noise Ratio (*CNR*) to evaluate image quality. *CNR* is a measure of highly distorted images' quality. It subtracts a term before determining the ratio. This measure is important when an image displays a significant bias, such as that from haze. An image may exhibit high intensity although the features of the image are washed out as a result of haze. This image may display a high SNR

metric but a low CNR metric. Therefore, CNR can measure image quality more efficiently than SNR can. The value of CNR is between 100 (best) and 0 (worst).

We test 6 groups of underwater images with different water turbidity (from 1 mg/L to200mg/L). Figure 2-13 shows the CNR values of different methods with different water turbidity. The average CNR of the proposed method is nearly improved 5 than the state-of-the-art models. From the above analysis, we can find that the proposed method performs well than the other methods both in visual assessment and qualities analysis.

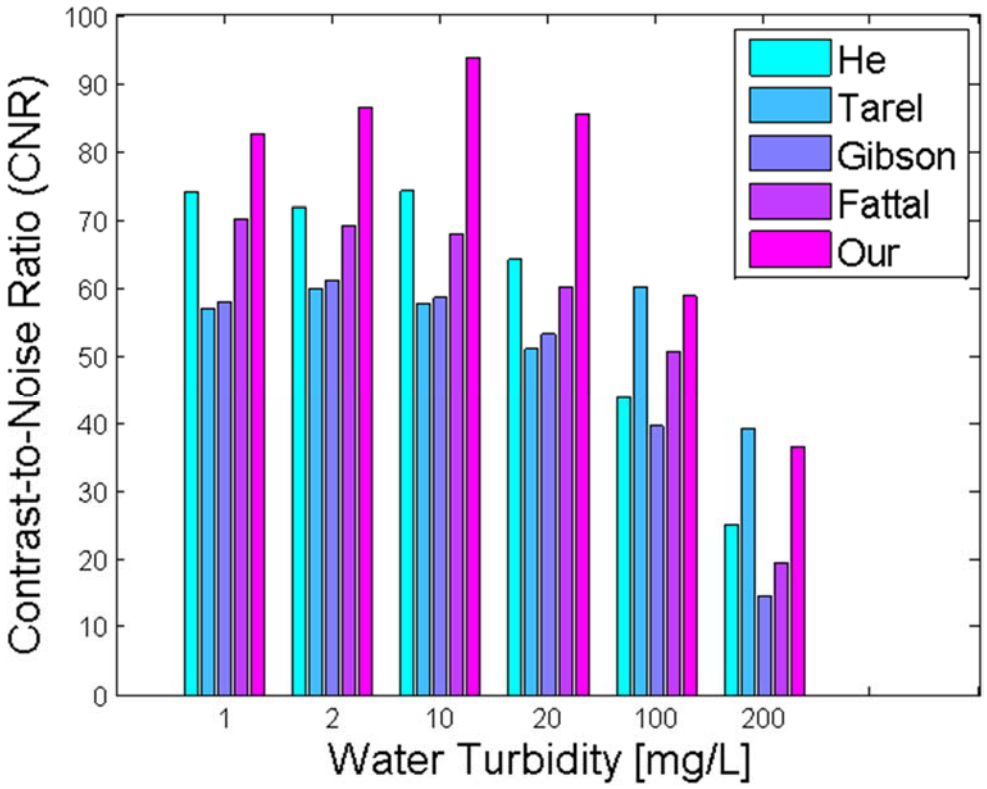


**Figure 2-13:** CNR values of different methods in different water turbidity.

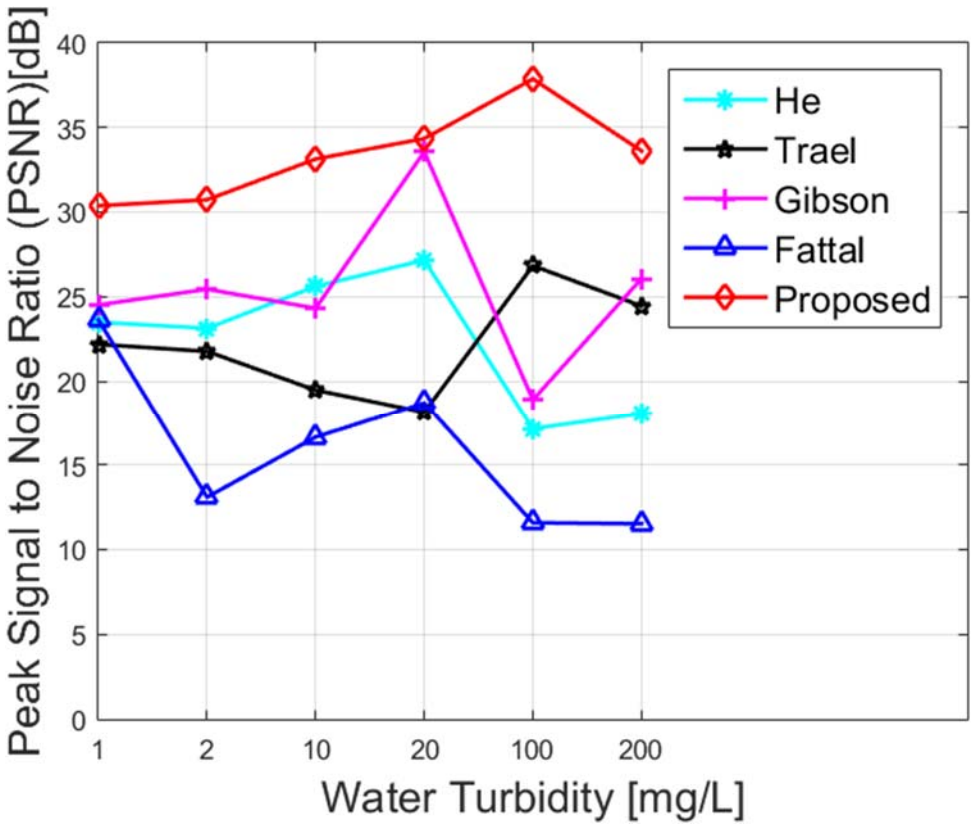


**Figure 2-14:** PSNR values of different methods in different water turbidity.

Figure 2-14 shows the PSNR value of different methods in different water turbidity. We can find that with different water turbidity (from 1 mg/L to 200 mg/L), the PSNR value of the proposed method is larger than the other methods. Therefore, the quality of proposed method is better than the other methods.

## 2.4 Conclusion

In this chapter, we proposed and successfully implemented novel enhancement techniques for underwater optical image processing. The contribution is that, we proposed dual-channels priors to estimate the rough transmission $T(x)$, and then a robust locally adaptive filter which has the benefits of edge-preserving and noise removing, is used to refine the transmission accurately. The other contribution is an artificial light removal method was proposed. The experiments show that compare with the state-of-the-art methods, the proposed method cost lower computing time. The value of PSNR, SSIM and CNR shows that the proposed method is with better image quality.

The proposed method improves the contrast of the underwater images. Therefore, we can conclude that the proposed method is suitable for underwater optical imaging.

# Chapter 3

# Color Correction

## 3.1 Background

For underwater short range optical imaging, because of scattering and absorption, the captured images are faded. In recent years, there are many image methods for improving the underwater image quality. Most of these methods consider the image formation process without a prior knowledge of the environment. These methods are usually simple. They also can obtain a good result.

With the water depth increases, the colors are faded depending on the wavelength. Generally, red color disappears at the depth of 3 meters. The orange color is lost at the depth of 5 meters. Almost all of the yellow color will disappears at the depth of 10 meters. The blue- green colors travel the longest in the water due to its shortest wavelength. Consequently, the underwater images are featured by blue-green color. Compare with the spectrum of blue or green, the red spectrum is always easier to be absorbed in water. Therefore, it is important to recover the true color of the imaged scene.

Two decades ago, Bazeille et al. [39] proposed an image pre-process method for recovering the scene. It reduces underwater perturbations and improves image quality. It is composed of several successive independent processing steps which correct non uniform illumination; the homomorphic filter is used to correct non-uniform illumination and to enhance contrasts of the image. Assume the captured image is a function of illumination and the reflectance as

$$f(x,y) = i(x,y)r(x,y), \tag{3.1}$$

where $f(x, y)$ is the captured image, $i(x, y)$ is the illumination multiplicative factor, and $r(x, y)$ is the reflectance function. Taking the logarithm to achieve,

$$\ln(f(x,y)) = \ln(i(x,y)) + \ln(r(x,y)). \tag{3.2}$$

Compute FFT of the Eq. (3.2),

$$F(w_x, w_y) = I(w_x, w_y) + R(w_x, w_y). \tag{3.3}$$

Then, utilize the Highpass Filters to the coefficients of FFT. And after inverse-FFT, the filtered images are obtained. However, the processed images also contain some noise.

Chambah et al. [40] proposed a color correction method based on adaptive contrast enhancement (ACE) model. ACE is a perceptual approach inspired by some adaptation mechanisms of the human vision system, in particular lightness constancy and color constancy. ACE was applied on videos taken in aquatic environment. Images were taken from the tanks of an aquarium. Inner parameters of the ACE algorithm were properly tuned to meet the requirements of image and histogram shape naturalness and to deal with these kinds of aquatic images.

As mentioned before, the pre-processed images may be too dark, so we introduce a novel fast color correction method for contrast enhancement. Bertalmio *et al.* [41] showed that by replacing $s_\alpha$ with a polynomial, the summation in $R$ can be decomposed into convolutions, reducing the complexity to $O(N^2 \log N)$. We change the $min\{max\{\alpha q, -1\}, 1\}$ with an odd polynomial approximation,

$$s_\alpha(q) \approx \sum_{m=1}^{M} c_m q^m \tag{3.4}$$

The input image is assumed to [0, 1], so the argument $q$ is guaranteed to be between -1 and 1. By the Stone-Weierstrass theorem, the continuous function $s_\alpha(q)$ can be uniformly approximated on [-1, 1] by a polynomial with any desired precision. In order tor reduce the computational cost, we select the coefficients $c_m$ to minimize the maximum absolute error over [-1, 1],

$$\min_{c} \max_{q\in[-1,1]} \left| s_\alpha(q) - \sum_{m=1}^{M} c_m q^m \right| \tag{3.5}$$

The optimal $c$ can be found using the Remez algorithm. Then it is possible to decompose $R$ into a sum of convolution,

$$
\begin{aligned}
R(x) &= \sum_{y\in \mathrm{T}^2} w(x-y)\sum_{m=1}^{M} c_m (I(x)-I(y))^m \\
&= -\sum_{y\in \mathrm{T}^2} w(x-y)\sum_{m=1}^{M} c_m (I(y)-I(x))^m \\
&= -\sum_{y\in \mathrm{T}^2} w(x-y)\sum_{m=1}^{M} c_m \sum_{n=0}^{m} \binom{m}{n} I(y)^n (-I(x))^{m-n} \\
&= \sum_{n=0}^{M} \left( \sum_{m=n}^{M} c_n \binom{m}{n} (-1)^{m-n+1} I(x)^{m-n} \right) \sum_{y\in \mathrm{T}^2} w(y-x) I(y)^n \\
&= \sum_{n=0}^{M} a_n(x)(w * I^n)(x)
\end{aligned}
\tag{3.6}
$$

where * is cyclic convolution over the whole torus $T^2$. If $x = y$, $w(x\text{-}y) = 0$, else, $w(x\text{-}y) = 1/d(x\text{-}y)$. So, the convolutions can be efficiently computed with DCT transforms instead of FFT transforms with $O(N^2 logN)$. We apply the $\alpha$ACE to correct the underwater distorted images. In this research, we set $\alpha$ =5, the polynomial $q$ is equal to $5.64305564q\text{-}28.94026159q^3+74.52401661q^5\text{-}83.54012582q^7+ 33.39343065q^9$.

Iqbal et al. [42] presented an underwater image enhancement method using an integrated color model. The proposed method is processed as the following steps: firstly, contrast stretching of RGB channels is used to equalize the color contrast of the images. Second, saturation and intensity stretching of HSI is applied to increase the true color and solve the problem of un-uniform lighting. The blue color component in the image is controlled by the saturation and intensity to create the range from pale blue to deep blue. The contrast ratio is therefore controlled by decreasing or increasing its value.

Arnold Bos et al. [43] presented a complete color correction framework for underwater images. They investigated the possibility of noises present in underwater images by using a combination of de-convolution and enhancement methods. At first, a contrast equalization method is proposed to remove backscattering, attenuation and lighting inequalities. Let $I(i, j)$ as the original image and $I_{LP}(i, j)$ is its low-pass version, a contrast-equalized version of $I$ is $I_{eq} = I / I_{LP}$. Contrast equalization is followed by histogram clipping and expansion of the image range. The method is suitable because backscattering is a slowly varying spatial function. Backscattering is considered as the first noise addressed in the algorithm, however, contrast equalization

also corrects the effect of the exponential light attenuation with distance. Floating particles and miscellaneous quantification errors are suppressed by a generic self-tuning wavelet-based algorithm. The use of the adaptive smoothing filter significantly improves edge detection in the images.

In this chapter, we propose a physical based color correction method. The spectral response function [44] of a camera maps the relative sensitivity of the camera imaging system as a function of the wavelength of the light.

## 3.2 Camera Spectral Characteristics

At first, let us review the concept of camera spectral characteristics. In order to process images from digital color cameras, it is necessary to know the spectral response properties of the camera's sensors. In addition, the intrinsic color quality of an image depends on the spectral characteristics of the camera sensors used. Consequently, it is important to measure the camera sensors' spectral response functions [45].

The output of a camera sensor $r$ to the spectral response of the sensor $s(\lambda)$, the incident radiant power $i(\lambda)d\lambda$, the exposure time $e$ and the measurement noise $n$:

$$r = \Gamma\left(e\int_{\lambda_l}^{\lambda_h} s(\lambda)i(\lambda)d\lambda + n\right). \tag{3.7}$$

The wavelengths $\lambda_l$ and $\lambda_h$ are the limits beyond which the spectral response of the sensor is 0. The function $\Gamma$ is a static non-linearity.

To perform calculations, a sampled version of Eq. (3.6) describes the entire calibration data set. Let **r**, **g**, and **b** be vectors representing the *R*, *G*, *B*, readings to a series of narrowband lights. The vectors have $K_r$, $K_g$ and $K_b$ entries respectively, one for each of the narrowband stimuli used to calibrate the corresponding sensor. Let the full spectrum of the *i-th* narrowband light be $s_i(\lambda)$, and let the unknown camera spectral sensitivities be $c_r(\lambda)$, $c_g(\lambda)$, $c_b(\lambda)$. Form Eq. (3.6) we can obtain:

$$\mathrm{r} = \Gamma\left(\begin{bmatrix} e(1)\sum_j c_r(\lambda_l + j\Delta\lambda)s_1(\lambda_l + j\Delta\lambda)\Delta\lambda \\ \vdots \\ e(i)\sum_j c_r(\lambda_l + j\Delta\lambda)s_i(\lambda_l + j\Delta\lambda)\Delta\lambda \\ \vdots \\ e(K_r)\sum_j c_r(\lambda_l + j\Delta\lambda)s_{K_r}(\lambda_l + j\Delta\lambda)\Delta\lambda \end{bmatrix} + \mathbf{n}\right) \tag{3.8}$$

where **n** is a vector representing measurement noise with variation about the average dark noise value, $\Delta\lambda$ is the wavelength sampling of the radiometric measurements, and $e(i)$ is the exposure setting for the *i-th* measurement [46].

The illumination incident on the camera is narrow band. This fact may be used to approximate Eq. (3.7) by

$$\mathrm{r} = \Gamma\left(\begin{bmatrix} e(1)\sum_j c_r(\lambda_1)s_1(\lambda_l + j\Delta\lambda)\Delta\lambda \\ \vdots \\ e(i)\sum_j c_r(\lambda_i)s_i(\lambda_l + j\Delta\lambda)\Delta\lambda \\ \vdots \\ e(K_r)\sum_j c_r(\lambda_{K_r})s_{K_r}(\lambda_l + j\Delta\lambda)\Delta\lambda \end{bmatrix} + \mathbf{n}\right) \tag{3.9}$$

where $\lambda_i$ is the wavelength of the peak of the *i*-th incident illumination. By ignoring the noise variability, the sensor response function $c_r(\lambda_i)$ as

$$c_r(\lambda_i) = \frac{\Gamma^{-1}(r_i) - n}{e(i)\sum_j s_i(\lambda_l + j\Delta\lambda)\Delta\lambda} \tag{3.10}$$

where $r_i$ is the *i*-th component of **r**.

The camera spectral response of *Olympus uTough 8000* at different lighting is shown in Figure 3-1. Figure 3-2 shows the camera spectral response of *Canon 70D MarkII*.

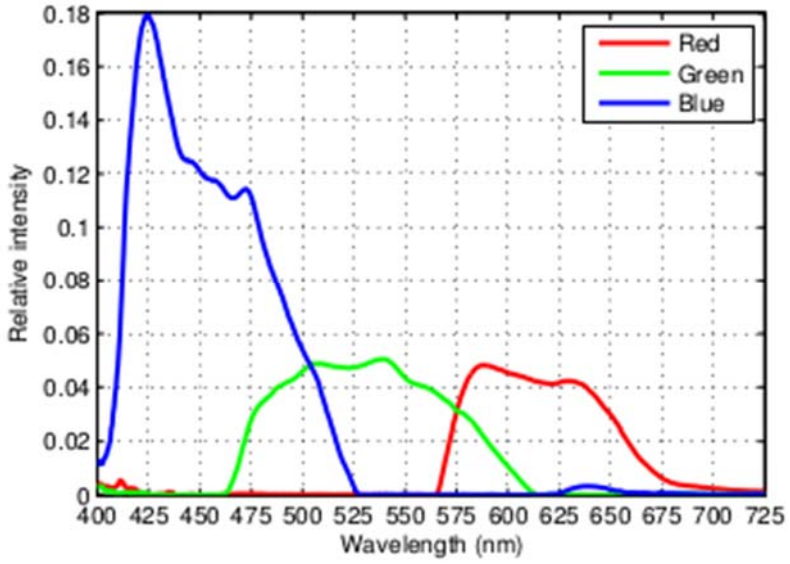


(a)

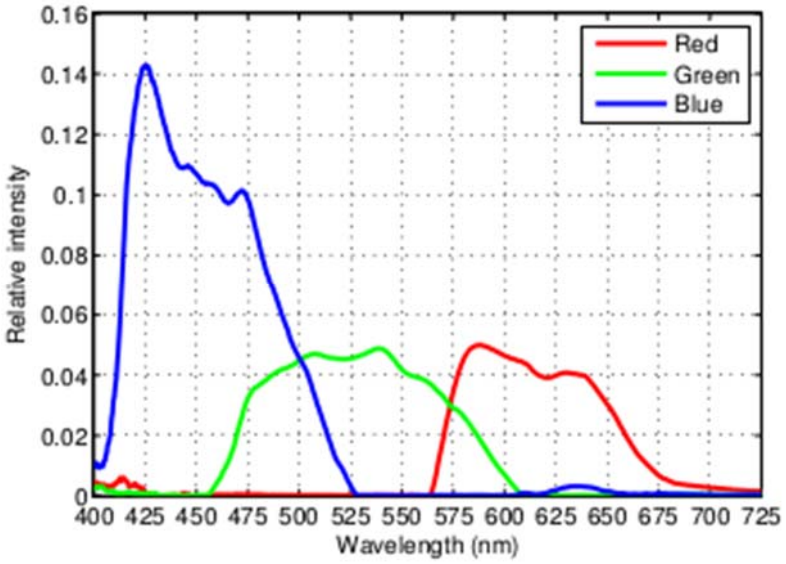


(b)

**Figure 3-1:** Camera Spectral Response of Olympus uTough 8000. (a) Auto white balance lighting. (b) Fluorescent white balance lighting. (c) Incandescent white balance lighting. (d) Sunny white balance lighting. (*Cont.*)

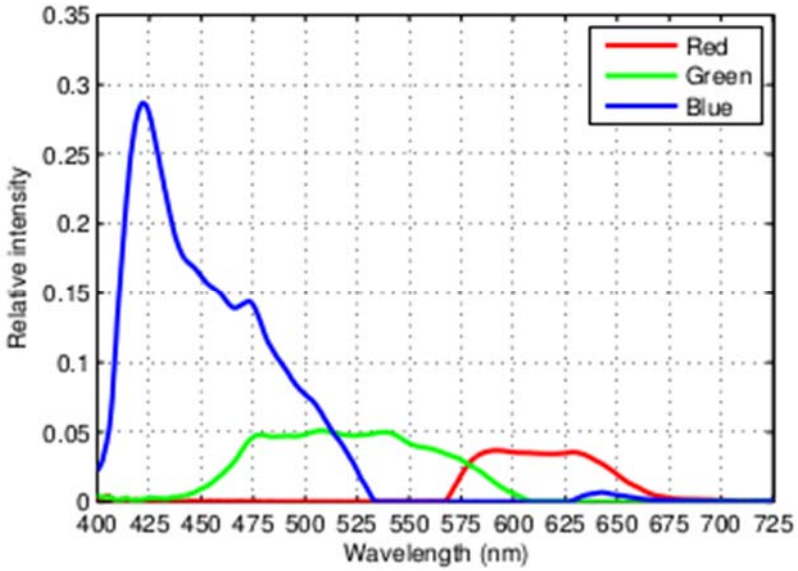


(c)

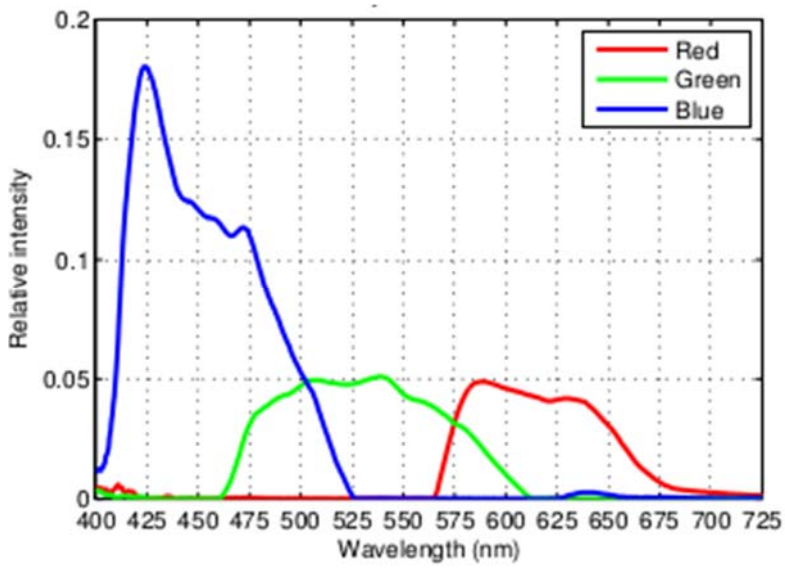


(d)

**Figure 3-1:** Camera Spectral Response of Olympus uTough 8000. (a) Auto white balance lighting. (b) Fluorescent white balance lighting. (c) Incandescent white balance lighting. (d) Sunny white balance lighting.

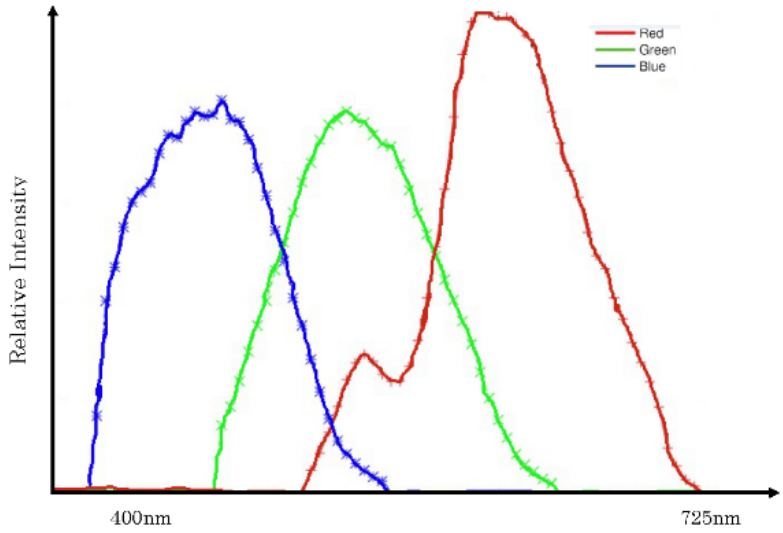


**Figure 3-2:** Camera Spectral Response of Canon 70D MarkII.

## 3.3 Color Temperature

### 3.3.1 Color Temperature

Color temperature is an important factor of color appearance. Corrected color temperature (CCT) is a metric that relates the appearance of a light source to the appearance of a theoretical black body heated to high temperatures. As the black body gets hotter, it turns red, orange, yellow, white and blue. The CCT of a light source, given in Kelvin (K), is the temperature at which the heated black body most closely matches the color of the light source in question.

As can be seen from Figure 3-3 and Figure 3-4, the preferences appear to be influenced more by the lamp spectral power distribution than by their CCTs. In daylight, the CCT is about 7400K. However, in De Luxe WarmWhite, the CCT is about 2950K. At the time that these studies were conducted, “deluxe” fluorescent lamps had CRI values of 90 or so, but warm white fluorescent lamps with their halo phosphate phosphors had CRI values as low as 50.

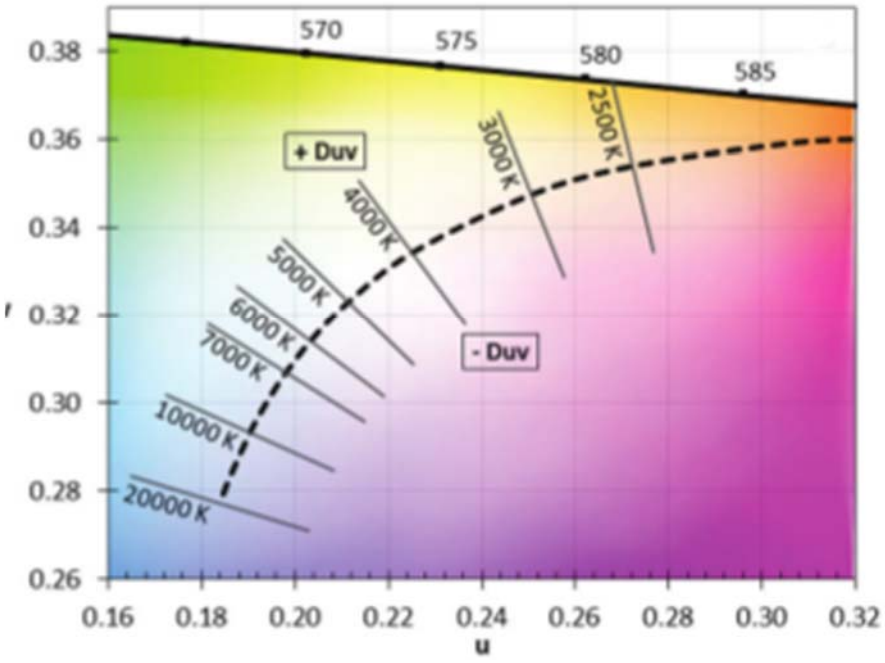


**Figure 3-3:** A close up of the CIE1960 chromaticity diagram of constant CCT.

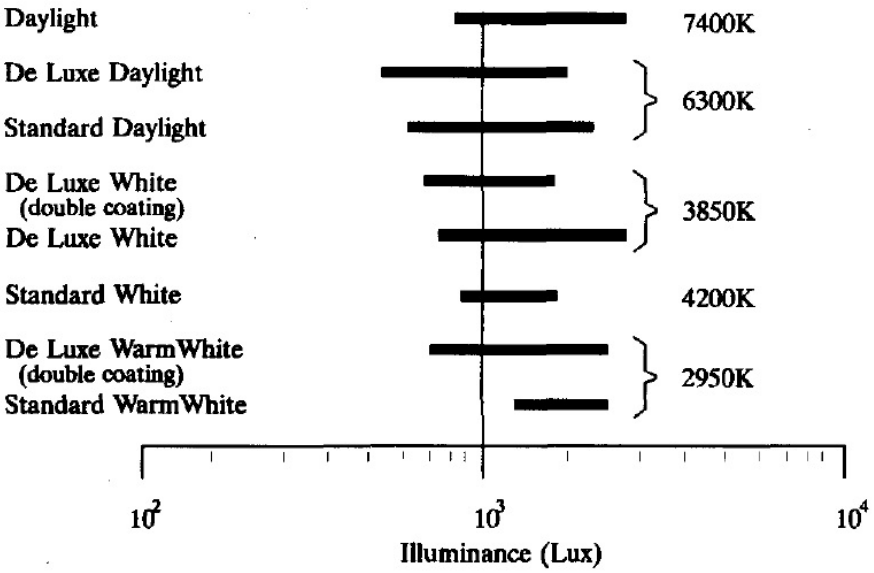


**Figure 3-4:** Preferred illuminance range versus fluorescent lamp type.

### 3.3.2 Spectral Power Distribution

Spectral power distribution (SPD) describes the power of each unit area per unit wavelength of an illumination. For the spectral power distribution of a radiant existence,

$$M(\lambda) = \frac{\partial^2 \Phi}{\partial A \partial \lambda}, \tag{3.11}$$

where $M(\lambda)$ is the spectral irradiance of the light; $\Phi$ is the radiant flux of the source; $A$ is the area over which the radiant flux is integrated; and $\lambda$ is the wavelength. Figure 3-5 to Figure 3-14 show the spectral power distribution at different color temperature.

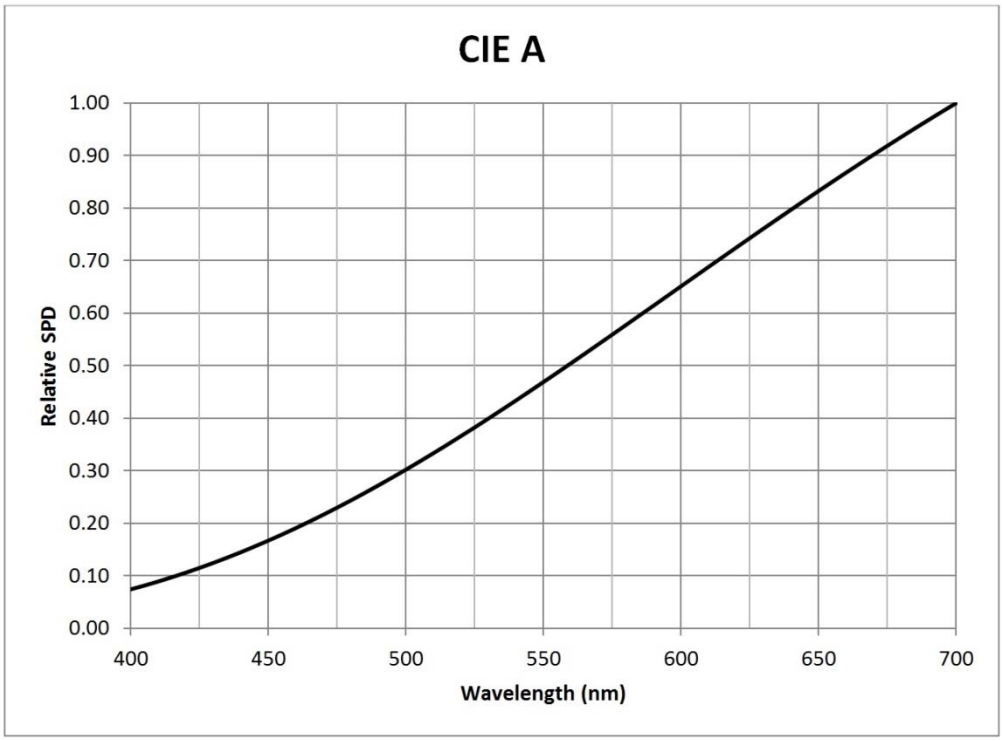


**Figure 3-5:** SPD of CIE A (incandescent, 2856K).

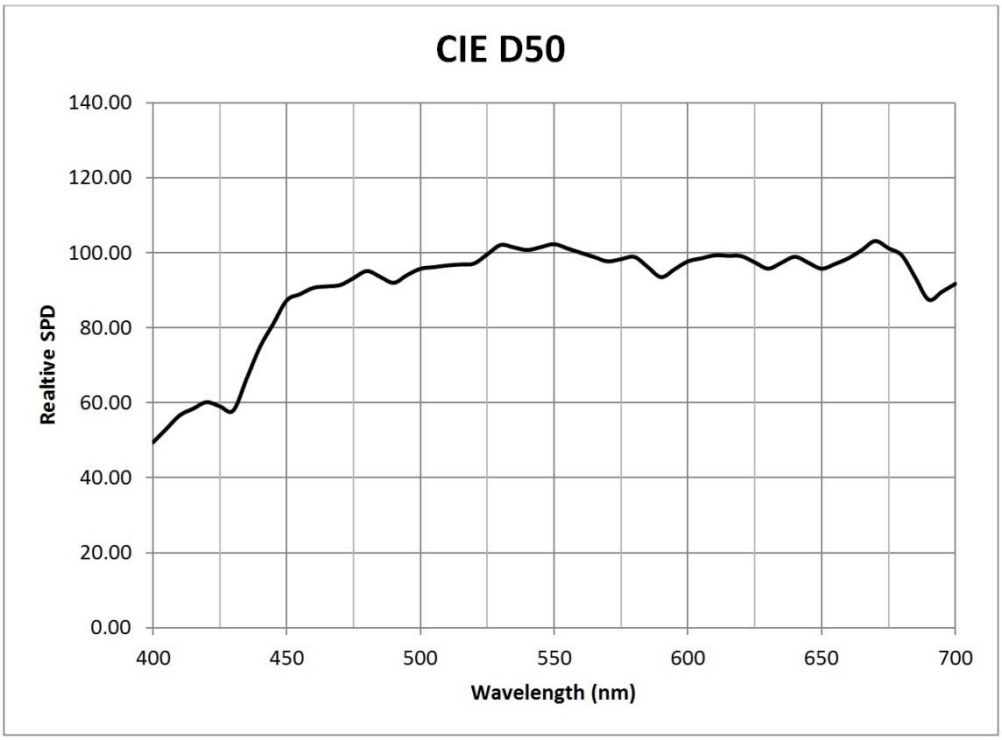


**Figure 3-6:** SPD of CIE D50 (daylight, 5000K).

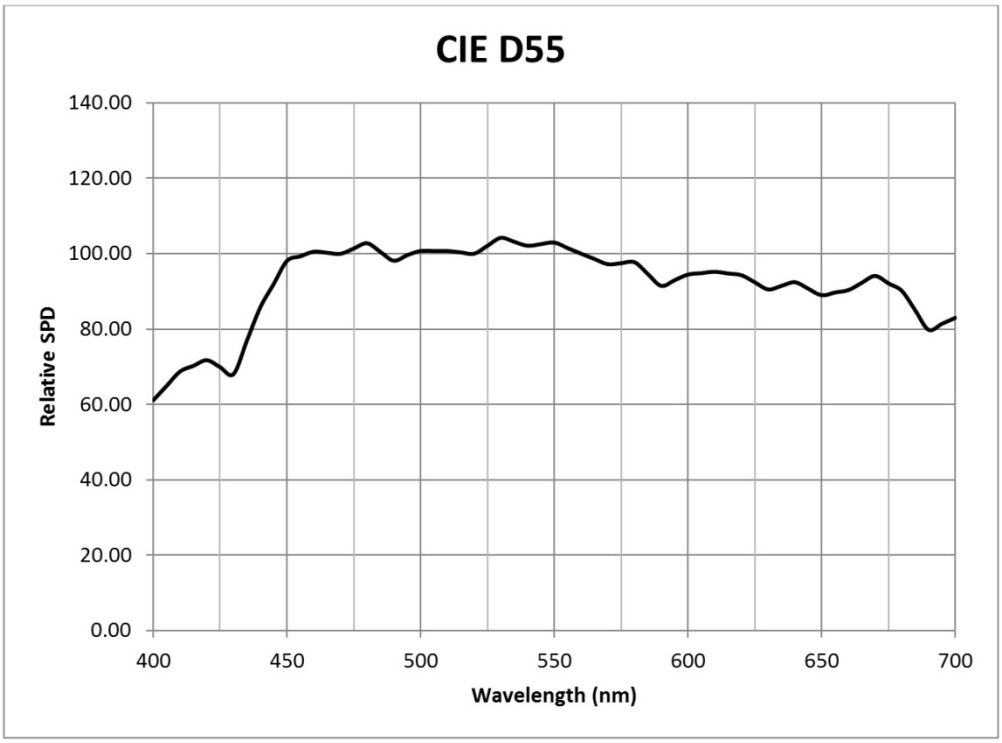


**Figure 3-7:** SPD of CIE D55 (daylight, 5500K).

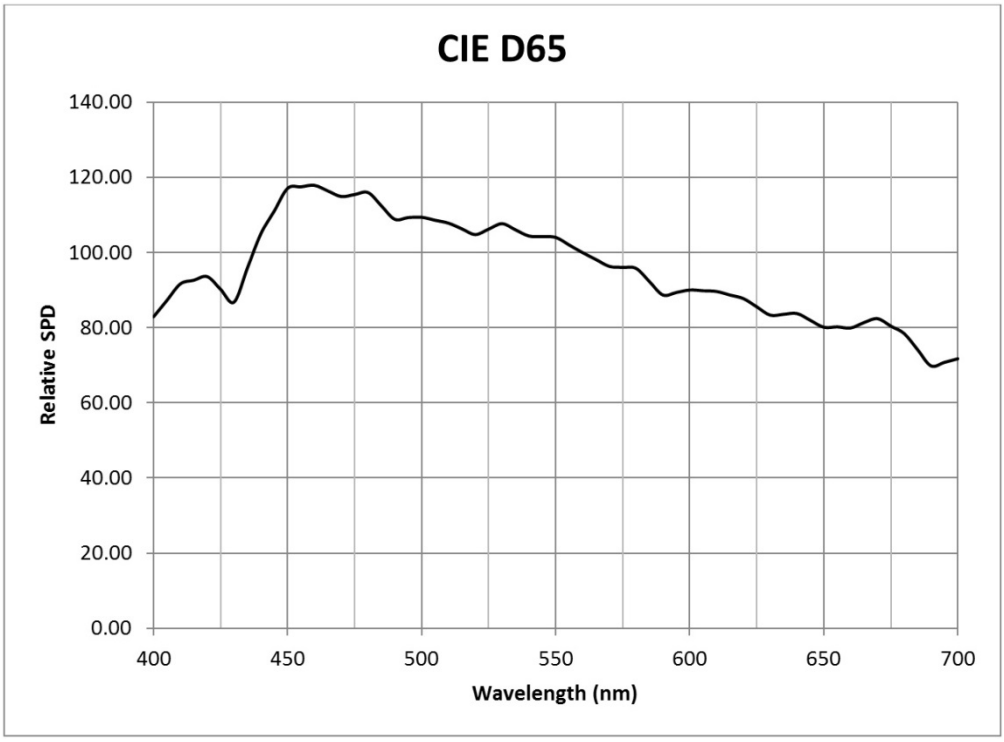


**Figure 3-8:** SPD of CIE D65 (daylight, 6500K).

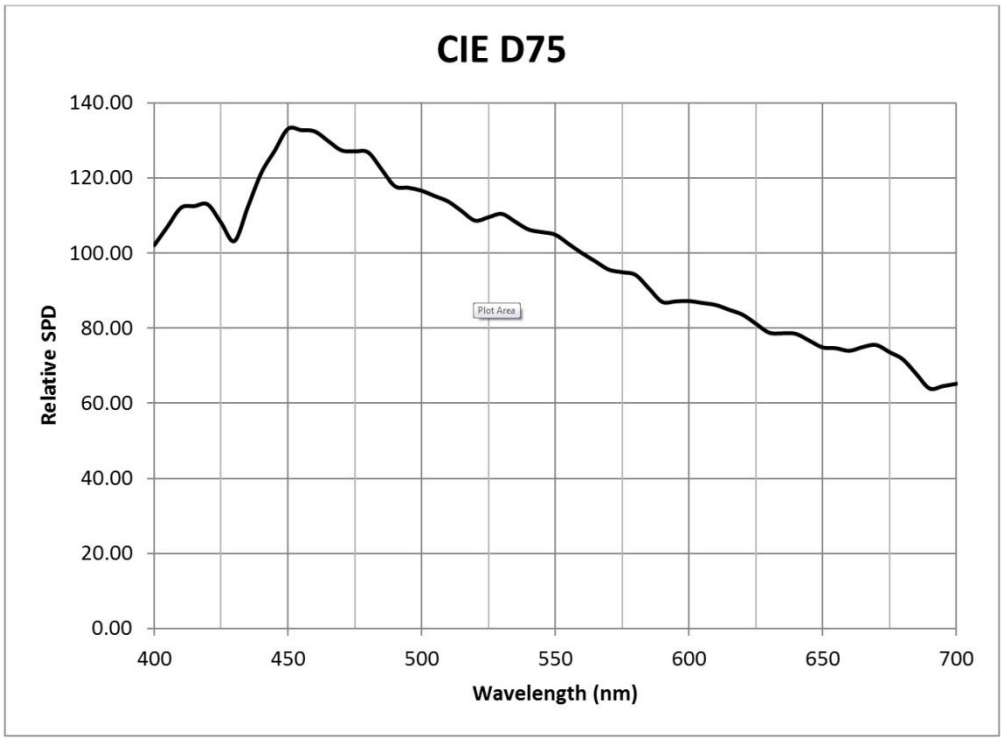


**Figure 3-9:** SPD of CIE D75 (daylight, 7500K).

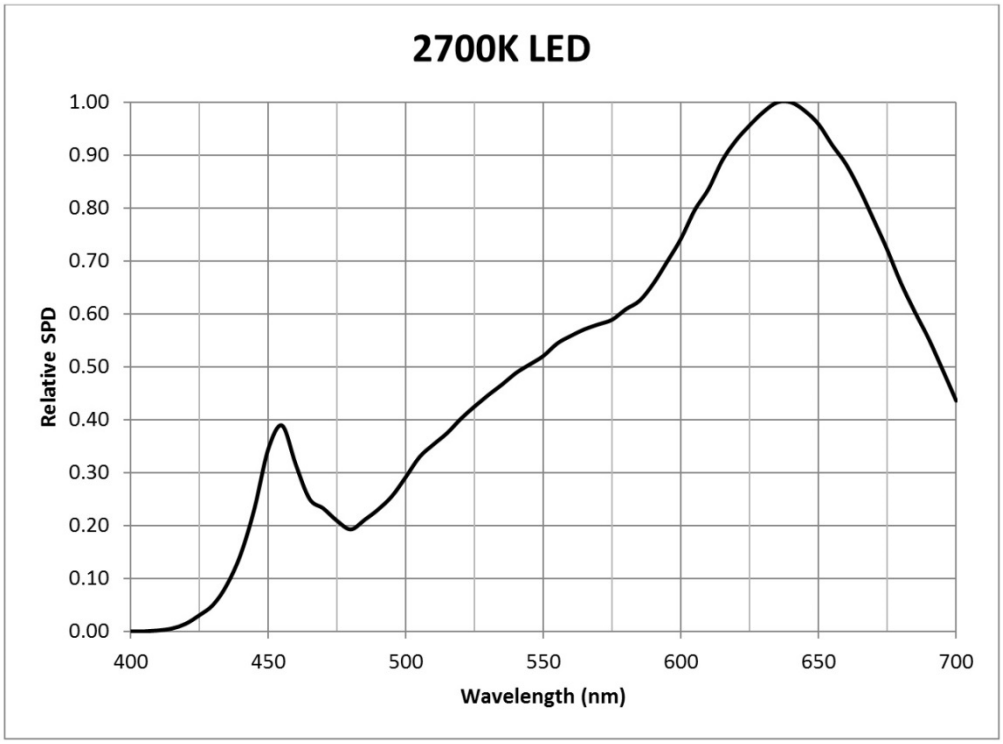


**Figure 3-10:** SPD of 2700K LED (white light LED, 2700K).

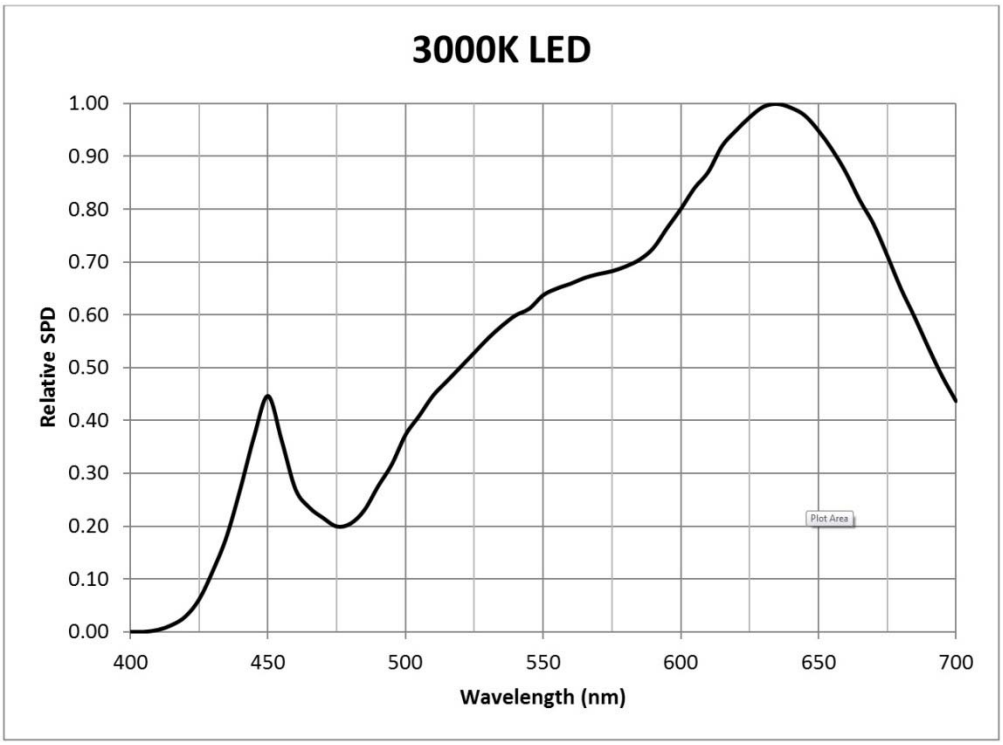


**Figure 3-11:** SPD of 3000K LED (white light LED, 3000K).

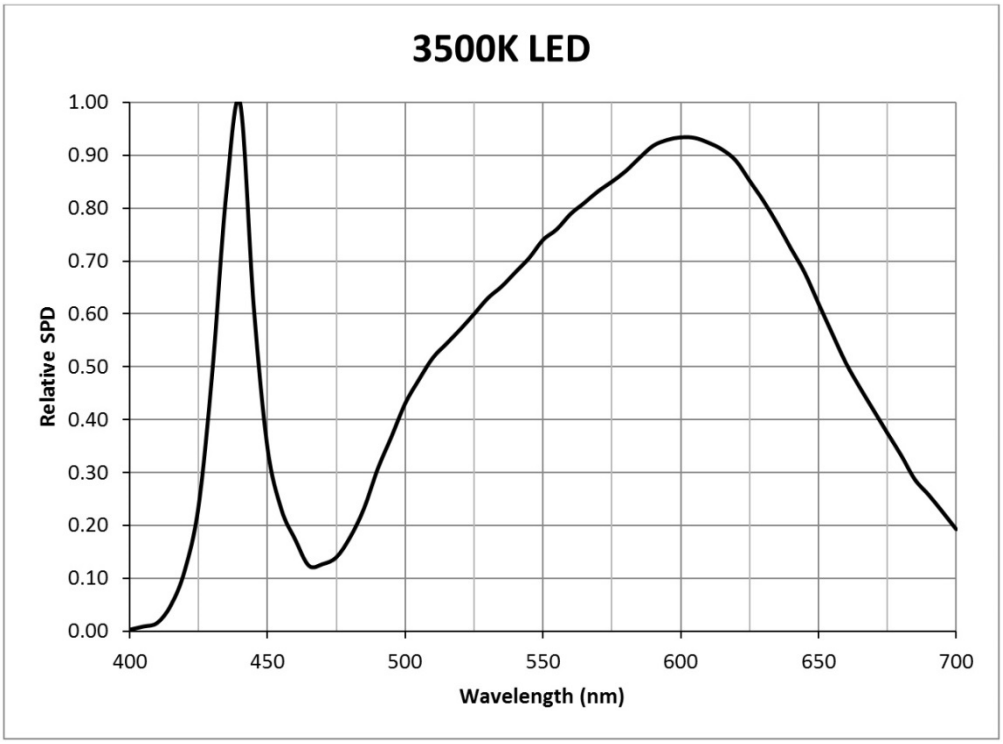


**Figure 3-12:** SPD of 3500K LED (white light LED, 3500K).

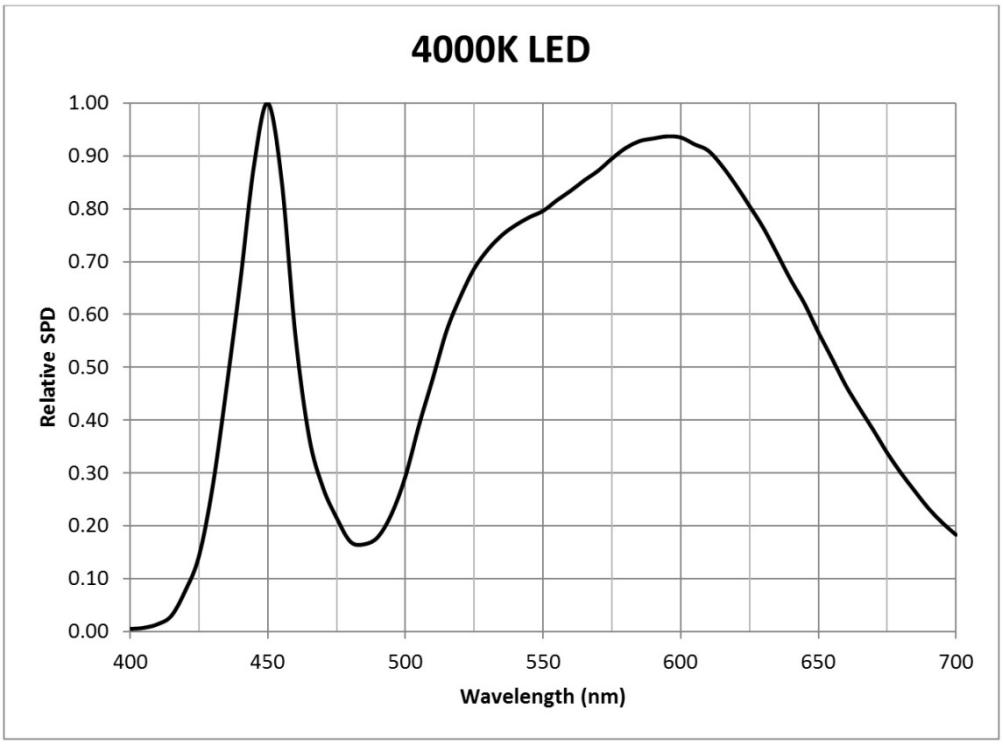


**Figure 3-13:** SPD of 4000K LED (white light LED, 4000K).

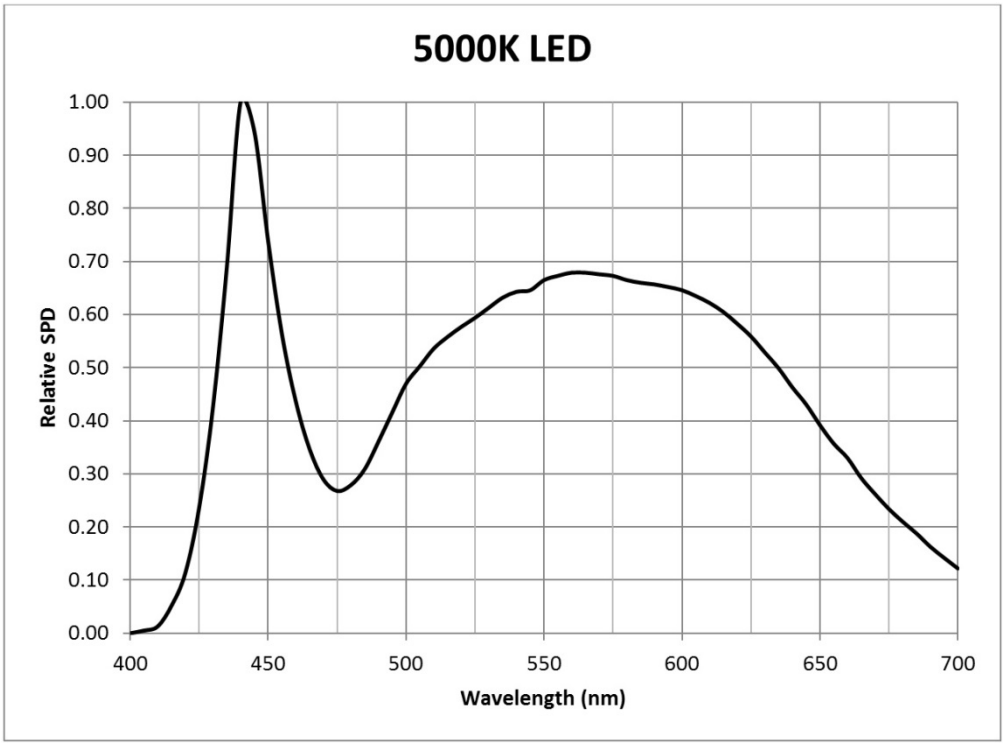


**Figure 3-14:** SPD of 5000K LED (white light LED, 5000K).

## 3.4 Color Correction Method

In this chapter, we consider to use the spectral response function of a camera maps the relative sensitivity of the camera imaging system as a function of the wavelength of light. The schematic of the proposed color correction method is shown in Figure 3-15. We use the chromatic transfer function $\tau$ for weighting the light from the water surface to a given depth of objects as

$$\tau_{\lambda}=\frac{E_{\lambda}^{surface}}{E_{\lambda}^{object}}, \tag{3.12}$$

where the transfer function $\tau$ at wavelength $\lambda$ is derived from the irradiance of the surface $E_{\lambda}^{surface}$ using the irradiance of the object $E_{\lambda}^{object}$. On the basis of the spectral response of the RGB camera, we convert the transfer function to the RGB domain:

$$\tau_{RGB}=\sum^{k}\tau_{\lambda}\cdot C_{c}(\lambda), \tag{3.13}$$

where $\tau_{RGB}$ is the weighted RGB transfer function, $Cc(\lambda)$ is the underwater spectral

characteristic function for color band $c$, $c \in \{r, g, b\}$, and $k$ is the number of discrete bands of the spectral characteristic function of the camera.

Finally, the corrected image is obtained from the weighted RGB transfer function using

$$J_\lambda(x) = k \cdot \widetilde{J}_\lambda(x) \cdot \tau_{RGB} \tag{3.14}$$

where $J_\lambda(x)$ and $\widetilde{J}_\lambda(x)$ are the color-corrected and uncorrected images, respectively. $\kappa$ is the spectral power distribution rate.

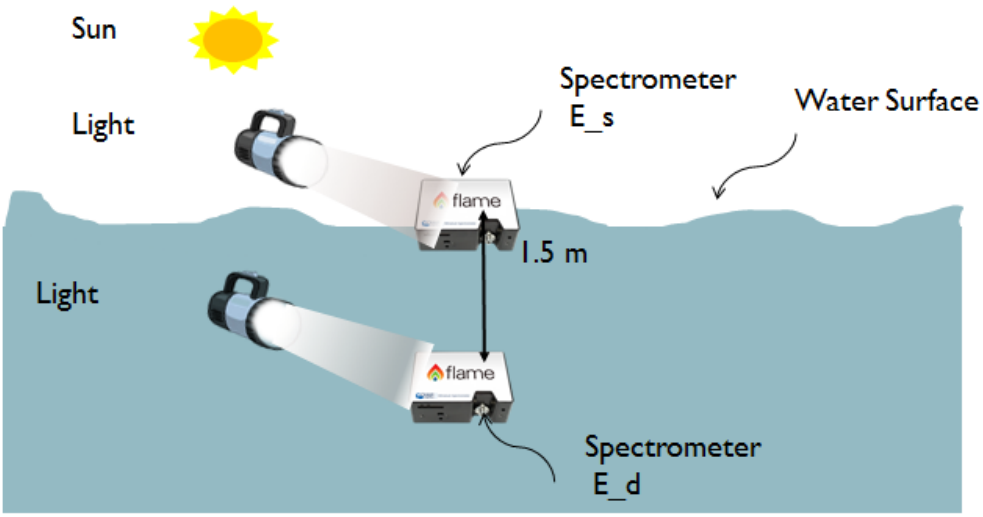


**Figure 3-15:** The schematic of the proposed color correction method

## 3.5 Experiments

In underwater environment, we use the blue-green deep-sea LED lighting; therefore, the illumination is inhomogeneous. Meanwhile, the sediments were floating in water. So, in chapter 2 we take one image pre-processing method and one de-scattering to remove the haze-like objects. However, deep-sea blue-green LED light has the limitation of wavelength, the real underwater scene cannot illuminate as well as on the land. Consequently, we need to use the camera spectral response function and illumination characteristics in water to recover the scene color. At first, we should know the illumination characteristics and camera spectral response function in Figure 3-16. In

Figure 3-16(a) the blue line shows the illumination on the water surface and the red line shows the illumination on sea bottom. Figure 3-16 (b) shows the spectral characteristic function of the Canon 70D MarkII camera. After that, we take the proposed color correction method for color correction, the results show in Figure 3-17.

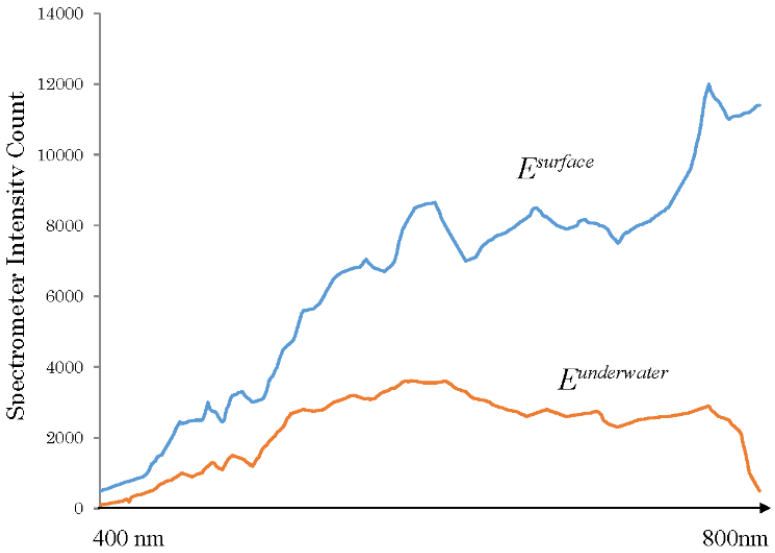


(a)

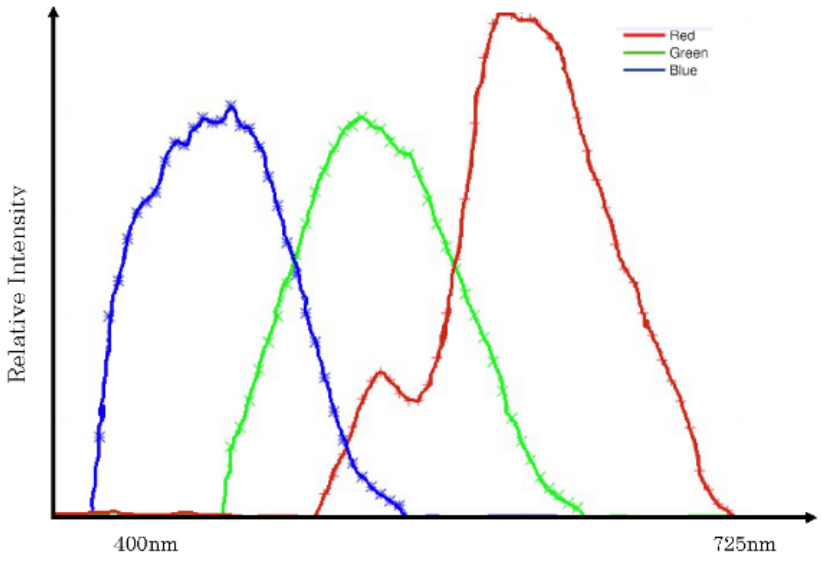


(b)

**Figure 3-16:** (a) Prediction of the illumination on the water surface and sea bottom. (b) Spectral characteristic function of the Canon 70D MarkII camera.

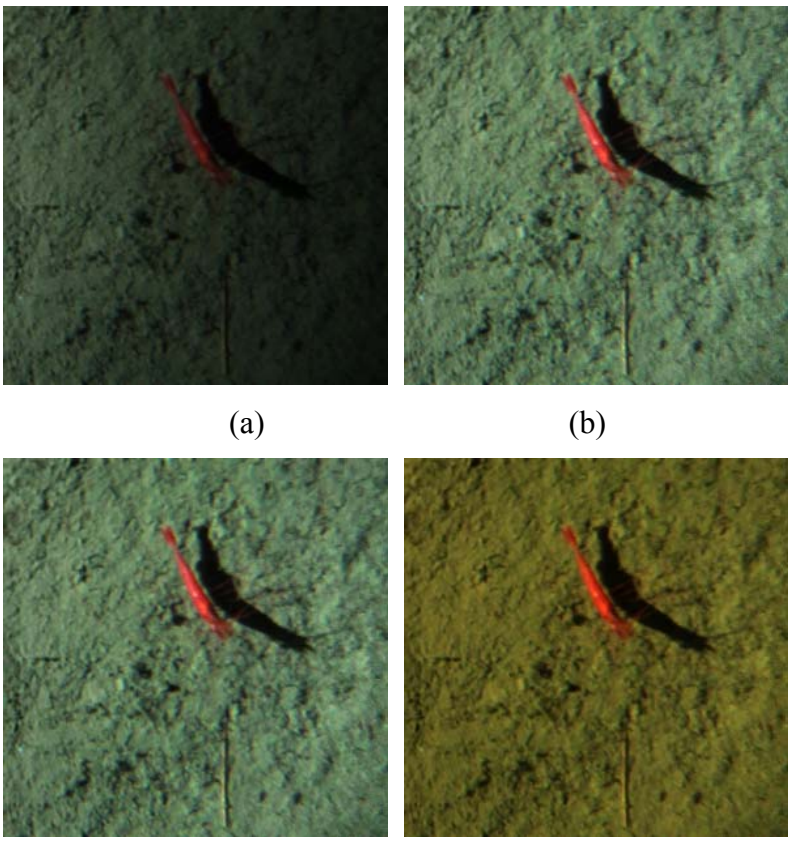

(a) (b)

(c) (d)

**Figure 3-17:** Summary of proposed approach for recovering deep-sea image. (a) Cropped initial image (1122×1106p). (b) Result after de-scattering. (c) Result after BM3D de-noising. (d) Result after color correction.

Figure 3-18 illustrates the simulation results obtained using the different methods by color chart in water tank. In this experiment, we added deep sea soil to the water in 200 mg/L. Bazeille's, Fattal's, Chiang's, and Ancuti's method show color distortion. Some scatter remained in the resulting images using the method proposed by He et al., Nicholas et al. and Xiao et al. As shown in Figure 3-18, the proposed method effectively removes haze and recovers color. We can conclude that the presently proposed method can recover the underwater scene color correctly in suitable illumination.

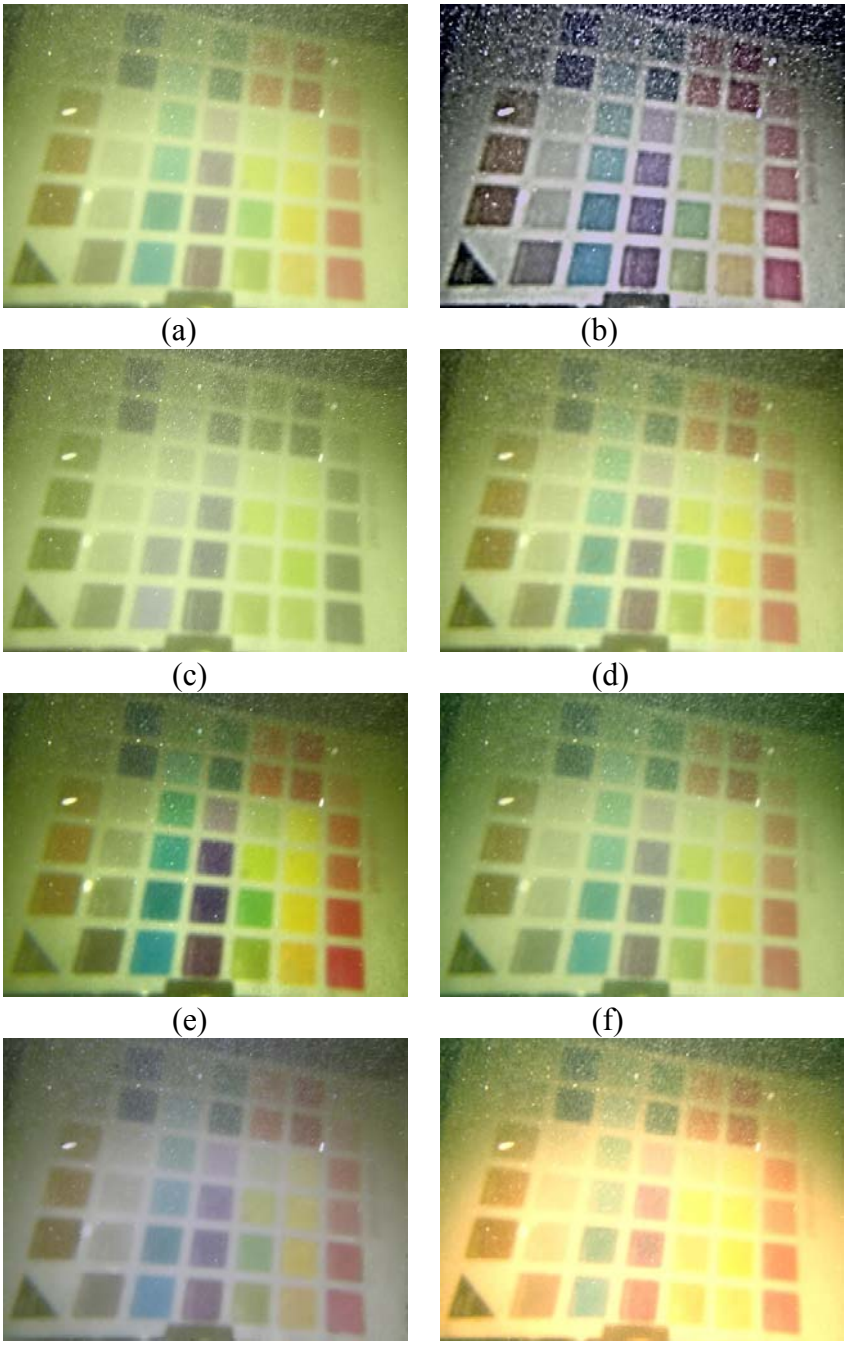

**Figure 3-18:** Simulation results of color chart in turbid water. (a) Turbidity image. (b) Bazeille's result. (c) Fattal's result. (d) Nicholas's result. (e) He's result. (f) Xiao's result. (g) Ancuti's result. (h) Chiang's result. (i) The proposed result. (j) Color chart (*Cont*)

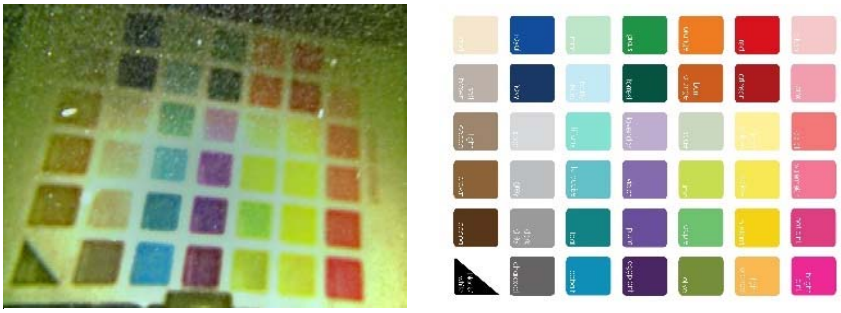

(i) (j)

**Figure 3-18**: Simulation results of color chart in turbid water. (a) Turbidity image. (b) Bazeille's result. (c) Fattal's result. (d) Nicholas's result. (e) He's result. (f) Xiao's result. (g) Ancuti's result. (h) Chiang's result. (i) The proposed result. (j) Color chart.

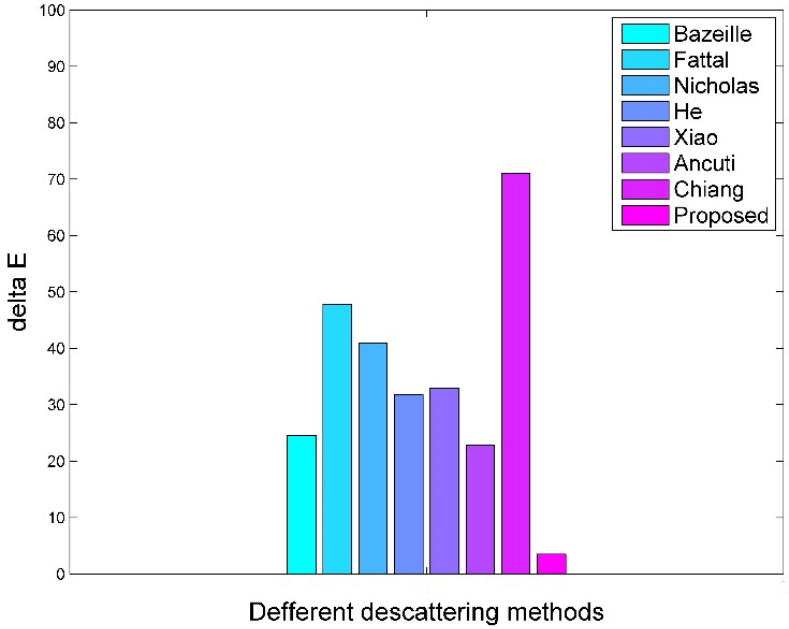


**Figure 3-19**: chromatic aberration $\Delta E$ for different methods.

We measured the color accuracy with the International Commission on illumination (CIE) standard--chromatic aberration $\Delta E$. The metric $\Delta E$ represents the difference between two colors in a *Lab* color space, calculated from their $L$, $a$, and $b$ values by the following formula:

$$\Delta E = \sqrt{(L_2 - L_1)^2 + (a_2 - a_1)^2 + (b_2 - b_1)^2}, \tag{3.15}$$

where $L$ represents the brightness, $a$ is the color from red to green, $b$ is the color from yellow to blue. The smaller of $\Delta E$ value is the more similar of two colors. In this

experiment, we cropped 42 color blocks from each image (in Figure 3-18) and then compare them. Figure 3-19 shows the average $\Delta E$ value of different methods. Obviously, the proposed method is with lowest value, so the proposed method can recover the distorted color well.

## 3.6 Conclusion

In this study, we explored and successfully implemented novel color correction method. Considering the camera spectral response color temperature and spectral power distribution, the proposed method successfully created colorful underwater images that are better than the state-of-the-art methods with lower computation time. Furthermore, the proposed method solved the limitations due to the influence of possible artificial light sources.

The experiments showed that the proposed method can recover the distorted image very well. Therefore, the proposed method is suitable for underwater imaging and solved the major problem of underwater optical imaging.

# Chapter 4

# Image Segmentation

## 4.1 Introduction

Image segmentation is the basis of image recognition and analysis. The definition is: divide image into each with distinct features of regional then extract interested objects. A lot of different segmentation methods [47-51] have been proposed such as: histogram method, morphology method, and graph cut method and so on. But all of them cannot be generalized under unique criterion.

Cluster has been applied for image segmentation. The definition of cluster is: the objects with same cluster have high similarity; however, they are very dissimilar to other objects which in other cluster [52]. There are two main clustering approaches: crisp clustering and fuzzy clustering. For crisp clustering method, the boundaries between clusters are clearly defined. However, in practice, the boundaries between clusters cannot be clearly defined. Some objects may belong to more than one cluster. In this situation, the fuzzy clustering methods provide better results [53].

The Fuzzy C-Means algorithm is the most popular fuzzy clustering method. Traditional FCM algorithm depends on the distance between objects. Standard FCM uses Euclidean distance which supposes that each feature has equal importance.

In this chapter, we proposed an image segmentation approach named automatic clustering weighted fuzzy c-means based method (ACWFCM), which uses Gradation-Gradient-two dimensional histogram automatically get the number of clustering.

## 4.2 Automatic Cluster Number Method

### 4.2.1 Gradation-Gradient 2D Histogram

Generally speaking, if the gray level of the target/ background is highly correlated, the gradient value in each target region / background region is smaller than edge. That is to say, the pixel value of target/background is close to the gradation axis (see Figure 4-1), while the edge is far away from the gradation axis. Furthermore, the edge is definitely between the background and targets or between different targets [54].

We can abandon the larger gradient value pixels, because noise usually is with large pixel value, which can filter the image.

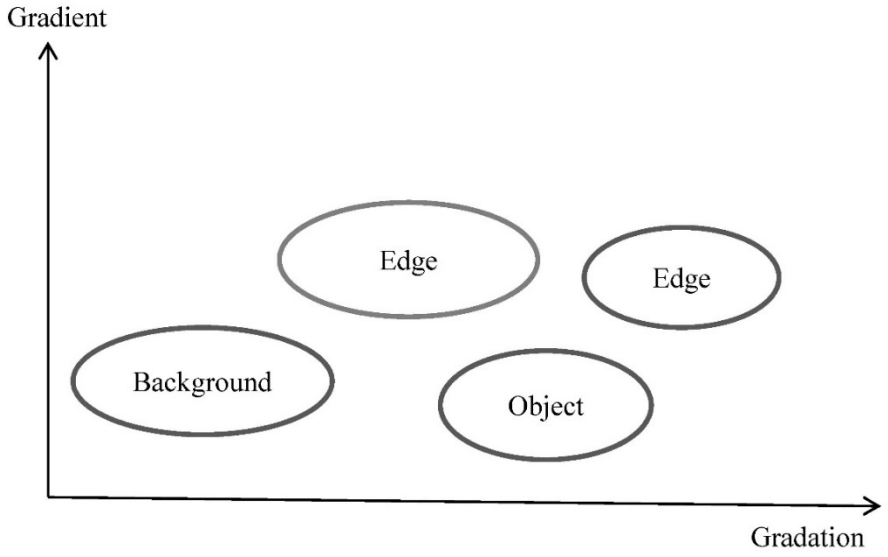


**Figure 4-1:** Gradation-Gradient two-dimensional histogram.

### 4.2.2 Automatic Cluster Number Method

For clustering algorithms, the number of clusters is often given as the initial conditions. If inappropriate number of cluster is chosen, it will make wrong cluster result and lead to a failure segmentation.

In this section, we use the Gradation-Gradient two dimensional histogram automatic obtain the number of clusters. In this histogram, according to the number of peaks to determine the number of clusters so that complete clustering unsupervised [55].

Let $f(x, y)$ is an image; the gradient value of each pixel is defined as

$$\nabla f = \left[ G_x^2 + G_y^2 \right]^{1/2} = \left[ \left( \frac{\partial f}{\partial x} \right)^2 + \left( \frac{\partial f}{\partial y} \right)^2 \right]^{1/2}. \tag{4.1}$$

And the Gradation-Gradient histogram is as follows:

$$H_{AB} = N_{AB} / N, \tag{4.2}$$

where $N$ is the all pixel number of an image, $N_{AB}$ is the numbers of pixels with gray value $A$ and gradient value $B$. Then set the gradient threshold to remove the pixel with large gradient value, next make a projection of 2D histogram to gray level and obtain 1D gradation histogram [56].

After that, Construct Gauss template $g(x)$ and make a convolution of $h(x)$ and $g(x)$.

$$\Phi(x) = h(x) * g(x) = \int_{-\infty}^{\infty} h(u) \frac{1}{\sqrt{2\pi}\sigma} \exp[-\frac{(x-u)^2}{2\sigma^2}] du, \tag{4.3}$$

where, $g(x) = \frac{1}{\sqrt{2\pi}\sigma} \exp[-\frac{(x-u)^2}{2\sigma^2}]$. The number of cluster $C$ can be automatically calculated by the aggregate $\{x_i \mid \Phi'(x_i) = 0, \Phi''(x_i) < 0\}$. The centroids $v_k$ are $\{x_i\}$.

$$C \mapsto \{x_i \mid \Phi'(x_i) = 0, \Phi''(x_i) < 0\}. \tag{4.4}$$

### 4.2.3 ACWFCM Algorithm

In this part, after automatically get the cluster number $C$, then we use an improved weighted fuzzy c-means to segment the image

The ACWFCM algorithm can be described as the following objective function:

$$\min\{J_{ACWFCM} = \sum_{(x,y),i \in N} \sum_{k=1}^{C} w_i u_k(x,y)^q \parallel I(x,y) - v_k \parallel^2\}, \tag{4.5}$$

where $u_k$ is the membership functions, $u_k(x,y)$ is the membership value at pixel location $(x, y)$ for class $k$ and $\sum_{k=1}^{C} u_k(x,y) = 1$, $I(x, y)$ is the observed image intensity

at location ($x$, $y$), and $v_k$ is the centroid of class $k$. The total number of cluster $C$ is automatically calculated by Eq. (4.4). The parameter $q$ is a weighting exponent for each fuzzy membership. It determines the amount of fuzziness of the resulting classification. For simplicity, in this paper, we assume that $q$=2 and the norm operator $\|\cdot\|$ represents the standard Euclidean distance. The main role of weighting parameter $w_i$ is adjusting the cluster centers. $w_i$ can be calculated by source image $I(x,y)$ and smooth image $\bar{I}(x,y)$. $n$ expresses the times of pixel ($x$, $y$) appeared in the image. We form a two dimensional gradation histogram by $I(x,y)$ and $\bar{I}(x,y)$. In the two dimensional gradation histogram, $H(s, t)$ represents the joint probability density, which with the gray level $s$ at source image $I(x,y)$ and with gray level $t$ at smooth image $\bar{I}(x,y)$.

$$w_i = H(s,t), \tag{4.6}$$

where, $\sum_{i=1}^{N} w_i = 1$, $N$ is the all pixel number of the image . When $w_i$=1/$N$, that is to say, the same effect to the classification of each class, ACWFCM is degenerated to the standard FCM.

The ACWFCM objective Eq. (4.4) is minimized when high membership values are assigned to pixels whose intensities are close to the centroid for its particular class, and low membership values are assigned where the pixel data is far from the centroid.

The advantage of ACWFCM is that, if a pixel is corrupted by strong noise, the segmentation will be only changed with some fractional amount. But for hard segmentations, the entire classification may be changed. At the same time, fuzzy membership functions can be used as an indicator of partial volume averaging. Furthermore, the improved algorithm not only can remove noise but also get the number of clusters more accurately; therefore it obtains a better segment result.

The steps of ACWFCM algorithm is described as follows:

**Step 1**: Provide initial values for centroids, $v_k$, $k$=1... $C$ and $C$ is automatically obtained by Eq. (4.4).

**Step 2**: Compute new memberships as follows:

$$u_k(x,y) = \frac{\| I(x,y) - v_k \|^{-2/(q-1)}}{\sum_{l=1}^{C} \| I(x,y) - v_l \|^{-2/(q-1)}}. \tag{4.7}$$

where $k$=1,...,$C$ and $q$=2.

**Step 3**: Computer new centroids as follows:

$$v_k = \frac{\sum_{x,y} w_i u_k(x,y)^2 I(x,y)}{\sum_{x,y} w_i u_k(x,y)^2}. \tag{4.8}$$

where $k$=1... $C$ and $0 < i \le N$.

**Step 4**: If the algorithm has converged, then quit. Otherwise, go to **Step 2**. In practice, the threshold value is usually set as 0.001.

### 4.2.4 Experiments and Discussions

In this experiment, we implemented the ACWFCM method on an *Intel Core2* 2.0GHz processor with MATLAB. In first experiment, The pixels of image 499×375. Figure 4-2 (b) to (d) shows the segmentation results of Otsu method, WFCM method and ACWFCM method. Compare with Otsu method and WFCM method, the proposed method can detect more blocks. But sometimes only with our eyes, we cannot decide which is better; therefore, the image segmentation assessment is introduced. In our experiment, intra-inter contrast was used [57]. The larger value is, the better quality is. The intra-inter contrast value of Otsu method is 0.5009, the intra-inter contrast value of WFCM is 0.5019, and the intra-inter contrast value of proposed method is 0.5021. Therefore, the proposed method is better than other methods.

In the second experiment, we applied the method for color images. We compared proposed method with some other methods. Figure 4-3 shows the segmentation results. From this figure, the color chart has 42 blocks. Using proposed method 22 blocks can

be segmented which is more than other methods. Therefore, the proposed method can segment better.

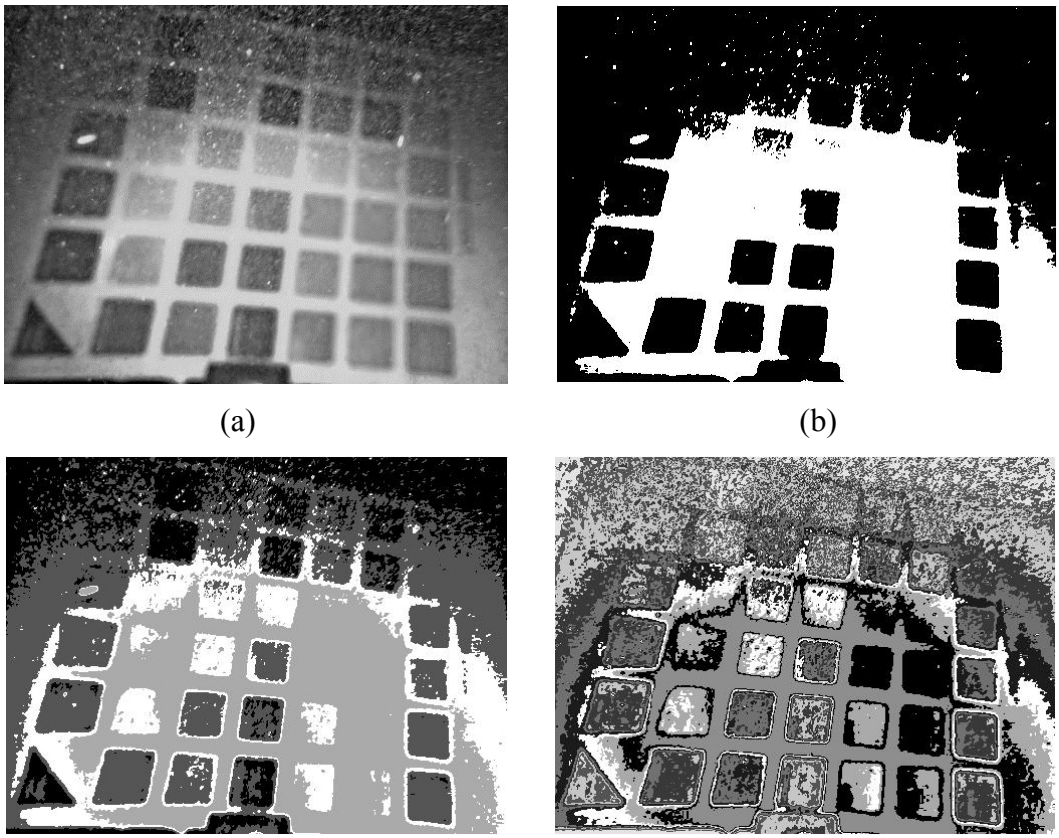

(a) (b)

(c) (d)

**Figure 4-2:** Results of different segment methods. (a)Input image.
(b) Otsu segment image. (c) WFCM segment image. (d) ACWFCM segment image

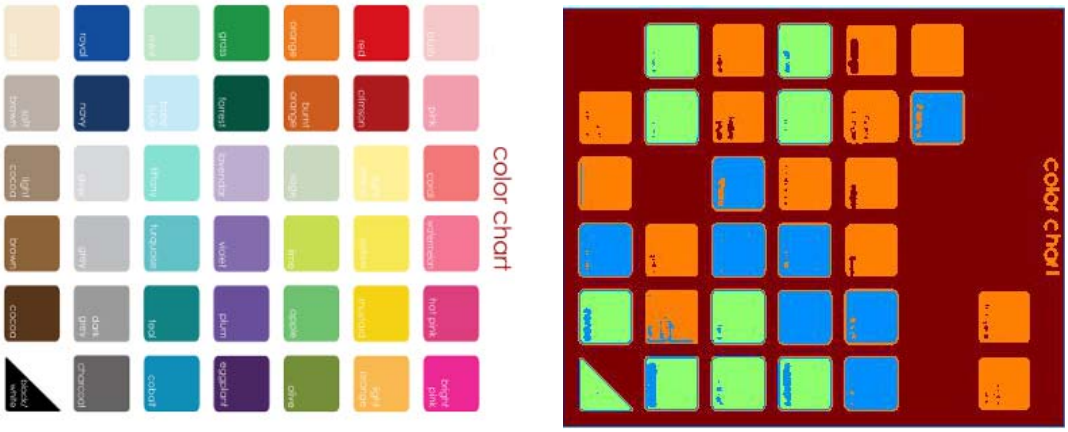


(a) (b)

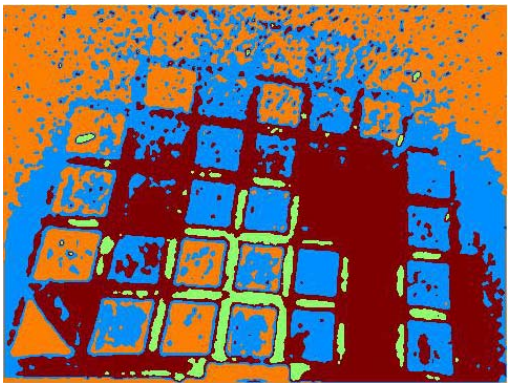

(c)

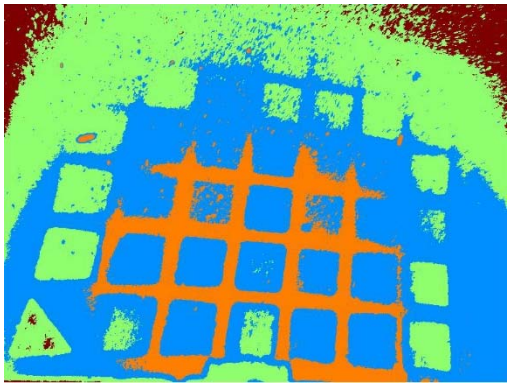

(d)

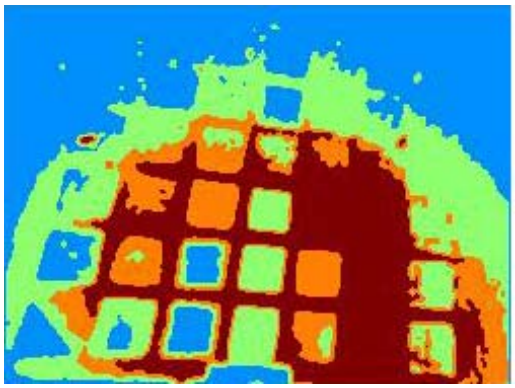

(e)

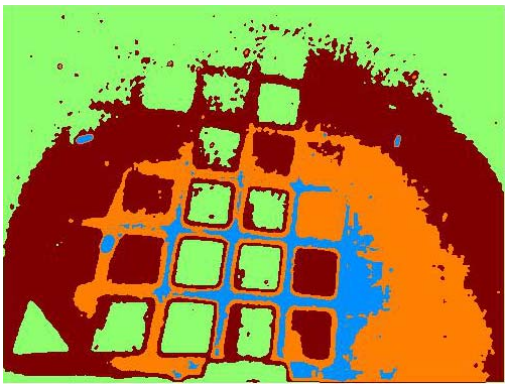

(f)

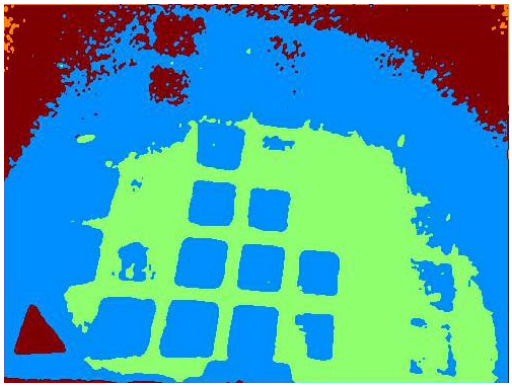

(g)

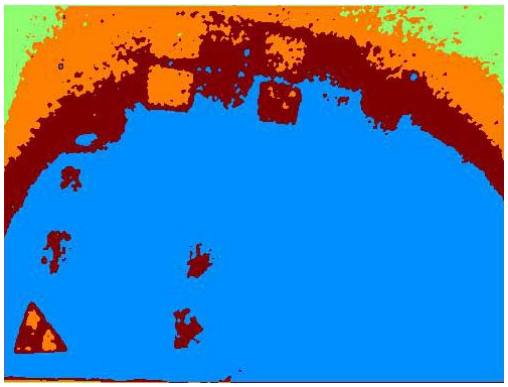

(h)

**Figure 4-3:** Simulation results of Color chart. (a) Color chart; (b) Blocks =32; (c) Bazeille's method, Blocks=22; (d) Fattal's method, Blocks=19; (e) Nicholas's method, Blocks=18; (f) He's method, Blocks=17; (g) Ancuti's method, Blocks=11; (h) Chiang's method, Blocks=3; (i) Xiao's method, Blocks=10; (j) The proposed, Blocks=22. (*Cont*)

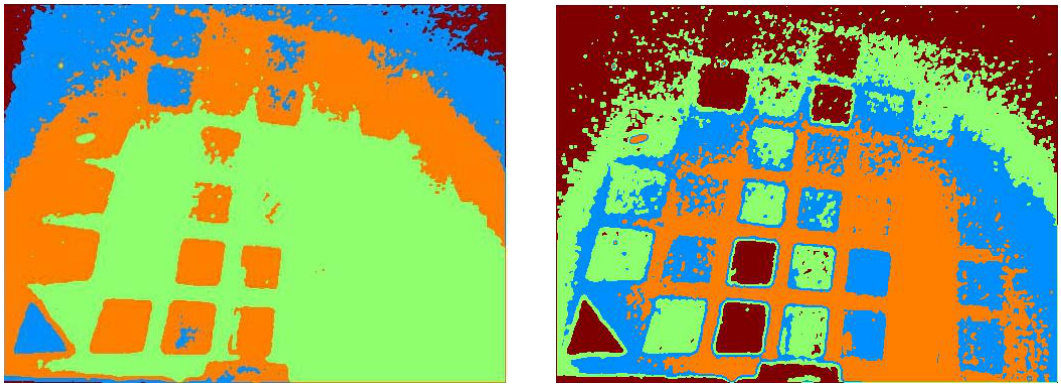

(i) (j)

**Figure 4-3:** Simulation results of Color chart. (a) Color chart; (b) Blocks =32; (c) Bazeille's method, Blocks=22; (d) Fattal's method, Blocks=19; (e) Nicholas's method, Blocks=18; (f) He's method, Blocks=17; (g) Ancuti's method, Blocks=11; (h) Chiang's method, Blocks=3; (i) Xiao's method, Blocks=10; (j) The proposed, Blocks=22.

However, there are three main drawbacks of ACWFCM. First, for using ACWFCM, it must change the RGB color image to other domain, such as gray image, HSV. The second is that it is time consuming. In our experiment, Otsu cost about 1 min, FCM cost about 2 hours, and ACWFCM cost about 1.1 hours. The third is it only can process images with simple texture. If the input image is with the complex textures, using ACWFCM method, the result is over-segmentation.

## 4.3 Fast Active Contour model based Method

All things tend to exist on minimum energy, because at this time it is the most balanced state. Therefore, many image segmentation methods have been developed on the basis of minimum energy. The active contour models (ACM) [58] are based on the theory of surface evolution and geometric flows. It has been extensively studied and successfully utilized for image segmentation in recent years.

The basic idea of ACM is as follows: express the target edge with continuous curve, and then define an energy function so that its arguments include edge. Therefore, the segmentation process is transformed to solving the process of minimum energy function. when the curve on the edge, the energy is minimum. Generally speaking, the ACM can be categorized into two classes: one is edge-based models [59, 60] and the

other is region-based models [61, 62]. Edge-based models use an edge stopping function and a balloon force function to control the motion of the contour. But, during some researches, appropriate choice of balloon force is difficult to set. If the balloon force is not appropriate, there will be a bad segment result. On the other hand, region-based active contour models have two advantages. First, do not use the image gradient and therefore have a better performance for weak boundaries images. Second, Insensitive to the location of initial contours. One of the most popular region-based active contour models is Chan-Vese model [63]. The Chan-Vese model is based on Mumford-Shah [64] segmentation techniques. In 2002, Vese and Chan extended their work by using a multiphase level set framework scheme for piecewise constant (PC) [65] and piecewise smooth (PS) [66] optimal approximations. It has some advantages. Such as the phases cannot overlap and minimizes as much as possible the computational cost, reducing the number of level set functions. These models effectively solve the fuzzy boundaries image and detect interior contours in images. But, the main drawback of them is the additional computational complexity. Li et al. [67] proposed the local binary fitting (LBF) model by embedding the local information. LBF can segment images with intensity in homogeneities and is more efficient and accurate than the PS model. However, the computational complexity is remains high. So, the main motivation of this chapter is improving the computational complexity of segmentation.

In this chapter, we propose a novel ACM model named fast active contour model (FACM) to improve the traditional level set methods by avoiding the calculation of signed distance function (SDF) and speed up the computational complexity of re-initialization. In the FACM, in order to speed up the computational complexity, we also provide a fast semi-implicit additive operator splitting (AOS) algorithm [68]. Furthermore, the proposed FACM also has property of selective local or global segmentation in experiments.

Curve evolution based methods are often utilized for image segmentation. In these methods, partial differential equations are frequently used to evolve the curves. The equations are formed following a certain physical principle. And use the curve evolution problem as an energy minimization problem to seek the solution of the corresponding Euler-Lagrange equation. In either case, partial differential equations are solved in an

iterative manner to evolve the curve. Typically, the curve evolution based methods are divided into two categories: one is region based methods and the other is edge based methods. In this section, we just review most epidemic models.

### 4.3.1 Mumford and shah model

The Mumford and shah (MS) model [64] is defined as following: assume the segmented image as piecewise constant, find an optimal piecewise smooth approximation function $u$ of image $u_0$, which varies smoothly within each sub-region $\Omega_i$ of image domain $\Omega \subset R^2$, while rapidly or discontinuously goes across the boundaries of $\Omega_i$. The MS energy functional is given as following.

$$E^{MS}(u,C) = \int_{\Omega}(u-u_0)^2\,dx + \mu\int_{\Omega/C}|\nabla u|^2\,dx + v\,|C|\,. \tag{4.9}$$

where $|C|$ is the length of the contour $C$, $\mu, v \geq 0$ are fixed parameters.

For many applications, it is enough to assume that $u$ is a piecewise constant function. In these cases, the second term disappears from the above minimization function. Among the ways of representing the unknown interfaces, the level set method is the most elegant because of its ability to deal with unknown topology. The main drawback is expensive computation.

### 4.3.2 Snakes model

A snake is a continuous curve that forms an initial state. It tries to position itself dynamically on image features. It is deformed as a result of the influence of local forces derived from edge points, while this deformation remains smooth because of the effect of internal forces [58]. The energy of the snake is typically given as following.

$$E^{snake} = \int_0^1 E_{\text{int}}[C(s)] + E_{image}[C(s)] + E_{ext}[C(s)]ds\,, \tag{4.10}$$

where $C(s)$ is the evolving curve parameterized by $s$, and $s$ is the curve arc-length. The first term of right hand side of this equation penalizes stretching and bending of the

curve. The second term attracts the evolving curve towards image features such as bright or dark line, edges et al.

The snake model has two main drawbacks. One is that it is highly sensitive to the parameterization of the curve. The other is the explicit representation of the curves prohibits any topological changes during evolution.

### 4.3.3 Level set methods

Level set methods (LSM) [69] evolve the curve $C$ along the normal direction. Different to the others, the level set methods embed the curve into a higher dimensional function $\phi$ called a level set function,

$$C = \{s \in \Omega \,|\, \phi(s) = 0\}, \tag{4.11}$$

where, Ω is image domain. Noting that the curve $C$ is always given by$\varphi(C(t), t) = 0$, and then by taking the total derivative of the left hand side of this equation we can get

$$\frac{\partial \phi}{\partial t} = -V\,|\nabla \phi|, \tag{4.12}$$

where $V$ is a speed function. The speed function $V$ is used to define the energy minimization problem. The level set evolution problem can also be solved as energy minimization problem [68]. Let us define energy functional as

$$E^{LSM}(\phi) = \int_{\Omega} e(s, \phi, \phi_s)\, ds, \tag{4.13}$$

where $\phi_s$is the derivative of $\phi$ with respect to $s$. Then, use the Euler-Lagrange, we get

$$\frac{\partial E}{\partial \phi} = \frac{\partial e}{\partial \phi} - \frac{\partial}{\partial s}\frac{\partial e}{\partial \phi_s} = 0, \tag{4.14}$$

Then we can formulate the level set function by Eq. (4.12), as

$$\frac{\partial \phi}{\partial t} = -\frac{\partial E}{\partial \phi} = -\frac{\partial e}{\partial \phi} + \frac{\partial}{\partial s}\frac{\partial e}{\partial \phi_s} \quad , \tag{4.15}$$

where $e$ is used to define the energy minimization problem. One drawback of the level set method is its high computational expense because it expands the domain of computation from the interface to a grid in one higher dimension.

### 4.3.4 Geodesic active contours

Geodesic active contours (GAC) [59] are an extension of the classical snakes described above. The GAC energy functional can be given by,

$$E^{GAC}(C) = \int g(|\nabla u_0(C(s))|)|C'(s)ds \, , \tag{4.16}$$

where $u_0$ is the image, $g$ is a strictly decreasing function such that $g(w) \to 0$ as $w \to \infty$. The curve evolution equation is obtained via Euler-Lagrange formulation as

$$\frac{\partial \phi}{\partial t} = g(|\nabla u_0|)|\nabla \phi|\kappa - \nabla g(|\nabla u_0|)\cdot \nabla \phi \, , \tag{4.17}$$

where the curvature $\kappa$ is now computed on the level sets of $\phi$, referred to as the mean curvature. The GAC model only considers the local information. Moreover, it needs to be initialized in a way that is either completely outside or inside the actual boundary.

### 4.3.5 Active contours without edges

Chan and Vese proposed a method (CV) [63] based on the Mumford-Shah model and the level set method. Set an image $u_0(x,y)$. Let us give the curve $C = \partial w$, with $w \subset \Omega$ an open subset and two unknown constants $c_1$ and $c_2$. Denoting $\Omega_1 = w, \Omega_2 = \Omega \setminus w$, the energy function is (see also [67]).

$$E^{CV}(c_1,c_2,C) = \mu \cdot Length(C) + \nu \cdot Area(inside(C)) + \lambda_1 \int_{\Omega_1 = w} |u_0 - c_1|^2 \, dxdy + \lambda_2 \int_{\Omega_2 = \Omega \setminus w} |u_0 - c_2|^2 \, dxdy. \tag{4.18}$$

where $\mu \geq 0, \nu \geq 0, \lambda_1, \lambda_2 > 0$ are fixed parameters. In almost calculations, we fix $\lambda_1 = \lambda_2 = 1$ and $\nu = 0$. If and only if the curve *C* on the boundary of homogeneity area, the above function obtain minimum value. Set $\phi$ as the level set function. Then, the energy $E^{CV}(c_1,c_2,\phi)$ can be written as

$$E^{CV}(c_1,c_2,\varphi) = \mu \int_\Omega \delta(\varphi) |\nabla \varphi| dxdy + \nu \int_\Omega H(\varphi) dxdy + \lambda_1 \int_\Omega |u_0 - c_1|^2 H(\varphi) dxdy + \lambda_2 \int_\Omega |u_0 - c_2|^2 (1 - H(\varphi)) dxdy. \tag{4.19}$$

Keeping $\phi$ fixed and minimizing the energy $E^{CV}(c_1,c_2,\phi)$ with respect to the constants $c_1$ and $c_2$, we can get the following formulas with $C = \{(x,y) \mid \phi(x,y) = 0\}$

$$c_1 = \frac{\int_\Omega u_0(x,y) H(\phi(x,y)) dxdy}{\int_\Omega H(\phi(x,y)) dxdy},$$

$$c_2 = \frac{\int_\Omega u_0(x,y)(1 - H(\phi(x,y))) dxdy}{\int_\Omega (1 - H(\phi(x,y))) dxdy},$$

$$\frac{\partial \phi}{\partial t} = \delta(\phi)\left[\mu \nabla\left(\frac{\nabla \phi}{|\nabla \phi|}\right) - \nu - \lambda_1 (u_0 - c_1)^2 + \lambda_2 (u_0 - c_2)^2\right]. \tag{4.20}$$

where, Heaviside function $H(z) = \begin{cases} 1 & z \geq 0 \\ 0 & z < 0 \end{cases}$. $\delta_\varepsilon(z) = \frac{dH(z)}{dz}$ is Dirac function. In practice, $H_\varepsilon(z) = \frac{1}{2}(1 + \frac{2}{\pi}\arctan(\frac{z}{\varepsilon}))$ and $\delta_\varepsilon(z) = \frac{1}{\pi} \cdot \frac{\varepsilon}{\varepsilon^2 + z^2}$, where $\varepsilon$ is constant [70].

### 4.3.6 Geodesic active regions

The geodesic active regions (GAR) model [71] utilizes boundary and region based information to find a set of minimal length curves. The GAR energy function is

$$E^{GAR}(C) = \alpha \sum_{i=1}^{2} \iint_{R_i} -\log[P_X(u(x,y)) \mid R_i]dxdy + (1-\alpha)\sum_{i=1}^{2} \int_0^1 g[P_C(C_i \mid R_i), \sigma_C] \mid C'(s) \mid ds. \tag{4.21}$$

where $\alpha$ is a positive constant that balance the contributions of the two terms, $0 \leqq \alpha \leqq 1$. $g$ is a Gaussian function with zero mean and variance $\sigma^2$. The first term on the right hand side is region based and represents the negative log-likelihood of a pixel belonging to a particular region. $u$ is the image, and boundary probabilities $P_C(\cdot)$ are used. $P_X(\cdot)$ is the conditional intensity density function with respect to the hypothesis $R_1$and $R_2$. The level set update equation can be given as follows,

$$\frac{\partial \varphi_1}{\partial t} = -\alpha \log\left(\frac{P_X(u \mid R_1)}{P_X(u \mid R_2)}\right) \mid \nabla \varphi_1 \mid + (1-\alpha)\left(g[P_C(\cdot), \sigma_C]\kappa_1 \mid \nabla \varphi_1 \mid + \nabla g[P_C(\cdot), \sigma_C] \cdot \nabla \varphi_1\right). \tag{4.22}$$

This model overcomes many drawbacks of the other models. However, the Gaussian function used to describe intensities may be inadequate in many cases.

### 4.3.7 Piecewise constant model

Chan and Vese improved the multi-phase piecewise constant (PC) active contour model [65] without edges in image processing. Let us write the energy for $n$=4 phases or classes, that is to say, use $m$=2 level set functions ($n$=2$^m$). Set level set functions $\phi_i (1 \le i \le m)$ to implicit express the curves $C_i$. Then, we get the energy function,

$$
\begin{aligned}
E^{PC}{}_4(c,\Phi) = & \int_\Omega (u_0 - c_{11})^2 H(\varphi_1)H(\varphi_2)dxdy \\
& + \int_\Omega (u_0 - c_{10})^2 H(\varphi_1)(1 - H(\varphi_2))dxdy \\
& + \int_\Omega (u_0 - c_{01})^2 (1 - H(\varphi_1))H(\varphi_2)dxdy \\
& + \int_\Omega (u_0 - c_{00})^2 (1 - H(\varphi_1))(1 - H(\varphi_2))dxdy \\
& + \nu \int_\Omega |\nabla H(\varphi_1)| + \nu \int_\Omega |\nabla H(\varphi_2)|,
\end{aligned} \tag{4.23}
$$

where $c = (c_{11}, c_{10}, c_{01}, c_{00})$ is a constant vetor, and $\Phi = (\phi_1, \phi_2)$. And then minimizing the energy functional $E^{PC}{}_4(c, \Phi)$ with respect to $\phi_i$, we derive the gradient descent flow,

$$
\begin{aligned}
& \frac{\partial \phi_1}{\partial t} = \delta_\varepsilon(\phi_1)\{\nu div\left(\frac{\nabla \phi_1}{|\phi_1|}\right) - \\
& \left[\left((u_0 - c_{11})^2 - (u_0 - c_{01})^2\right)H(\phi_2) + \left((u_0 - c_{10})^2 - (u_0 - c_{00})^2\right)(1 - H(\phi_2))\right]\}
\end{aligned} \tag{4.24}
$$

$$
\begin{aligned}
& \frac{\partial \phi_2}{\partial t} = \delta_\varepsilon(\phi_2)\{\nu div\left(\frac{\nabla \phi_2}{|\phi_2|}\right) - \\
& \left[\left((u_0 - c_{11})^2 - (u_0 - c_{10})^2\right)H(\phi_1) + \left((u_0 - c_{01})^2 - (u_0 - c_{00})^2\right)(1 - H(\phi_1))\right]\}
\end{aligned} \tag{4.25}
$$

where, the constants functions $c_{11}$, $c_{10}$, $c_{01}$, $c_{00}$ respectively as

$$
c_{11}(\Phi) = \frac{\int_\Omega u_0 H_\varepsilon(\phi_1)H_\varepsilon(\phi_2)dxdy}{\int_\Omega H_\varepsilon(\phi_1)H_\varepsilon(\phi_2)dxdy} \qquad c_{10}(\Phi) = \frac{\int_\Omega u_0 H_\varepsilon(\phi_1)(1 - H_\varepsilon(\phi_2))dxdy}{\int_\Omega H_\varepsilon(\phi_1)(1 - H_\varepsilon(\phi_2))dxdy}
$$

$$
c_{01}(\Phi) = \frac{\int_\Omega u_0 (1 - H_\varepsilon(\phi_1))H_\varepsilon(\phi_2)dxdy}{\int_\Omega (1 - H_\varepsilon(\phi_1))H_\varepsilon(\phi_2)dxdy} \qquad c_{00}(\Phi) = \frac{\int_\Omega u_0 (1 - H_\varepsilon(\phi_1))(1 - H_\varepsilon(\phi_2))dxdy}{\int_\Omega (1 - H_\varepsilon(\phi_1))(1 - H_\varepsilon(\phi_2))dxdy}
$$

where, Heaviside function $H(z) = \begin{cases} 1 & z \geq 0 \\ 0 & z < 0 \end{cases}$. $\delta_\varepsilon(z) = \frac{dH(z)}{dz}$ is Dirac measurement $(\delta_\varepsilon(x) = H'_\varepsilon(x))$. In practice, $\lambda_1$=$\lambda_2$=1.

### 4.3.8 Piecewise smooth model

In order to overcome the general problem of MS model in image processing, Chan and Vese proposed piecewise smooth (PS) model [66] which aims at expressing the

intensities inside and outside the contour as piecewise smooth functions instead of constants. Assume that $u^+$, $u^-$, are curve $C$ functions on $\phi \geqq 0$ and on $\phi \leqq 0$ respectively. The unknowns' $u$ and $\phi$ can be expressed by introducing two functions $u^+$ and $u^-$ as,

$$u(x,y) = \begin{cases} u^+(x,y) & if\ \phi(x,y) \geq 0 \\ u^-(x,y) & if\ \phi(x,y) < 0 \end{cases}. \tag{4.26}$$

Then, the 2-Dimensional PS model energy function was defined,

$$\begin{aligned} E^{PS}(u^+,u^-,\varphi) = & \int_\Omega |u^+ - u_0|^2\ H(\varphi)dxdy \\ & + \int_\Omega |u^- - u_0|^2\ (1-H(\varphi))dxdy \\ & + \mu\int_\Omega |\nabla u^+|^2\ H(\varphi)dxdy \\ & + \mu\int_\Omega |\nabla u^-|^2\ (1-H(\varphi))dxdy + \nu\int_\Omega |\nabla H(\varphi)|, \end{aligned} \tag{4.27}$$

where $v$, $\mu \geqq 0$ are fixed parameters. $u_0$ is the original image. Minimizing the above equation, we get the following Euler-Lagrange equations

$$\begin{aligned} & u^+ - u_0 = \mu\Delta u^+\ in\ \{(x,y) : \phi(t,x,y) > 0\} \\ & \frac{\partial u^+}{\partial \vec{n}} = 0\ on\ \{(x,y) : \phi(t,x,y) = 0\} \cup \partial\Omega \\ & u^- - u_0 = \mu\Delta u^-\ in\ \{(x,y) : \phi(t,x,y) < 0\} \\ & \frac{\partial u^-}{\partial \vec{n}} = 0\ on\ \{(x,y) : \phi(t,x,y) = 0\} \cup \partial\Omega \end{aligned}$$

$$\begin{aligned} & \frac{\partial \phi}{\partial t} = \delta_\varepsilon(\phi)[\nu\nabla\left(\frac{\nabla\phi}{|\nabla\phi|}\right) - |u^+ - u_0|^2 \\ & - \mu|\nabla u^+|^2 + |u^- - u_0|^2 + \mu|\nabla u^-|^2] \end{aligned} \tag{4.28}$$

where $\partial / \partial \vec{n}$ denotes the partial derivative in the normal direction $\acute{n}$ at the corresponding boundary. $\delta_\varepsilon(z) = \frac{dH(z)}{dz}$ is Dirac measurement $(\delta_\varepsilon(x) = H'_\varepsilon(x))$.

We can see that the computational cost is very expensive. Furthermore, the $u^+$ and $u^-$

must be extended to the whole image domain, which is difficult to implement and also increases the computational cost.

### 4.3.9 The Proposed Model

In this section, a new level set model is proposed for image segmentation which named Fast Active Contour Model (FACM). From the Eq. (4.20), we can find that the main force of level set evolution is depended on $-\lambda_1(u_0-c_1)^2+\lambda_2(u_0-c_2)^2$. As we set $\lambda_1=\lambda_2=1$, decompose it by squared difference formula, we can get $2(c_1-c_2)(u_0-\frac{c_1+c_2}{2})$. Then, we propose the following model,

$$\frac{\partial\phi}{\partial t}=\alpha\delta_\varepsilon(\phi)\left(\mu\nabla\left(\frac{\nabla\phi}{|\nabla\phi|}\right)+u_0-\frac{c_1+c_2}{2}\right), \tag{4.29}$$

where, $u_0-\frac{c_1+c_2}{2}$ is the speed term. $\nabla$ is the gradient operator. $\alpha$ is added to increase the propagation speed. $\mu\geqq 0$ is a fixed parameter.

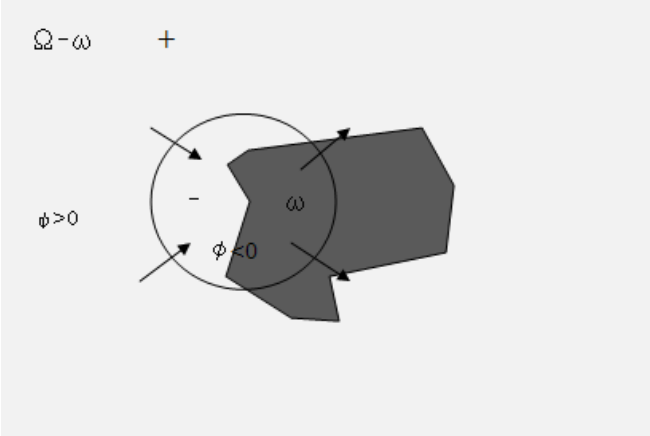


**Figure 4-4**: Evolution of the curve *C* in the image.

In Figure 4-4, "+" and "-" represent the sign of speed term, "→" is the motivation of the curve *C*. We can see that according Hamilton-Jacobi partial differential equation, the

curve $C$ will eventually stop in the target's boundary [73]. A given curve $C$ is represented implicitly, as the zero level set of a scalar Lipschitz continuous function $\phi$, such that (see Figure 4-4):

$$\begin{cases} \phi < 0 & in \quad w \\ \phi > 0 & in \quad \Omega \setminus w \\ \phi = 0 & on \quad \partial w \end{cases} \tag{4.30}$$

In this paper, we utilize a semi-implicit additive operator splitting (AOS) method [68] rather than explicit schemes to implement the discrete level set processing. The basic idea of the AOS scheme [74] is to split the m-dimensional spatial operator into a set of one-dimensional space discretization that can be efficiently solved with Gaussian elimination algorithm named Thomas Algorithm [75].

To simplified form of Eq.(4.24) and Eq.(4.25), $\frac{\partial \phi}{\partial t} = \delta_{\varepsilon}(\phi) div\left(\frac{\nabla \phi}{|\nabla \phi|}\right)$ can be written by the semi-implicit AOS scheme as

$$\varphi_i^{n+1} = \varphi_i^n + \tau\delta(\varphi_i) \sum_{j \in N(i)} \frac{2}{(|\nabla\varphi|)_i^n + (|\nabla\varphi|)_j^n} (\varphi_j^{n+1} - \varphi_i^{n+1}), \tag{4.31}$$

where, $\tau$ is the time step size. Note that, by evaluate only image positions with $|\nabla\phi|_i \neq 0$, the denominator in this scheme is not disappearance. In matrix-vector notation this becomes

$$\phi^{n+1} = \phi^n + \tau\left(\sum_{l \in \{x,y\}} A_l(\phi^n)\right)\phi^{n+1} \quad , \tag{4.32}$$

where $A_l$ describes the interaction in $l$ direction. $x$,$y$ respectively the *x-direction* and *y-direction* (2D). With the definition of $A_l(\phi^n) = a_{ij}(\phi^n)$, and $a_{ij}(\phi^n)$ can be expressed as

$$a_{ij} = \begin{cases} \delta(\phi_i)\frac{2}{(|\nabla\phi|)_i^n + (|\nabla\phi|)_j^n}, & j \in N_l(i) \\ 0, & else \\ -\delta(\phi_i)\frac{2}{(|\nabla\phi|)_i^n + (|\nabla\phi|)_j^n}, & i = j \end{cases} \tag{4.33}$$

According to above equations, the formulation (5.33) can be re-expressed as

$$\phi^{n+1} = \frac{1}{2}\sum_{l\in\{x,y\}}\left(I - 2\tau A_l(\phi^n)\right)^{-1}\phi^n . \tag{4.34}$$

So, combine with formulation (4.31), the formulation (4.24) and (4.25) finally can be rewritten as,

$$\begin{aligned} \phi_1^{n+1} &= |\nabla\phi_1^n| \{\frac{1}{2}\sum_{l=1}^{2}\left(I - 2\tau\mu A_l(\phi_1^n)\right)^{-1} \\ &\times [\phi_1^n - \left(u_0 - \tfrac{c_{11}+c_{01}}{2}\right)H(\phi_2^n) + \left(u_0 - \tfrac{c_{10}+c_{00}}{2}\right)\left(1 - H(\phi_2^n)\right)]\} \end{aligned} \tag{4.35}$$

$$\begin{aligned} \phi_2^{n+1} &= |\nabla\phi_2^n| \{\frac{1}{2}\sum_{l=1}^{2}\left(I - 2\tau\mu A_l(\phi_2^n)\right)^{-1} \\ &\times [\phi_2^n - \left(u_0 - \tfrac{c_{11}+c_{10}}{2}\right)H(\phi_1^n) + \left(u_0 - \tfrac{c_{01}+c_{00}}{2}\right)\left(1 - H(\phi_1^n)\right)]\} \end{aligned} \tag{4.36}$$

This is the gradient decent flow functions of our model. From the above equations, we know that the AOS scheme speed up the FACM model.

In our model, we simplify the traditional level set model. Meanwhile, utilize the AOS scheme for accurate the systolic velocity. The main procedures of the proposed model are summarized as follows,

**Step 1:** Initialize each level set curve $C_i^0$ and $\phi_i^0$;

**Step 2:** To calculate $\phi_{ix}^{n+1}$, $\phi_{iy}^{n+1}$ respectively in *x-direction* and *y-direction*. Set $\phi_i^{n+1} = 1/2(\phi_{ix}^{n+1} + \phi_{iy}^{n+1})$;

**Step 3:** Estimate the convergence of $\phi_i^{n+1}$ by equation $Q = \left(\sum_{i,j}|\delta_\varepsilon(\phi_{i,j}^{n+1}) - \delta_\varepsilon(\phi_{i,j}^n)|\right)/M$,

$M$ is the size of image $u_0$. If $Q$ is constriction, end the loop; else, set $\phi_i^{n+1}$ as new initial value, return to **Step 2**;

**Step 4:** If all of $\phi_i^{n+1}$ ($i=1, 2$) are constriction, end the algorithm.

From this algorithm, we can found that it speed up the computational complexity of re-initialization. Beside of this, it take implicit active contour formulation, speed up the computational complexity. The effectiveness of this model will be discussed in the next section [76].

## 4.4 Experiments

In these experiments, we used *Windows* XP, *Intel Core* 2.0 GHz, and 1G RAM. We compare the proposed method with state-art methods. In Figure 4-5, the input images are the images with aforementioned enhancement method and other traditional methods. We use the proposed fast active contour model method ($\lambda_1 = \lambda_2 = 1$, $\mu = 0.1 \times 255^2$ $\nu = 0$ ) to segment these images. In Figure 4-5, we can find that with the proposed method 17 blocks can be detected. It is more than other methods (Figure4-5 (b), (c), (d), (e), (f), and (g)). Although Bazeille's method can detected 23 blocks, the image is over segmented. We also use intra-inter contrast value to assessment the results. The intra-inter value of Bazeille's method, Fattal's method, Nicholas's method, He's method, Ancuti's method, Chiang's method and Xiao's method respectively is 0.5021, 0.5007, 0.5006, 0.5008, 0.5009, 0.5017, 0.5018. But the intra-inter value of proposed method is 0.5022 which is larger than other methods. Therefore, the proposed method can obtain well segmentation results and is suitable for underwater images.

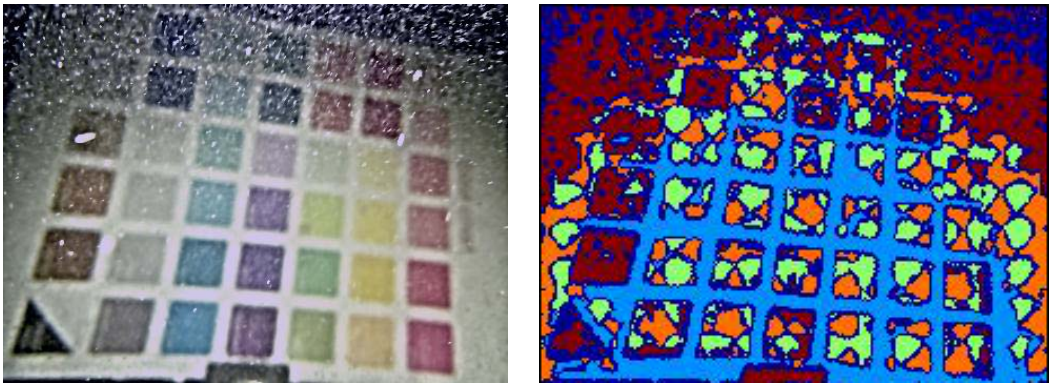

(a)

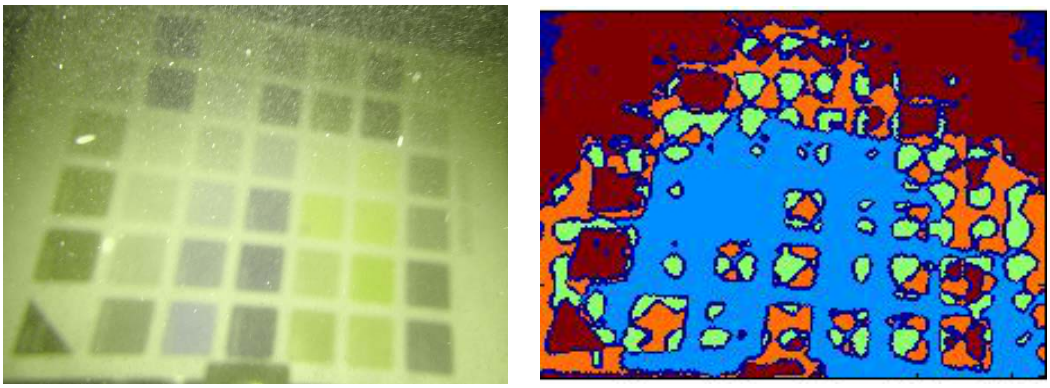

(b)

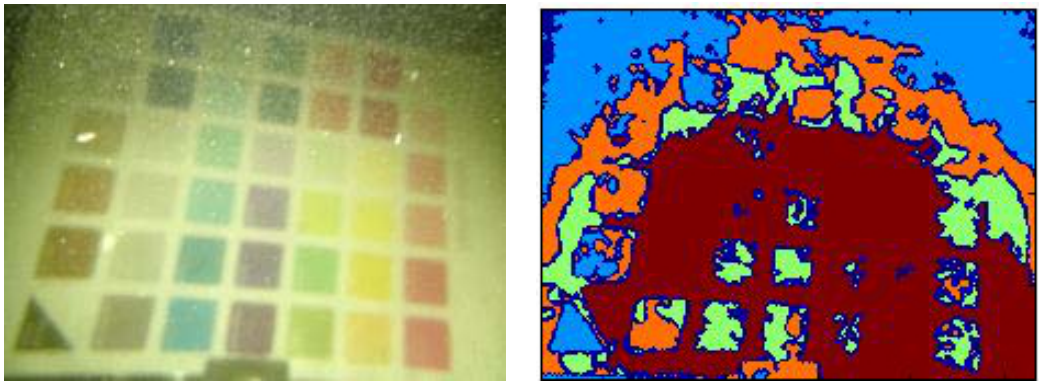

(c)

**Figure 4-5:** Using different methods for underwater image segmentation. (a) Bazeille's method, Blocks=23; (b) Fattal's method, Blocks=13; (c) Nicholas's method, Blocks=10; (d) He's method, Blocks=15; (e) Ancuti's method, Blocks=12; (f) Chiang's method, Blocks=7; (g) Xiao's method, Blocks=13; (h) Proposed method, Blocks=17. (*Cont.*)

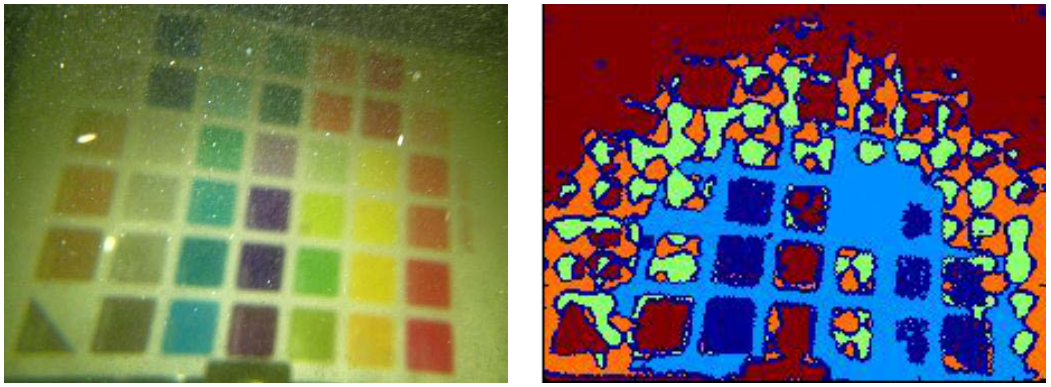

(d)

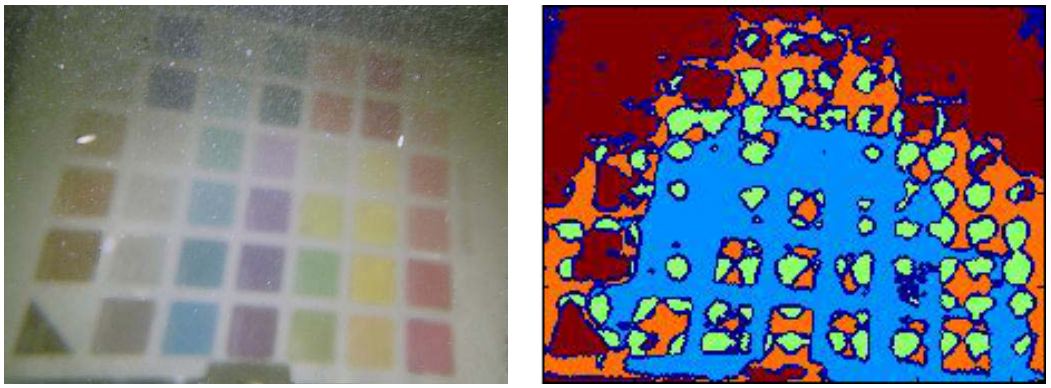

(e)

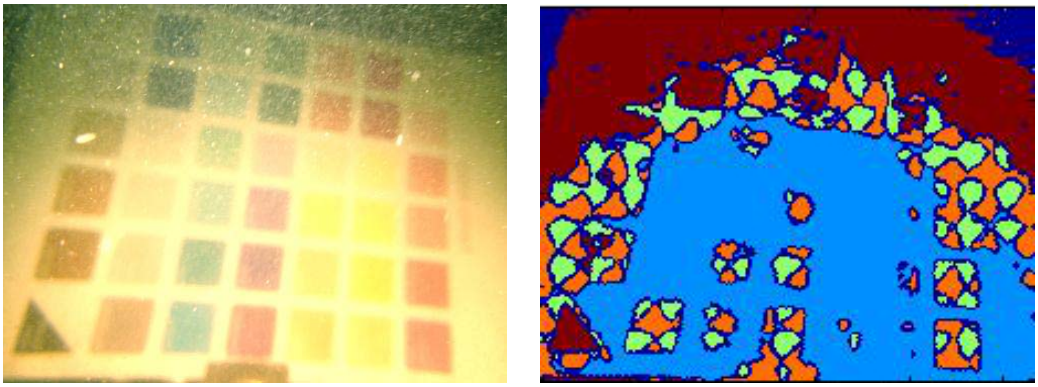

(f)

**Figure 4-5:** Using different methods for underwater image segmentation. (a) Bazeille's method, Blocks=23; (b) Fattal's method, Blocks=13; (c) Nicholas's method, Blocks=10; (d) He's method, Blocks=15; (e) Ancuti's method, Blocks=12; (f) Chiang's method, Blocks=7; (g) Xiao's method, Blocks=13; (h) Proposed method, Blocks=17. (*Cont.*)

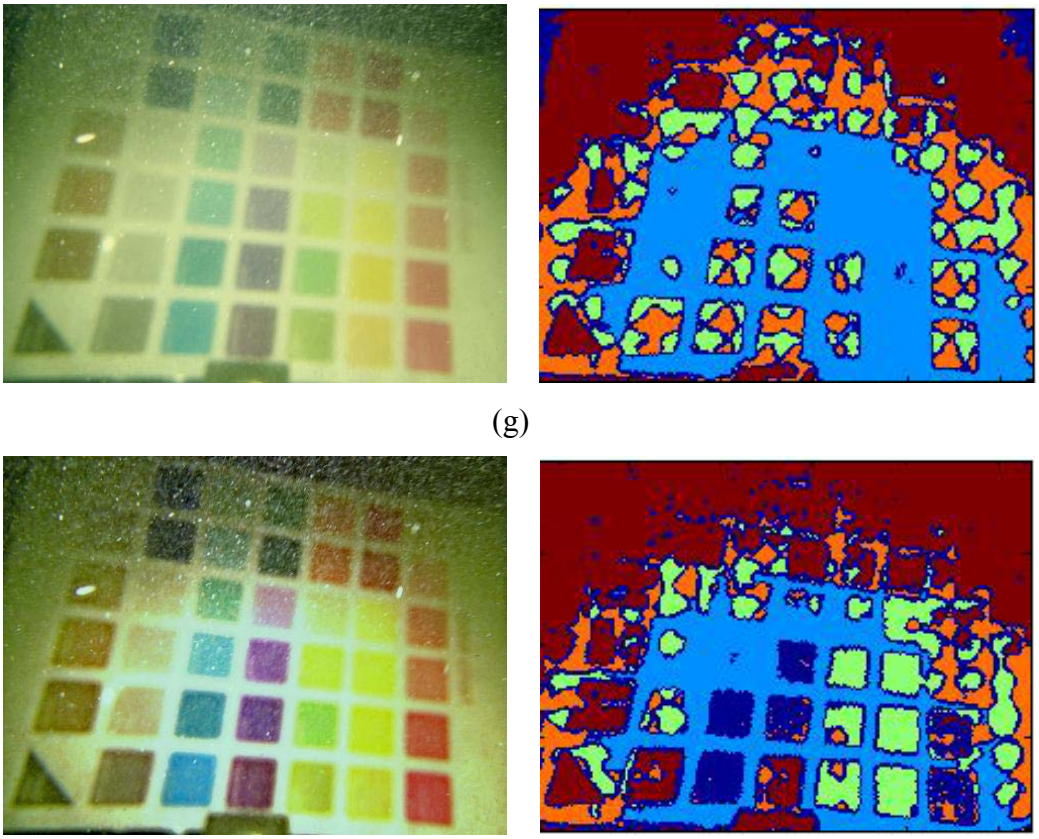

**Figure 4-5:** Using different methods for underwater image segmentation. (a) Bazeille's method, Blocks=23; (b) Fattal's method, Blocks=13; (c) Nicholas's method, Blocks=10; (d) He's method, Blocks=15; (e) Ancuti's method, Blocks=12; (f) Chiang's method, Blocks=7; (g) Xiao's method, Blocks=13; (h) Proposed method, Blocks=17.

Figure 4-6 shows the comparison of the proposed method with state-art methods. From the results, we can see that, with the Snake method only can detected 6 blocks, with Chan-Vese method 10 blocks can be detected, but the proposed method can detect 17 blocks. The intra-inter value of Snake method is 0.5015, the intra-inter value of Chan-Vese method is 0.5009, the intra-inter value of proposed method is 0.5022 which is larger than Snake and Chan-Vese method. The Snake method cost CPU time is 232 sec. The Chan-Vese method cost CPU time is 165 sec; however, the proposed method only cost 24 sec. Therefore, the proposed method can segment image better.

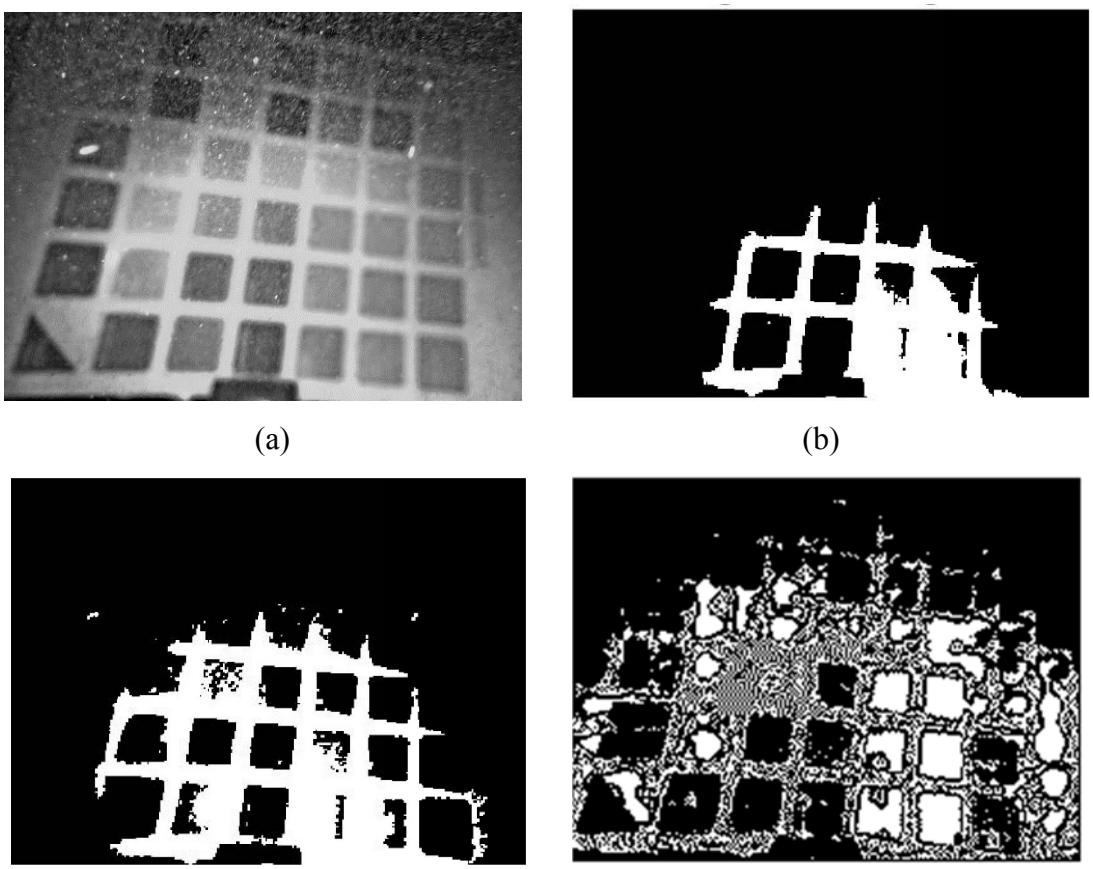

(a) (b)

(c) (d)

**Figure 4-6:** Using different level set methods for underwater image segmentation. (a) Input image; (b) Snake method; (c) Chan-Vese method; (d) Proposed method.

## 4.5 Conclusion

In this chapter, we present ACWFCM for image segmentation. The proposed gradation-gradient two-dimensional histogram method not only can remove the high value pixels, which can more effectively eliminate the influence of heavy noise, but also can automatically obtain the cluster number. The experiments show that ACWFCM can segment images with simple texture very well.

We also presented a novel ACM (FACM) for image segmentation which is based on level set evolution method. The new model makes full use of the advantages of GAC model and CV model. We consider that there are three primary contributions: (i) the

proposed FACM method reduces the expensive re-initialization of traditional level set method to make the model more efficient, (ii) the FACM method utilize the AOS scheme for accelerate the computational complexity, which is confirmed a satisfy method for level set methods, (iii) the FACM method combines the ability of GAC model and PC model, which possesses the property of region or global segmentation. Experimental results show the effectiveness of FACM method in terms of segmenting images. Image segmentation is a complex and difficult problem, the FACM cannot perform well under any circumstances. In future, we will improve this model further, to improve its robustness and versatility.

# Chapter 5

# Conclusions

This chapter summarizes the contents and contributions of the thesis, and suggests several directions for future work based on the current stage of the research.

## 5.1 Summary

In this thesis, a full approach for underwater image processing has been proposed. The full approach extends the normal image restoration and enhancement techniques. For complex and challenging ocean medium, the aim is to obtain clear images which can be used for monitoring the geological, biological environment of seafloor.

Underwater imaging suffers from specific environment that require specific solutions. The contributions of this thesis concern the optical imaging techniques which can significantly improve the final image quality and visual pleasantness.

Chapter 2 describes a novel underwater image enhancement method. The transmission is estimated by the proposed dual-channel prior. Then a robust locally adaptive filter algorithm for enhancing underwater images is used. In addition, the artificial light removal method is also proposed. Compared with the traditional methods, the proposed method obtains better images.

Chapter 3 presents a color correction method to recover the distorted image colors. In the experiments, the proposed method recovers the distorted colors in real-time. The color corrected images have a reasonable noise level in their dark regions, and the global contrast is also well improved.

Chapter 4 describes two methods for image segmentation. The first one is the automatic clustering Weighted Fuzzy C Means (WFCM) based segmentation method. It automatically obtains a reasonable clustering result for the underwater images with

simple texture. The second method is fast Active Contour Model (ACM) based image segmentation method, which dramatically improves the calculation speed. Compare with the traditional methods, the processing speed is improved by over 10 times.

## 5.2 Contributions

The present works led to some contributions to the state-of-the-art methods and are listed as follows:

- A novel underwater imaging model that compensates for attenuation discrepancies along the propagation path was proposed. In addition, an artificial light removal method for underwater optical images was developed.

- One color correction method for underwater image reconstruction was proposed. It is based on camera spectral response, color temperature and spectral power distribution. This method can recover the real scene actually.

- Two methods for underwater image segmentation were proposed. The first one is automatic clustering weighted Fuzzy C Means based image segmentation method. It can segment the simple objects in water. The second one is fast active contour model based image segmentation method. Compare with the traditional level set methods, the processing speed of proposed method was improved by over 10 times.

## 5.3 Future Work

The proposed methods attempt to solve the underwater surveying vision problems by AUVs or Deep-sea Mining Systems (DMS). The field of underwater imaging is very new and much remains to be explored. Several long-term results would make a difference. Regarding future work, there are still several open problems which will require the development of new techniques.

On the one hand, to improve the existing underwater imaging system, thereby it can fully recover the real color of underwater images.

On the other hand, for underwater optical system, we want to do some improvements and then apply them to some applications, such as underwater archeology, fish observation and so on.

Finally, we would like to combine the existing system with robots and make the robots to do some underwater exploration, such as underwater search, mineral exploration, and detection salvage and so on. It is an important future direction that improves monitoring underwater robots which not entirely dependent on intelligent machines but more dependent sensors and human intelligence.

# Bibliography


[1] Ocean observations, *Wikipedia*, http://en.wikipedia.org/wiki/Ocean_observations.

[2] Ocean Networks Canada, http://www.oceannetworks.ca/installations/observatories

[3] O. NOAA Ocean Climate Observation Program, http://www.oco.noaa.gov/.

[4] Japanese Ocean Flux Data Sets with Use of Remote Sensing Observation, http://dtsv.scc.u-tokai.ac.jp/j-ofuro/.

[5] Woods Hole Oceanographic Institution, https://www.whoi.edu/.

[6] F. Muller-Karger, M. Roffer, N. Walker, M. Oliver, O. Schofield, "Satellite remote sensing in support of an integrated ocean observing system", *IEEE Geoscience and Remote Sensing Magazine*, vol.1, no.4, pp.8-18, 2013.

[7] Data Buoy Cooperation Panel, http://www.jcommops.org/dbcp/.

[8] Underwater Acoustic Sensor Networks, http://www.ece.gatech.edu/research/labs/bwn/UWASN/

[9] J.P. Fish, "Sound underwater images: a guide to the generation and interpretation of side scan sonar data", *2nd Ed., Lower Cape Publishing*, Oreleans, MA, 1991.

[10] J.S.M. Rusby, J. Revie, "Long-range mapping of the continental shelf", Marine Geology, vol.19, no.4, pp.M41-M49, 1975.

[11] P. Blondel, and B.J. Murton, "Handbook of seafloor sonar imagery", *Wiley-Praxis Series in remote sensing*, Edited by: D. Sloggett, John Wiley & Sons, Chichester, 1997.

[12] E. Belcher, W. Hanot, J. Burch, "Dual-frequency identification sonar", *in: Proc. of the 2002 International Symposium on Underwater Technology*, pp.187-192, 2002.

[13] A. Davis, A. Lugsdin, “High speed underwater inspection for port and harbor security using Coda Echoscope 3D sonar”, *in: Proc. of MTS/IEEE OCEANS*, vol.3, no.1-6, 2005.

[14] BlueView Technologies, http://www.blueviewtech.com, last access: 14 December 2013.

[15] R. Schettini, S. Corchs, “Underwater image processing: state of the art of restoration and image enhancement methods”, *EURASIP Journal on Advances in Signal Processing*, vol.2010, ID 746051, pp.1-14, 2010.

[16] Kocak. DM, Da. FR, “A focus on recent developments and trends in underwater imaging”, *Marine Technology Society Journal*, vol.42, no.1, pp.52-67, 2008.

[17] J. Tarel, N.Ca, “Fast visibility restoration from a single color or gray level image”, *In Proceedings of IEEE Conference of Computer Vision and Pattern Recognition*, pp.2201-2208, 2009.

[18] M. Chambah, D.Semani, “Underwater color constancy: enhancement of automatic live fish recognition”, *In Proceedings of SPIE*, pp.157-168, 2004.

[19] Ocean Optics, www.oceanopticsbook.info.

[20] H. Lu, “Contrast enhancement for images in turbid water”, *Journal of Optical Society of America,* vol.32, no.5, pp.886-893, 2015

[21] D.M. Kocak, F.R. Dalgleish, F.M. Caimi; Y.Y. Schechner, “A focus on recent developments and trends in underwater imaging”, *Technol. Soc. J.*, vol.42, no.1 pp.52-67, 2008.

[22] R. Schettini, S. Corchs, “Underwater image processing: state of the art of restoration and image enhancement methods”, *EURASIP J. Adv. Sig. Pr.*, 746052, 2010.

[23] R. Schettini, S. Corchs, “Enhancing Underwater Image by Dehazing and Colorization”, *International Review on Computers and Software*, vol.7, no.7, pp.3470-3474, 2012.

[24] C.O. Ancuti, T. Haber, P. Bekaert, “Enhancing underwater images and videos by fusion”, *in: Proceedings of IEEE Conference on Computer Vision and Pattern Recognition*, pp.81-88, 2012.

[25] R. Fattal, “Signal image dehazing”, *In SIGGRAPH*, pp.1-9, 2008.

[26] K. He; J. Sun, X. Tang, “Single image haze removal using dark channel prior”, *IEEE T. Pattern Anal*, vol.33, no.12, pp2341-2353, 2011.

[27] K. He; J. Sun, X. Tang, “Guided image filtering”, *In Proceedings of the 11th European Conference on Computer Vision*, vol.1, pp.1-14, 2010.

[28] C.B. Nicholas, M. Anush, R. M. Eustice, “Initial results in underwater single image dehazing”, *In Proc. of IEEE OCEANS*, pp.1-8, 2010.

[29] J. Y. Chiang, Y.C. Chen, “Underwater image enhancement by wavelength compensation and dehazing”, IEEE T. Image Process, vol.21, no.4, pp. 1756–1769, 2012.

[30] Seiichi Serikawa, H.M. Lu, “Underwater image dehazing using joint trilateral filter ”, *Computera and Electrical Engineering*, vol.40, no.1, pp.41-50, 2014.

[31] M. Chambah, D. Semani, A. Renouf, P. Courtellemont, “Underwater color constancy: enhancement of automatic live fish recognition”, *In Proceedings of SPIE,* vol. 5293, p157-168, 2004.

[32] A. Rizzi, C. Gatta, D. Marini, “A new algorithm for unsupervised global and local color correction”, *Pattern Recogn. Lett*, vol.24, pp.1663-1677, 2003.

[33] Yujie Li, Huimin Lu, Seiichi Serikawa, “Natural image feathering using referenced depth image filter ”, *Information*, vol.17, no.2, pp. 515–521, 2014.

[34] Huimin Lu, Yujie Li, “Underwater Image Enhancement Method Using Weighted Guided Trigonometric Filtering and Artificial Light Correction”, *Journal of Visual Communication and Image Representation*, to be submitted.

[35] H. M. Lu, Y. J. Li, “Underwater optical image dehazing using guided trigonometric bilateral filtering”, Proceedings of IEEE International Symposium on Circuits and Systems(ISCAS 2013), pp. 2147-2150, 2013

[36] Yin L, Yang R, “Weighted median filters: a tutorial”, *IEEE Transactions on Circuits and System*, vol. 43, no.3, pp.157-192, 1996.

[37] Yujie Li, Huimin Lu, Seiichi Serikawa, “A novel deep-sea image enhancement method ”, *Proceedings of 2nd International Symposium on Computer, Consumer and Control Process*(*IS3C2014*), pp.529-532, 2014.

[38] Artificial Light Correction”, Marine Science Bulletin, vol.5, no.1, pp.16-23, 2003.

[39] Stephane. Bazeille, Isabelle. Quidu, “Automatic underwater image pre-processing”, *CMM’06, Oct 2006, Brest, France, <hal-00504893>*, https://hal.archives-ouvertes.fr/hal-00504893.

[40] Chambah. M, D. Renouf, “Underwater color constancy: enhancement of automatic live fish recognition”, *Electronic Imaging, International Society for Optics and Photonics*, pp.157-168, 2003.

[41] Marcelo Bertalmio, Vicent Caselles, “Perceptual color Correction Through Variational Techniques”, *IEEE Transaction on image processing*, vol.16, no.4, pp.1058-1072, 2007.

[42] Kashif. Iqbal, “Underwater image enhancement using integrated colour model”, *IAENG International Journal of Computer Science*, vol.34, no.2, pp.24-30, 2007.

[43] Z. Andreas Arnold-Bos, “A preprocessing framework for automatic underwater image denoising”, *European Conference on Propagation and Systems*, 2005, https://hal.archives-ouvertes.fr/hal-00494314.

[44] Yu. Li, Hui. H, “Real-time visualization system for deep-sea surveying”, *Mathematical Problems in Engineering*, vol.2014, pp.1-10, 2014.

[45] Huimin. Lu, Seiichi. Serikawa, “Underwater image enhancement using guided trigonometric bilateral filter and fast automatic color correction”, *Proc. of 2013 IEEE International Conference on Image Processing (ICIP2013)*, pp.3412-3416, 2013.

[46] H. Lu, S. Serikawa, “A novel underwater scene reconstruction method”, *Proceedings of 2014 International Symposium on Computer, Consumer and Control*, pp.773-775, 2014.

[47] R.C. Gonzalez, and R.E. Woods, “Digital Image Processing”, *I2nd Edition*, Prentice Hall, 2008.

[48] H. Lu, L. Zhang, “A method for infrared image segmentation based on sharp frequency localized contourlet transform and morphology”, *Proceeding of International Conference on Intelligent Control and Information Processing*, pp.79-82, 2010.

[49] Yujie. Li, Huimin. Lu, “An improved detection algorithm based on morphology methods for blood cancer cells detection”, *Journal of Computational Information Systems*, vol.7, no.13, pp.4724-4734, 2011.

[50] Yujie. Li, Huimin. Lu, “Segmentation of offshore oil spill image in leakage acoustic detection system”, *Research Journal of Chemistry and Environment*, vol.17, no.s1, pp36-41, 2013.

[51] B. Otman, Z. Hongwei, K. Fakhri, “Connectionist-based dempster- shafer evidential reasoning for data fusion”, *Neural Networks, IEEE Transactions on*, vol.16, no.6, pp.1513-1530, 2005.

[52] S. Shen, W.A. Sandham, “Fuzzy clustering based applications to medical image segmentation”, *Proceeding of the 25th Annual International Conference on the IEEE EMBS*, pp.747-750, 2003.

[53] M. Hung, D. Yang, “An efficient fuzzy c-means clustering algorithm”, *Proceeding of International Conference on Data Mining*, pp.225-232, 2001.

[54] G. Xinbo, L. Jie, J. Hongbing, “A multi-threshold image segmentation algorithm based on weighting fuzzy c-means clustering and statistical test”, ACTA ELCTRONICA SINICA, vol.32, no.4, pp.661-664, 2004.

[55] Yujie. Li, Humin. Lu “An automatic image segmentation algorithm based on weighting fuzzy C-means clustering”, *Soft Computing in Information Communication Technology , Advances in Intelligent and Soft Computing* , vol.58, no.4, pp.27-32, 2012.

[56] Yujie. Li, Huimin .Lu, “Robust color image segmentation method based on weighting Fuzzy C-Means Clustering”, *IEEE/SICE International Symposium on System Integration (SII)*, pp.133-137, 2012.

[57] A.M. Nazif, M.D.Levine, “Low level image segmentation: an expert system”, IEEE Transaction on Pattern Analysis and Machine Intelligence, vol.6, pp.555-577, 1984.

[58] M. Kass, A. Witkin, D. Terzopoulos, “Snakes: active contour models”, *International Journal of Computer Vision*, vol.1, pp.321-331, 1988.

[59] V. Caselles, R. Kimmel, G. Sapiro, “Geodesic active contours”, *International Journal of Computer Vision*, vol.22, no.1, pp.61-79, 1997.

[60] R. Malladi, J.A. Sethian, “Shape modeling with front propagation: a level set approach”, *IEEE Transactions on Pattern Analysis and Machine Intelligence*, vol.17, no.2, pp.158-175, 1995.

[61] J. Lie, M. Lysaker, "A binary level set model and some application to Mumford-Shah image segmentation", *IEEE Transactions on Image Processing*, vol.15, no.5, pp.1171-1181, 2006.

[62] C. Li, C. Kao, "Minimization of region-scalable fitting energy for image segmentation", *IEEE Transactions on Image Processing*, vol.17, no.10, pp.1940-1949, 2008.

[63] T.F. Chan, "Active contours without edges", *IEEE Transactions on Image Processing*, vol.10, no.2, pp.266-277, 2001.

[64] D. Mumford, J. Shah, "Optimal approximation by piecewise smooth function and associated variational problems", *Communications on Pure and Applied Mathematics*, vol.42, no.5, pp.577-685, 1989.

[65] L.A. Vese, T.F. Chan, "A multiphase level set framework for image segmentation using the Mumford-Shah model", *International Journal of Computer Vision*, vol.50, no.3, pp.271-293, 2007.

[66] T.M. Le, L.A. Vese, "Additive and multiplicative piecewise-smooth segmentation models in functional minimization approach", *Contemporary Mathematics*, vol.445, pp.207-223, 2007.

[67] C. Li, C. Xu, C. Gui, "Level set evolution without re-initialization: a new variational formulation", *in: Proc. of IEEE Conference on Computer Vision and Pattern Recognition, San Diego, 2005*, pp.430-436, 2005.

[68] G. Kuhne, J. Weickert, "Fast implicit active contour models", *Pattern Recognition, Lecture Notes in Computer Science*, pp.133-140, 2002.

[69] J.A. Sethian, "Level set methods and fast marching methods", *evolving interfaces in computational geometry, fluid mechanics, computer vision and materials science*, Cambridge University Press, 1999.

[70] D. Cremers, M. Rousson, “A review of statistical approaches to level set segmentation: integrating color, texture, motion, and shape”, *International Journal of Computer Vision*, vol.72, no.2, 2007.

[71] N. Paragios, R. Deriche, “Geodesic active regions: a new framework to deal with frame partition problems in computer vision”, *Journal of Visual Communication and Image Representation*, vol.3, no.1-2, pp.249-268, 2002.

[72] H. Lu, S.S, “Proposal of fast implicit level set scheme for medical segmentation using the Chan and Vese model”, *Applied Mechanics and Materials*, vol. 103, pp. 695-699, 2012.

[73] Huimin. Lu S.Serikawa, “Fast level set segmentation method in medical multi-sensor images detection”, *International Journal of Advancements in Computing Technology*, vol.4, no.23, pp.475-482, 2012.

[74] Yujie. Li, Huimin.Lu, “A new segmentation method implicit level set scheme in X/ $\gamma$ -ray inspection system”, *Applied Mechanics and Materials*, vol.103, pp.705-710, 2011.

[75] H. M. LU, Y. J. Li, “Effective fast active contours model for image segmentation”, *Applied Mathematics &Information Science*, vol.7, no.1s, pp.1-4, 2013.

# Acknowledgments

First of all, I owe much to my supervisor Prof. Seiichi Serikawa for giving me the opportunity and the support to work on this research project. His insightful remarks and suggestions were invaluable for me during this period. I have learned much more than this dissertation. All of these properties will benefit my long life.

I would like to thank Serikawa Laboratory members, in particular Dr. Lifeng Zhang, Dr. Shiyuan Yang, Dr. Akira Yamawaki and Dr. Huimin Lu. During the undertaking of this project, the laboratory members have been very supportive and have provided a wonderful working environment. I am very grateful to all my friends in the Serikawa Laboratory for their tremendous support.

Finally, I also wish to express my appreciation to the entire reviewers of my thesis, Prof. Yoshihisa Nakato, Prof. Takeshi Ikenaga, and Prof. Hyoungseop Kim for giving me some helpful comments and suggestions.